UNIVERSIDAD NACIONAL AUTÓNOMA DE MÉXICO

PROGRAMA DE MAESTRÍA Y DOCTORADO EN INGENIERÍA

INGENIERÍA EN EXPLORACIÓN Y EXPLOTACIÓN DE RECURSOS NATURALES – YACIMIENTOS

COMPOSITIONAL STREAMLINE-BASED MODELING OF POLYMER FLOODING INCLUDING RHEOLOGY, RETENTION AND SALINITY VARIATION.

TESIS
QUE PARA OPTAR POR EL GRADO DE:

DOCTOR EN INGENIERÍA

PRESENTA:

FRANCISCO JAVIER ROSADO VÁZQUEZ

TUTOR PRINCIPAL

DR. SIMÓN LÓPEZ RAMÍREZ,
FACULTAD DE INGENIERÍA
CIUDAD UNIVERSITARIA, CD. MX. SEPTIEMBRE 2023

JURADO ASIGNADO:

Presidente:	Dr. Fernando Samaniego Verduzco
Secretario:	Dr. José Luis Bashbush Bauza
1 er. Vocal:	Dr. Simón López Ramírez
2 do. Vocal:	Dr. Fernando Rodríguez de la Garza
3 er. Vocal:	Dr. Jesús Rivera Rodríguez

UNIVERSIDAD NACIONAL AUTÓNOMA DE MÉXICO.
División de Estudios de Posgrado, Facultad de Ingeniería.
Cd. Universitaria, Ciudad de México, México.

TUTOR DE TESIS:

Dr. Simón López Ramírez

FIRMA

Abstract

Polymer flooding is one of the most used chemical enhanced oil recovery (CEOR) technology worldwide. Because of its commercial success at field scale, there has been an increasing interest to expand its applicability to more unfavorable mobility ratio conditions, such as more viscous oil. Therefore, an important requirement of success is to find a set of design parameters that balance material requirements and petroleum recovery benefits in a cost-effective manner. Then, prediction of oil recovery turns out to handle more detailed information and time consuming field reservoir simulation. Thus, for an effective Enhanced Oil Recovery project management, a quick and feasible tool is needed to identify projects for polymer flooding applications, without giving up key physical and chemical phenomena related to the recovery process, and avoiding activities or projects that have no hope of achieving adequate profitability.

A detailed one-dimensional mathematical model for multiphase compositional polymer flooding is presented. The mathematical formulation is based on fractional flow theory and, as a function of fluid saturation and chemical compositions, it considers phenomena such as rheology behavior (shear thinning and shear thickening), salinity variations, permeability reduction and polymer adsorption. Moreover, by setting proper boundary and initial conditions the formulation can model different polymer injection strategies such as slug or continuous injection. A numerical model based on finite-difference formulation with a fully implicit scheme was derived to solve the system of nonlinear equations. The validation of the numerical algorithm is verified through analytical solutions, coreflood laboratory experiments and a CMG-STARS numerical model for waterflooding and polymer flooding.

The linear model is used to carried out a flow dynamic analysis to investigated key aspects for optimum strategies that would help to increase polymer flooding effectiveness. The aspects analyzed are the effects of polymer and salinity concentrations, apparent aqueous viscosity - shear rate relationship, permeability reduction, reversible - irreversible polymer adsorption, and polymer injection strategies, on petroleum recovery.

The one-dimensional model is extended to a two-dimensional model through the implementation of the streamline-based approach. This, as an alternative to have a multidimensional practical tool thoroughly representing the physical and chemical behavior of polymer flooding by considering key phenomena

such as rheology behavior, salinity variations, permeability reduction, and polymer adsorption. Previously published streamline multidimensional models for polymer flooding lack of the integrated modeling of the above-mentioned key phenomena. Additionally, the models to represent rheology and retention phenomena in the proposed tool consider a more completed description than present streamline-based simulators.

For the numerical treatment, we considered a black oil formulation to estimate the pressure and saturation 2D distribution by applying the implicit in pressure and explicit in saturation (IMPES) method, coupled with an explicit formulation for the 2D composition computation. For the saturation-composition along the streamlines, the 1D validated practical tool mentioned previously was incorporated, as well as its capability to represent the polymer flooding key phenomena. The numerical algorithm used by the streamline-based tool is supported by laboratory experiments for waterflooding in homogenous medium, analytical results for waterflooding in heterogeneous medium, polymer flooding field scale simulation case of the literature, and CMG-STARS model built as a reference for waterflooding in homogenous and heterogeneous medium, and for polymer flooding.

The 1D model and the 2D streamline-base model are practical tools that help to connect math with physics, facilitating the upscaling from laboratory observations to field application with better fitted numerical simulation models, that contribute to determine favorable scenarios, and thus, it could assist engineers to understand how key parameters affect oil recovery without performing time consuming CEOR simulations.

Resumen

La inyección de polímeros es una de las tecnologías, de la recuperación mejorada, que más se aplican para la recuperación mejorada de petróleo. Debido a su éxito comercial a escala de campo, se ha incrementado el interés por aplicaciones en condiciones de relación de movilidades desfavorables. Por lo que es importante, basar el éxito en un diseño que equilibre el requerimiento de materiales, beneficio en la recuperación del petróleo, y un manejo eficiente de costos. Para esto, los pronósticos de los simuladores numéricos de yacimientos, a escala de campo, han requerido información más detallada y mayor consumo de tiempo. Entonces, para una eficiente administración de proyectos de recuperación mejorada, una herramienta práctica-eficiente es requerida, y así poder identificar rápidamente proyectos candidatos para la inyección de químicos, esto sin dejar de captar los fenómenos físicos y químicos claves del proceso, y a su vez evitando proyectos sin una adecuada rentabilidad.

En esta investigación se presenta un modelo matemático, 1D, para la inyección de polímeros, con una descripción multifásica y composicional. La formulación se basa en la teoría de flujo fraccional, y en función de saturaciones y composiciones, el modelo considera fenómenos como la reología del polímero (pseudoplástica o viscoelástica), variación de salinidad, reducción de permeabilidad y adsorción del polímero. Con las condiciones de frontera e iniciales apropiadas, la formulación puede modelar diferentes estrategias para la inyección del polímero, tal como inyección continua, secundaria, o en bache de polímero. Para resolver el modelo no-lineal de ecuaciones, se aplica la formulación en diferencias finitas con un esquema totalmente implícito. La validación del algoritmo numérico se realizó con soluciones analíticas, experimentos de laboratorio en núcleos, un modelo numérico en CMG-STARS para inyección de agua e inyección de polímeros.

El modelo lineal es usado para analizar la dinámica del fujo de fluidos, y para investigar los aspectos claves de una estrategia óptima que incremente la efectividad en la inyección de polímeros. Los aspectos estudiados son el efecto de la concentración del polímero y la salinidad, la relación de la viscosidad aparente de la fase acuosa y el esfuerzo de corte, la reducción de la permeabilidad, la adsorción reversible-irreversible del polímero, y la estrategia de inyección el polímero, todos sobre la recuperación de petróleo.

Como alternativa para una herramienta práctica multidimensional, el modelo 1D es extendido a un modelo 2D con la aproximación en líneas de corriente, el cual representa el comportamiento físico y químico en la inyección de polímeros, y considera los fenómenos claves, como son la reología, la

variación de la salinidad, la reducción de la permeabilidad y la adsorción del polímero. Modelos multidimensionales basados en líneas de corriente, publicados previamente para inyección de polímeros, carecen de un modelado que integre los fenómenos claves mencionados arriba. Para el tratamiento numérico se consideró la formulación de aceite negro con el método IMPES, para estimar la distribución 2D de las presiones y saturaciones, y para la distribución 2D de las composiciones se acopló una formulación explícita. Para obtener las saturaciones y concentraciones a lo largo de las líneas de corriente se incorporó la herramienta práctica 1D mencionado previamente. El algoritmo numérico usado por la herramienta basada en líneas de corriente fue validado con experimentos de laboratorio para inyección de agua en un medio homogéneo, resultados analíticos para inyección de agua en medio anisotrópico, simulación numérica a escala de campo para inyección de polímeros, y modelado numérico construido con el simulador CMG-STARS para inyección de agua en medios homogéneo y anisotrópico, y para inyección de polímeros en un medio homogéneo.

El modelo 1D y el 2D basado en líneas de corriente son herramientas prácticas que ayudan a conectar la matemática con la física, facilitando el escalamiento de observaciones en laboratorio a aplicaciones a escala de campo, mejorando los ajustes en los modelos de simulación numérica para determinar escenarios favorables, y así entender mejor el efecto de los parámetros clave en la recuperación de petróleo, evitando el consumo de tiempo innecesario en la simulación de los procesos de inyección de químicos.

Dedication

This research is dedicated to my wife and my three daughters, whom are my inspiration and motivation to be a better man. Thanks for the support and made this possible.

Acknowledgements

I would like to thank my supervisor, Dr. Simón López Ramírez for his support, guidance, and constant encouragement in the development of this research and the international publications.

I like to thank Dr. José Luis Bashbush Bauza, for sharing me his experience and valuable advises on my studies, as well as for his contribution to my first publication from this research, and on the revision of this thesis. I also thank to Dr. Fernando Rodriguez De La Garza, for sharing me his experience, and knowledge, as well as for his contribution to my second publication from this research, and the revision of this thesis.

I want to thank both Drs. Fernando Samaniego Verduzco and Jesús Rivera Rodríguez for helping me with the revision of my thesis.

The financial support of the National Autonomous University of Mexico that made this research and my graduate studies possible.

I want to give a special thanks to my mother that have always been there to encourage me to achieve my goals. Thank you for everything you have done for me.

Finally, I would like to thank my sister, brothers, my aunt Julia, and my in-laws for their support and encouragement.

Nomenclature

Normal

A	Cross-section area, L^2
$a_{p1}, a_{p2}, a_{p3}, S_p$	Polymer viscosity at zero shear rate model parameters
a_4, b_4	Adsorption model parameters
b_{kr}, c_{kr}	Permeability reduction model parameters
C_i	Overall concentration of species i in the mobile phases
$\tilde{C}_i$	Overall concentration of species i in the mobile and stationary phases
$\hat{C}_i, Cad_i$	Rock phase concentration of species i
C_{ij}	Volume fraction of component i in phase j
C_{SEP}	Effective salinity for polymer
C^*, C_M	Empirical constants in the polymer viscosity model
E_R	Recovery efficiency
e_j	Relative permeability exponent of phase j
F_i	Fractional flux of component i
f_j	Fractional flow of phase j
$\vec{J_i}$	Mass flux of species i, $ML^{-2}T^{-1}$
$\vec{\vec{K}}_{ij}$	Dispersion tensor for species i in phase j, L^2T^{-1}
k_{rj}	Relative permeability to of phase j
k_{rj}^*	End point relative permeability to of phase j
k_{rj}	Relative permeability to of phase j
k	Permeability, L^2

L	Length of the porous media, L
M^*	End point mobility ratio
N_C	Total number of components
N_P	Total number of phases
n_C	Shear rate dependency of polymer viscosity mode parameter
$R\varepsilon_{i,\iota}$	Residual function of component i and node ι for NR method
R_i	Mass rate of production of species i, $ML^{-3}T^{-1}$
R_F	Resistance factor $= \frac{polymer\ mobility\ during\ polymer\ flows}{water\ mobility\ during\ polymer\ flows}$
R_k	Permeability reduction factor $= \frac{Rock\ perm.\ when\ water\ flows}{Rock\ perm.\ when\ aqueous\ polymer\ solution\ flows}$
R_{kmax}	Maximum permeability reduction factor
R_{RF}	Residual resistance factor $= \frac{water\ mobility\ before\ polymer\ flows}{water\ mobility\ after\ polymer\ flows}$
r_{ij}	Homogeneous reaction rate of species i in phase j, $ML^{-3}T^{-1}$
S_j	Saturation of phase j
S_{jr}	Residual saturation of phase j
S_{nj}	Normalized saturation of phase j
t	Time, T
t_D	Dimensionless time
t_r	Relaxation time of the fluid
Q	Fluid injection rate, L^3T^{-1}
$\vec{u}_j$	Superficial velocity of phase j, LT^{-1}
u	Magnitude of superficial velocity, LT^{-1}
V_b	Bulk volume of the control element, $V_b = \Delta x \Delta y \Delta z$, L^3
W_i	Overall concentration of species i, ML^{-3}

x	Position, L
y	Position, L
x_D	Dimensionless position

Greek

α, λ	Shear rate dependency of polymer viscosity model parameters
α_1, α_2	Adsorption model parameters
ϵ_A	Approximation error (area bordered by analytical and numerical solutions)
$\dot{\gamma}_c$	Equivalent shear rate model parameter, T^{-1}
$\dot{\gamma}_{eq}$	Equivalent shear rate, T^{-1}
λ_{rj}	Relative mobility of phase j, $LM^{-1}T$
μ_1^o	Polymer solution viscosity at zero shear rate, $ML^{-1}T^{-1}$
μ_{1app}	Apparent polymer solution viscosity, $ML^{-1}T^{-1}$
μ_{1el},	Shear thickening viscosity or elongational viscosity, $ML^{-1}T^{-1}$
μ_j	Viscosity of phase j, $ML^{-1}T^{-1}$
μ_{1sh}	Shear thinning viscosity, $ML^{-1}T^{-1}$
μ_∞	Viscosity at high shear limit (generally taken as water viscosity), $ML^{-1}T^{-1}$
ξ	Unknown variable for generic numerical expression
ζ	Spatial distance along streamline, L
ς	variable or index for spatial coordinate: 1 (x), 2 (y), and 3 (z)
ρ_j	Density of phase j, ML^{-3}
ψ	Streamfunction, L^2T^{-1}
$\emptyset$	Porosity, fraction
τ	Time of flight, Time, T

τ_r		Shear stress, FL^{-2}
ω_{ij}		Mass fraction of species i in phase j

Superscript

n		Time level of the numerical simulation
v		Iteration level for a time step

Subscript

i		Species index
	1	Water
	2	Oil
	4	Polymer
	5	Salinity (total monovalent anions)
ι		x coordinate index
$\not{\jmath}$		y coordinate index
j		Phase index
	1	Aqueous
	2	Oleic
s		Streamline index
$\not{f}$		τ coordinate index
l		Index for gridblock faces in each direction, $l = 1{,}2$.
m		Unknown variable index for generic numerical expression
ref		Reference for permeability in adsorption parameter

Table of contents

Abstract ..... **iii**

Resumen ..... **v**

Dedication ..... **vii**

Acknowledgements ..... **viii**

Nomenclature ..... **ix**

Table of contents ..... **xiii**

List of figures ..... **xvi**

List of tables ..... **xx**

Chapter 1: Introduction **1**

1.1 Overview on polymer flooding 1

1.2 Overview on streamline modeling 5

1.3 Outline of the dissertation 8

Chapter 2: Fundamentals of polymer flooding **10**

2.1 Concepts of waterflooding 10

2.1.1 Surface tension and interfacial tension *10*

2.1.2 Wettability *10*

2.1.3 Capillary pressure *12*

2.1.4 Relative permeability *12*

2.1.5 Mobility ratio *13*

2.2 Concepts of polymer flooding 14

2.2.1 Polymer *14*

2.2.2 Rheology *15*

2.2.3 Polymer retention *17*

Chapter 3: Mathematical model for 1D polymer flooding **20**

3.1 Mathematical modeling 20
3.1.1 Model assumptions 20
3.1.3 Model for polymer flooding 22
3.2 Numerical model for 1D polymer flooding 26
3.3 Effects of polymer and salinity concentrations on flow properties 28
3.3.1 Polymer adsorption 29
3.3.2 Permeability reduction factor 30
3.3.3 Viscosity at zero shear rate 31
3.3.4 Equivalent shear rate 32
3.3.5 Aqueous phase viscosity 33
3.3.6 Aqueous phase fractional flow 35
Chapter 4: Validation of the 1D model and flow dynamic 36
4.1 Numerical solution validation 36
4.1.1 Comparison of numerical model and analytical solution 36
4.1.2 Comparison of numerical model and core flood experiments 39
4.2 Flow dynamic analysis 46
4.2.1 Effect of shear rate and polymer concentration 47
4.2.2 Effect of salinity concentration 50
4.2.3 Effect of polymer adsorption 55
4.2.4 Effect of permeability reduction 57
4.2.5 Effect of slug size 60
4.2.6 Effect of reversible and irreversible adsorption 64
Chapter 5: Streamline-based modelling of polymer flooding 67
5.1 Fundamentals of streamline simulation 67
5.2 Streamlines model for polymer flooding 68
5.2.1 Model for pressure, saturation, and composition 2D distribution 68

5.2.2 Polymer flooding model along streamlines 71

5.2.3 Streamline construction 75

5.3 Steps for streamline simulation 76

Chapter 6: Validation of the streamline-based model 78

6.1 Waterflooding in homogenous medium 78

6.2 Waterflooding in anisotropic medium 82

6.3 Field case polymer flooding 84

Chapter 7: Conclusions 94

References 97

List of figures

Figure 2.1: Effect of wettability on saturation, (Green et al., 1998). 11

Figure 2.2: Interfacial forces at an interface between two immiscible fluids and a solid, (Green et al., 1998). 11

Figure 2.3: Viscosity versus shear rate for a typical pseudoplastic fluid flow behavior, (Sheng, 2011). 16

Figure 2.4: Schematic illustration of viscoelastic fluid flow behavior, (Sheng, 2011). 17

Figure 2.5: Schematic illustration of polymer retention mechanisms in porous media, (Sorbie, 1991). 18

Figure 3.1: Flowchart of the numerical simulator developed. 27

Figure 3.2: Polymer adsorption concentration for no-salinity effect and salinities $0.01wt\%$ *and* $0.1wt\%$*. 30*

Figure 3.3: Maximum value for permeability reduction factor versus effective salinity. 31

Figure 3.4: Viscosity at zero shear rate versus polymer concentration. 32

Figure 3.5: Water fractional flow and equivalent shear rate versus water saturation. 33

Figure 3.6: Shear rate and apparent polymer viscosity versus water saturation. 34

Figure 3.7: Water fractional flow and apparent polymer viscosity versus water saturation. 34

Figure 4.1: Comparative of numerical and analytical solutions for waterflooding. 37

Figure 4.2: Comparative of numerical and analytical solutions for polymer flooding. 37

Figure 4.3: Behavior of ϵ_A *as a function of number of nodes in the grid for waterflooding. 38*

Figure 4.4: Behavior of ϵ_A *as a function of number of nodes in the grid for polymer flooding. 38*

Figure 4.5: Comparison of experimental and simulated data of polymer flooding test 1. Simulated data were obtained with the proposed model and CMG-STARS software. 40

Figure 4.6: Comparison of experimental and simulated data of polymer flooding test 1. Simulated data were obtained with the proposed model and CMG-STARS software. 41

Figure 4.7: Comparison of experimental and simulated data of polymer flooding test 2. Simulated data were obtained with the proposed model and CMG-STARS software. 41

Figure 4.8: Comparison of experimental and simulated data of water and polymer flooding test 4. Simulated data were obtained with the proposed model and CMG-STARS software. 42

Figure 4.9: Comparison of experimental and simulated data of water and polymer flooding test 5. Simulated data were obtained with the proposed model and CMG-STARS software. 43

Figure 4.10: Shear thinning and viscoelastic models fit to experimental data taken from Masuda. 44

Figure 4.11: Comparison of experimental and simulated data of polymer flooding with data from Masuda et al. Simulated data were obtained with the proposed model for shear thinning and viscoelastic behavior. 45

Figure 4.12 Saturation, chemical concentrations and viscosities versus distance, at $0.5PV$ *injected. . 47*

Figure 4.13: Efficiency recovery for different polymer concentrations versus injection flow rates. 48

Figure 4.14: Profiles for saturation and viscosity distribution, for different injection flow rates. 49

Figure 4.15: Profiles for saturation and viscosity distribution, for different polymer concentrations. 49

Figure 4.16: Recovery efficiency versus pore volume injected for different polymer concentrations and injection flow rates. 50

Figure 4.17: Recovery efficiency versus salinity concentration, for different polymer concentrations.. 51

Figure 4.18: Recovery efficiency versus pore volume injected for different polymer and salinity concentrations. 52

Figure 4.19: Profiles for saturation, effective salinity concentrations and apparent viscosity. 52

Figure 4.20: Profiles for saturation and salinity concentrations for different salinity injection strategies. 53

Figure 4.21: Recovery efficiency versus pore volume injected for different salinity injection strategies. 54

Figure 4.22: Profiles for saturation and adsorption concentrations, for 3 adsorption levels..... 56

Figure 4.23: Recovery efficiency versus pore volume injected for 3 adsorption level. 56

Figure 4.24: Profiles for end point water- oil mobility ration for different polymer concentration (C_{41}*) and permeability reduction factor (*R_k*). 58*

Figure 4.25: Saturation profiles and apparent viscosity distributions for different polymer concentration (C_{41}*) and permeability reduction factor (*R_k*)..... 59*

Figure 4.26: Recovery efficiency versus pore volume injected for different polymer concentration (C_{41}*) and permeability reduction factor (*R_k*). 59*

Figure 4.27: Profiles for saturation, chemical concentration and viscosities, at $0.5PV$ *injected with a slug size of* $0.25PV$*. 60*

Figure 4.28: Profiles for saturation and polymer concentration with a slug size of $0.25PV$ *and* $C_{41} = 0.1wt\%$*..... 61*

Figure 4.29: Profiles for saturation and polymer concentration with a slug size of $0.25PV$ *and* $C_{41} = 0.032wt\%$ *62*

Figure 4.30: Profiles for saturation and polymer concentration with a slug size of $0.08PV$ *and* $C_{41} = 0.1wt\%$ *62*

Figure 4.31: Recovery efficiency versus pore volume injected for three cases of slug injection. *63*

Figure 4.32: Profiles for saturation, polymer and adsorption concentrations with a slug size of $0.08PV$, $C_{41} = 0.1wt\%$ *and reversible adsorption.* *65*

Figure 4.33: Profiles for saturation, polymer, and adsorption concentrations with a slug size of $0.08PV$, $C_{41} = 0.1wt\%$ *and irreversible adsorption.* *66*

Figure 4.34: Recovery efficiency versus pore volume injected for reversible and irreversible adsorption. *66*

Figure 5.1: Flowchart of the numerical simulator for estimating pressure, saturations, and concentrations for a 2D distribution. *71*

Figure 5.2: Flowchart of the numerical simulator for polymer flooding by streamlines *77*

Figure 6.1: Comparison of experimental and simulated data for waterflooding. Simulated data were obtained with the proposed model and CMG-STARS software. *78*

Figure 6.2: Streamlines and time of flight obtained from the New SL Model, with the data reported in the literature (Douglas et al., 1959). *80*

Figure 6.3: Profiles for saturation at breakthrough time, with normalized time of flight, obtained from experiments $\mu_2/\mu_1 = 0.083$ *and* $\mu_2/\mu_1 = 754$. *81*

Figure 6.4: Profiles for saturation at breakthrough time, obtained from experiments a) $\mu_2/\mu_1 = 0.083$ *(left) and b)* $\mu_2/\mu_1 = 754$ *(right).* *81*

Figure 6.5: 3D view of saturation distribution at breakthrough time, obtained from the two experiments in Figure 6.4. ..... *82*

Figure 6.6: Comparison of analytical (Landrum and Crawford, 1960) and simulated data of waterflooding with directional permeability in a five-spot pattern. *83*

Figure 6.7: Streamlines and time of flight obtained from the New SL Model, with the data reported in the literature (Landrum and Crawford, 1960), for the cases a) $k_x/k_y = 1$ *(left) and b)* $k_x/k_y = 0.1$ *(right).* *84*

Figure 6.8: Comparison of published and simulated data for water and polymer flooding. Simulated data were obtained with the proposed model and CMG-STARS software. *86*

Figure 6.9: Comparison of simulated data for polymer flooding. Simulated data were obtained with the proposed model and CMG-STARS software. *87*

Figure 6.10: Profiles for saturation and polymer concentration at breakthrough time, with normalized time of flight, obtained from simulation case $^{\mu_2}/_{\mu_{1app}} = 16$. *88*

Figure 6.11: Saturation contours at breakthrough time, obtained from simulation case $^{\mu_2}/_{\mu_{1app}} = 16$ *a) New SL Model (left) and b) CMG-STARS (right).* *89*

Figure 6.12: Polymer concentration contours at breakthrough time, obtained from simulation case $^{\mu_2}/_{\mu_{1app}} = 16$ *a) New SL Model (left) and b) CMG-STARS (right).* *89*

Figure 6.13: Contour plots at breakthrough time, obtained from simulation case $^{\mu_2}/_{\mu_{1app}} = 16$ *with CMG-STARS and 40 x 40 cells: a) saturation (left) and b) polymer concentration (right).* *90*

Figure 6.14: Contour plots at breakthrough time, obtained from simulation case $^{\mu_2}/_{\mu_{1app}} = 16$ *with CMG-STARS and 80 x 80 cells: a) saturation (left) and b) polymer concentration (right).* *90*

Figure 6.15: Profiles for saturation at breakthrough time, with normalized coordinate, obtained from simulation case $^{\mu_2}/_{\mu_{1app}} = 16$. *91*

Figure 6.16: Profiles for polymer concertation at breakthrough time, with normalized coordinate, obtained from simulation case $^{\mu_2}/_{\mu_{1app}} = 16$. *91*

Figure 6.17: 3D saturation and concentration distributions at breakthrough time, obtained from simulation case in Figure 6.11. ..... *92*

List of tables

Table 1.1: Analytical models for 1D flow flooding. 3

Table 3.1: Polymer and reservoir data for 1D flow problem. 29

Table 4.1: Brief description of coreflood properties for laboratory polymer solution flooding. 39

Table 6.1: Brief description of five-spot model properties for laboratory waterflooding. 79

Table 6.2: Polymer and reservoir data for 2D field scale polymer flooding simulation. 85

Chapter 1: Introduction

1.1 Overview on polymer flooding

World average of total production from an oil reservoir after primary and secondary recovery is about one third of the original oil in place (OOIP) (Donaldson et al., 1985; Chierici, 1995; Green et al., 1998), so that significant volume of petroleum is left behind underground due to capillary forces, and viscous fingering (such as stratification, channeling, gravity segregation, etc.), hence nearly $2x10^{12}$ barrels of conventional oil and $5x10^{12}$ barrels of heavy oil will remain in reservoir (Thomas, 2008). Along with the growing energy demand around the world, Enhanced Oil Recovery (EOR) technologies need to contribute to increase the recovery from petroleum reservoirs. Now, because of many oil fields have been under waterflooding, Chemical EOR methods could be implemented with fewer additional facilities needed, compared with other EOR methods (Sheng, 2014). Polymer flooding is probably the most practical CEOR technology applied successfully at commercial scale for light or medium gravity oils (Chierici, 1995; Taber et al., 1997; Carcoana,1992; Dickson et al., 2010), and also in combination with horizontal wells for heavy-high viscous oils (from 600 to $2{,}000cP$), where thermal methods are not economically applicable (Wassmuth et al., 2009; Delaplace et al., 2013; Delamaide et al., 2014). Beyond the screening criteria applications, polymer flooding is a good candidate for improving oil recovery and has been successful at commercial scale for a wide range of oil viscosities.

Polymer flooding process improves waterflooding, because of a polymeric solution increases the viscosity of the displacing water and decreases the mobility ratio, thereby decreasing viscous fingering. From experimental data, polymer adsorption onto rock surface causes reduction of effective permeability to water, contributing to increase volumetric sweep efficiency and reduce water cut (Sorbie, 1991; Sheng, 2011; Lake, 1989). From field experience, successful projects have been reported with considerable permeability reduction (Standnes et al., 2014), such as the successful flood in ShuangHe oilfield (He et al., 1998), which reported resistance factor values, R_F, in the range from 20 to 60 and, reported residual resistance factor values, R_{RF}, in the range from 3 to 13.5.

The benefits to improve sweep efficiency by polymers have been carried out along with other EOR technologies, combining the mobility control with the enhancement of microscopic displacement efficiency, by reducing oil-water interfacial tension with surfactant injection or by wettability alteration through alkaline flooding (Sheng, 2011; Olajire, 2014), nanoparticles flooding (Kamal et al, 2017) and low salinity water injection (Kakati et al., 2020; Vermolen et al., 2014; Shiran and Skauge, 2013). Besides, there are other endeavors to apply polymer flooding to more unfavorable environments such as high-temperature, high-salinity carbonate reservoirs (Hashmet et al., 2017), pH-sensitive polymer conditions (Kazempour and Alvarado, 2011) and formations with active clays (Kazempour et al., 2013), where geochemical description is recommended to be considered in the modeling. Seright (2017) examined and published a review of previous and current practices, where discussions with many operators and designers of current polymer floods revealed substantial differences of opinion for the appropriate way to design a polymer flood. Therefore, polymer flooding is a mature and versatile technology that can be combined with other EOR methods, be applied on a wide variety of reservoir conditions, and can be designed under different strategies to increase the recovery efficiency and profitability.

To find the optimum conditions of applying polymer flooding, a predictive model that represents physical and chemical behavior during displacement processes is a helpful tool. Polymer flooding entails phenomena such as rheology, salinity variation, permeability reduction and adsorption. Some of the first multicomponent-multiphase displacement mathematical models for chemical flooding were presented by various authors (Pope et al.,1978; Helfferich, 1981; Hirasaki, 1981), where models for polymer viscosity behavior did not consider shear rate nor salinity concentration dependence, the adsorption behavior was not included; salinity concentration, and permeability reduction was neglected. Hirasaki and Pope (1974) discussed and proposed a model for adsorption and for dilatant behavior with viscoelastic properties of the polymer solution.

After, with considerable simplifications several authors introduced analytical solutions to one dimensional water and polymer flooding problem such as; Buckley and Leverett (1942), (BL), and Welge (1952) described the classical frontal advance behavior for waterflooding, Pope (1980) presented the application of fractional flow theory to EOR, Sorbie (1991) and Lake (1989) documented the solution to the convection-dispersion equation for polymer transport, and more recent works have presented analytical expressions (Shapiro et al.,

2004; Vicente et al., 2014; De Paula and Pires, 2015; Borazjani et al., 2016; Abdul-Hamid and Muggeridge, 2018) for 1D polymer injection (Table 1.1). Although analytical methods cannot represent all the required physics of multiphase flow for EOR processes, they could draw a rough image of the flooding performance that help to build a decision framework for proceeding to support a decision (Alvarado et al., 2010).

Reference	Comments
(Pope, 1980)	Continuous polymer injection; constant viscosities; $\hat{C}_4$ is represented by constant retardation.
(Sorbie, 1991)	Continuous polymer injection; constant dispersion coefficient and Q; $\hat{C}_4$ is a linear isotherm.
(Shapiro et al., 2004)	Continuous chemical injection; aqueous multicomponent solution; constant viscosities; variable $\hat{C}_4$.
(Vicente et al., 2014)	Semi-analytical; slug polymer injection; aqueous viscosity is linear with C_{41}; $\hat{C}_4$ is a Langmuir isotherm.
(De Paula and Pires, 2015)	Slug polymer injection; salinity variation; constant viscosities; $\hat{C}_4$ is a Langmuir isotherm with salt effect;
(Borazjani et al., 2016)	Slug polymer injection; salinity variation; non-Newtonian behavior; linear Henry's sorption.
(Abdul Hamid et al., 2018)	Slug polymer injection; viscous fingering by Todd and Longstaff; absence of adsorption.

Table 1.1: Analytical models for 1D flow flooding.

Unlike analytical methods, reservoir simulation allows modelling more complex physical and chemical principles, and reservoir conditions under specific development strategies. Then, at the beginning of the 70s some of the numerical models were presented (Patton et al., 1971; Bondor et al., 1972) that, with basic relations, took into account the polymer content effect on polymer adsorption, aqueous viscosity and polymer slug. Later, in 1978, in a chemical flooding compositional simulator, Pope et al. (1978) considered salinity as a component in the continuity equation but not in the polymer-rich phase viscosity or polymer adsorption. For economic analysis, by 1984 some researchers developed a prediction tool (Jones et al., 1984) for polymer flooding which incorporated methods used in both; simplified and sophisticated prediction tools, by combining a 2D cross sectional model with area sweep correlations, and injectivity functions. Based on the BL equation, Masuda et al. (1992) proposed a simple simulation model including the viscoelastic effect of polymer solution. In 1996 Delshad et al. (1996) described the formulation of a general chemical compositional

simulator named UTCHEM. Zheng et al. (2000) introduced a new empirical model for relative permeability reduction as a function of polymer adsorption, and a model for shear rate based on mobility measurements. As the application of polymer flooding extended to viscous oils with polymers at high concentrations and with very high molecular weights, a mechanistic understanding of polymer rheology and accurate numerical modeling were essential. This led to improvements in the understanding of polymer rheology incorporating apparent viscosity models (Delshad et al., 2008) that account for both shear-thinning and shear-thickening behavior of polymers in porous media. A critical review of the existing viscoelastic models was carried out (Azad and Trivedi, 2019) and presented the deficiencies of different methodologies used for quantifying the viscoelastic effects by polymer flooding. Nowadays, models and correlations developed for polymer flooding have been the basis for modeling specific problems. Manzoor (2020) studied the effect of injection pressure on flooding performance in one-dimensional mathematical model that considers several phenomena, neglecting the shear rate and salt effects on apparent viscosity.

Even in coreflooding laboratory scale, commercial and academic reservoir simulators for CEOR applications such as CMG- STARS, ECLIPSE, and UTCHEM require more detailed information (related to fluids, components, reservoir properties, and operational conditions) and imply more economic resources than simplified numerical models. Additionally, for preliminary decision-making processes, such as in the early stages of EOR process selection and laboratory investigations, a practical tool that captures the basic physical and chemical phenomena involved in the CEOR process is required.

According to Hite et al. (2004) a successful EOR project depends on good planning and should avoid spending considerable time and effort on projects that have no hope of achieving adequate profitability. Screening studies should identify candidates thus only focusing on worthy opportunities. Therefore, EOR predictive tools with different degree of accuracy [from statistical techniques (Alvarado et al., 2010; Rai et al., 2009) to reservoir numerical simulation] interact with economics, engineering planning and data collection, and should go hand-in-hand at each step for an effective EOR project management.

This thesis has developed a one-dimensional, multiphase, compositional mathematical model, based on fractional flow theory that considers Non-Newtonian rheology (shear thinning and viscoelasticity), permeability reduction, irreversible or reversible polymer adsorption, as a function of polymer and salinity concentrations. The model includes four

components [water, oil, polymer and salinity (total monovalent anions)] and two phases (aqueous and oleic). Some limitations are temperature variations, mechanical degradation, and water hardness. The resulting non-linear mathematical system is solved numerically by using a finite-difference formulation with fully implicit scheme in time and central differences in space. The numerical algorithm was validated by: 1) analytical solutions of BL (Buckley and Leverett, 1942; Lake, 1989) for waterflooding and the extension of the fractional flow theory for polymer flooding (Pope, 1980; Sorbie, 1991), 2) laboratory experiments reported by Koh et al. (2018) for waterflooding and polymer flooding where oil viscosities from 72 to $1{,}050cP$ were simulated, and by Masuda et al. (1992), for viscoelastic rheology, and 3) a CMG-STARS model built as a reference for water and polymer flooding.

Additionally, with the one-dimensional model, this work analyzes the interaction of the main phenomena involved in polymer flooding processes, investigating the effects of controlling flow properties on saturation and composition profiles, as well as, on breakthrough time and recovery efficiency. Chemical injection strategy is deemed vital for the success of flooding (Druetta and Picchioni, 2018), in either continuous or slug modalities.

1.2 Overview on streamline modeling

The 1D model developed can be extended to more dimensions through the application of the streamline concept. This is based on the description of flow paths that particles follow when a fluid flows from an injection to a production well. The beginnings of the streamline modeling take us back to the analytical treatment in the works of Muskat and Wyckoff (1934), and Muskat (1937), where they considered a steady flow of immiscible phases with unit mobility ratio (as a “single phase”) to estimate recovery efficiency. By treating channels between streamlines as one-dimensional conduits, some authors (Higgins and Leighton, 1962) applied the BL theory in a computer method built to rapidly calculate the performance of the waterflood, and because every stream channel has different characteristics, they included a shape factor that was determined from a potentiometric model. This model was utilized by Patton et al. (1971) and they extended the application to polymer flooding by considering the aqueous viscosity as a linear function of polymer concentration and irreversible adsorption in a five-spot flood. An alternative to estimate streamlines was introduced by publications (Morel-Seytoux, H. J., 1965, 1966), which consist of an analytical-numerical technique to approximate the pressure distribution and streamfunction in several flow geometries for waterflooding predictions was described. Later, LeBlanc and Caudle

(1971) proposed a computational model for secondary recovery, in which the flow through a stream channel was represented by the fluid velocities along the streamline (SL) in the center of the channel, and the model required no prior knowledge of the streamlines or stream channels to be used, so a shape factor was no needed; furthermore, the BL solution for frontal displacement was assumed within each streamline. A development of a streamline model for micelar-polymer simulation was carried out by Wang et al. (1981), by considering fixed and unit mobility ratio streamlines, calculated using source and sink equations with the method of image wells, in doing so, they obviated the need to solve the pressure equation and solved along each streamline, with finite-difference, the conservation equation of Pope et al. (1978) for multicomponent, multiphase flow. Pollock (1988) proposed a semianalytical computation procedure for particle tracking to determine the curved particle path lines within individual grid cells. This method is thought of as semianaitical since the overall paths of a particles is the summation of a series of analytically determined path lines for the individual grid cells.

Datta-Gupta and King (1995) introduced a semianalytic approach to modeling a tracer movement in permeable media, based on the velocity field and its approximation by piecewise hyperbolic intervals for the estimation of streamlines. This provides a better resolution than conventional particle tracking. Some aspects of this model were used by Peddibhotla et al. (1996) to propose a streamline simulator focused on a 3D, multiphase flow in waterflooding field performance prediction, demonstrated through the application to synthetic and field cases. Bratvedt et al. (1996) presented a streamline simulator for incompressible, two-phase flow in three dimensions, where the front tracking method was used and the effects of gravity were accounted for in a separate correction step, by considering a new operator splitting technique based on a physical approach. After, an investigation (Batyckty et al., 1997) published a 3D streamline-based simulator that accounted for changing well conditions, well conversion, heterogeneity, mobility, and gravity effects. The contribution of this model was that the fluid transport occurred on a streamline grid rather than the grid blocks on which the pressure distribution is solved.

Later, the utility of the streamline-based models encompassed applications beyond conventional waterflooding. Crane and Blunt (1999) extended the streamline method to the solute transport simulation in 3D heterogenous aquifers, single-phase, multicomponent, by considering a conservative, sorbing and decaying tracer flow; a four-component radioactive

decay chain and saltwater intrusion with a time varying flow field. A publication by Jessen and Orr (2002) presented a compositional streamline simulation and reported results of combining an analytical 1D solution for multicomponent miscible gas injection with a representation of flow along streamlines to capture the effects of heterogeneity. Di Donato et al. (2003) documented a streamline-based dual porosity simulator to model waterflooding in fractured reservoirs, where the fracture/matrix transfer is modeled as a source/sink term in the 1D conservation equation along the streamlines. Seto et al. (2007) applied analytical solutions in a compositional streamline simulation to model a real field scale project, and they demonstrated that the compositional streamline technique is an efficient computational method for modeling CO_2 storage and condensate vaporization in gas reservoir. Zhu et al. (2009) explored the extension of streamline simulation to thermal recovery processes, where they included temperature dependent viscosity and accounted for thermal expansion; results for the case of 2D heterogeneous quarter five-spot problems, compared favorably with those obtained from commercial thermal simulator.

An extension of streamline simulation to field scale polymer flooding was presented by Thiele et al. (2010), in which they considered water viscosity, Langmuir isotherm, and shear rate dependence with shear-thinning effect, all as a function of polymer concertation, neglecting salinity effects. AlSofi and Blunt (2010) extended the streamline simulator based on the work of Batyckty et al. (1997) to explore the effects of non-Newtonian rheology on field scale polymer flooding performance; their rheology model can be defined for shear thinning and shear thickening regimes, and adsorption is modeled by a linear isotherm, all this by ignoring salinity composition.

A number of field case studies, based on streamline simulation models, have been reported for efficient implementation and management of polymer flooding projects. Clemens et al. (2010) documented a management methodology on a Romanian oil field to show that the utility factor can be reduced while sustaining recovery. Vicente et al. (2012) developed a streamline simulator to model a 2D, heterogeneous or homogenous medium, two-phase oil displacement by polymer slugs, by considering adsorption with Henry or Langmuir isotherms, in which analytical solutions of the transport equation along streamlines were used. A publication presented by Choudhuri et al. (2015) a full field streamline simulation model of a large polymer flooding project in the Sultanate of Oman, to facilitate the reservoir management decision-making and optimization of the polymer flood strategy. Chen et al.

(2020) used a heuristic method with a streamline-based rate allocation approach to maximize oil recovery in an ongoing polymer flood in the Mangala field, in India; they applied a streamline flow diagnostic for rate allocation and optimization of the polymer flood at field-scale; also developed a framework to incorporate dynamic field development schemes and operational constrains. Later, Li et al. (2022) introduced an application of streamline-based polymer flooding injection optimization for the Mangala field in India, using a systematic rate optimization workflow designed for practical field implementations.

As indicated, the application of streamline technique has proved to be an effective reservoir simulation tool for the design and management of polymer flooding projects, so this research developed a one-dimensional model described previously, extending it to a two-dimensional streamline-based model aiming at having a practical tool for the comprehensive modeling of key phenomena that influence polymer flooding, such as rheology (shear thinning and shear thickening), salinity variation, permeability reduction, and irreversible-reversible polymer adsorption. Previously published streamline multidimensional models for polymer flooding lack of the integrated modeling of the above mentioned key phenomena. For the streamline-based approach, a black oil formulation was considered to estimate the pressure and saturation 2D distributions by applying the IMPES method, coupled with an explicit formulation for the 2D composition computation. For the saturation-composition along the streamlines, the 1D validated practical tool mentioned previously was incorporated, as well as its functionality to represent polymer flooding key phenomena. The numerical algorithm is supported by 1) laboratory experiments reported by Douglas et al. (1959) for waterflooding in homogenous medium, 2) analytical results (Landrum and Crawford, 1960) for waterflooding in heterogeneous medium, 3) a polymer flooding field scale simulation case of the literature (Qi et al. 2018), 4) a CMG-STARS model built as a reference for waterflooding in homogenous and heterogeneous medium, and for polymer flooding.

1.3 Outline of the dissertation

This research is organized as follows. First, fundamental concepts for polymer flooding are described, and the mathematical flow model for 1D polymer flooding is derived. Second, the resulting system of equations are discretized with finite-difference and the numerical flow model is described. Then, the numerical model and algorithm are validated by well-known 1D analytical solutions, laboratory experiments and commercial simulator results. Third, the flow dynamics and recovery efficiency behavior of polymer flooding by saturation and

concentration distribution under different flow parameter scenarios were investigated. Fourth, a streamline-based model for 2D polymer flooding was developed, applying finite differences with IMPES to estimate the 2D pressure and saturation distribution, along with an explicit formulation for the 2D composition estimation. This was coupled with the 1D numerical model adapted to use along streamlines. Fifth, the numerical algorithm was validated by laboratory experiments, analytical solution results, published results from field-scale numerical simulation and commercial simulator results. Finally, the dissertation concludes with the interpretations of results.

Chapter 2: Fundamentals of polymer flooding

2.1 Concepts of waterflooding

2.1.1 Surface tension and interfacial tension

In petroleum recovery processes where immiscible phases are present, a surface energy influences phase distributions and oil recovery. The molecules that are at or near the surface that separates the immiscible phases (for example liquid/air interface), on average, are attracted unequally in all directions owing to cohesive forces, and their movement therefore tends to be affected by cohesive forces. A net force away from the surface tends to pull these molecules in to the bulk of the liquid. The surface thus acts like a stretched membrane, tending to shorten as much as possible (Green et al., 1998).

This surface force is quantified in terms of surface tension, σ, the force acting in the plane of the surface per unit length of the surface, required to create additional surface area. Thus, the work or energy needed to separate or create additional surface is directly proportional to σ (Bear, 1972; Scheidegger, 1974). The term “surface tension” usually is reserved to the case in which the surface is between a liquid and its vapor or air. If the surface is between two different liquids, or between a liquid and a solid, the term “interfacial tension” (IFT) is used.

IFT’s between oil and water are usually in the order of 10 to 30 dynes/cm at 77 °F. Interfacial tension is a measure of immiscibility: the lower the IFT, the closer two phases approach miscibility. Low IFT´s are also observed in systems containing alcohols and surfactants. Values of 10^{-5} dynes/cm have been reported for some formulations. IFT’s less than 10^{-3} dynes/cm are referred to as ultralow tensions (Willhite, 1986).

2.1.2 Wettability

Fluid distribution is also affected by forces at fluid/solid interfaces. When two immiscible phases are placed in contact with a solid surface, one phase (wetting phase) usually is more strongly attracted to the solid than the other. Then, wettability is the tendency of one fluid to spread out on or adhere to a solid surface in the presence of a second fluid, and hence relative permeability curves are strong functions of rock wettability in a fluid/rock system

(Green et al., 1998). A simple example of the effect on saturation is shown in Figure 2.1, which shows residual oil saturation location in a strongly water-wet and a strongly oil-wet rock.

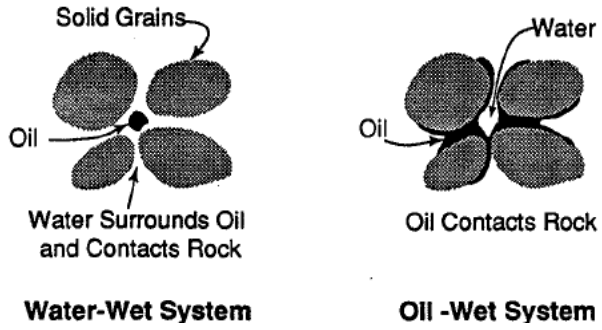

Figure 2.1: Effect of wettability on saturation, (Green et al., 1998).

Rocks could have intermediate and/or mixed wettability, depending on the physical/chemical makeup of the rock, the composition of the oil phase, the salinity and type of salts in the water phase. Intermediate wettability occurs when both fluid phases tend to wet the solid, but one phase is only slightly more attracted than the other. Mixed wettability results from a variation or heterogeneity in chemical composition of exposed rock surfaces or cementing material surfaces in the pores.

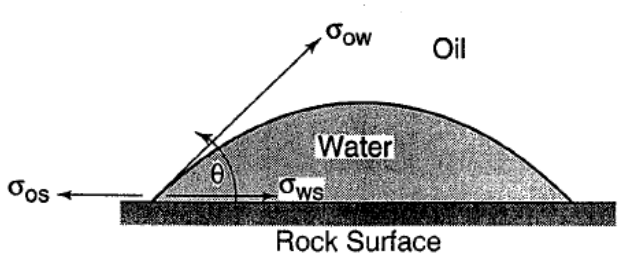

Figure 2.2: Interfacial forces at an interface between two immiscible fluids and a solid, (Green et al., 1998).

By examining the interfacial forces that exist when two immiscible fluid phases are in contact with a solid. Figure 2.2 shows the balance of the interfacial forces acting, and a force balance at the horizontal axes in the intersection of solid, water, and oil yields the expression

$$\sigma_{os} - \sigma_{ws} = \sigma_{ow} \cos\theta \qquad (2.1)$$

where σ_{os}, σ_{ws}, and $\sigma_{ow} = IFT's$ between soild and oil, water and solid, and water and oil, respectively, and θ is the contact angle, measured through the water phase.

2.1.3 Capillary pressure

This concept comes from the representation of capillary phenomena in the standard physics experiment in which a capillary tube in inserted into a container of water, and the water raises inside the tube (Craig, 1971). An oil/water interface in a large diameter tube is flat because the wetting forces at the walls of the tube are distributed over a large perimeter, and thus the pressures of the fluids at the interface are equals (Willhite, 1986). Pores in a rock are analogous to capillary tubes in that the diameters are small, and surface forces induced by preferential wetting of the solid extend over the entire interface, causing measurable pressure difference between the two immiscible fluid phases across the interface, and this pressure difference is the capillary pressure in porous media.

$$P_C = P_{nw} - P_w \tag{2.2}$$

where P_{nw} is the pressure in the nonwetting phase and P_w is the pressure in the wetting phase. Then, capillary pressure is a measure of the tendency to absorb the wetting fluid and repeal the nonwetting in the porous media.

Fluid distribution within the rock pores of given wettability depends upon the direction of the saturation changes (Craig, 1971). The term *hysteresis* is applied to the difference in multiphase fluid-rock properties that depends upon the direction of saturation change within a porous space. Because of hysteresis, different capillary pressure curves are obtained, depending on the initial saturation condition, flow direction and saturation history in the porous space.

2.1.4 Relative permeability

The concept of permeability is established for the flow of a single phase through a porous media. To extend the flow equations from one phase to a multiphase flow, the concept of relative permeability was developed.

Experimentally, it has been determined that when two immiscible fluids are flowing simultaneously through a porous media, each fluid has its own effective permeability. These

permeabilities are dependent on the saturations of each fluid and the sum of the effective permeabilities is always less than the absolute permeability (Dake, 1978).

For the water relative permeability curve behavior, two saturation states are important; the connate or irreducible water saturation where water will not flow, and when the water saturation reaches the maximum value where we get the maximum water relative permeability (end-point water relative permeability). In general, the relative permeability to a phase decrease as the saturation of that phase decreases.

Relating to relative permeability, it is important to describe definitions, such as, to distinguish the residual oil saturation from the remaining oil saturation. The residual oil saturation is the remaining behind in a thoroughly water swept region of the permeable media; while the remaining oil saturation is the oil left after a waterflood, well-swept or not. The trapped water saturation is the irreducible water saturation. It is not the connate water saturation, which is the water saturation in a reservoir before any water is injected, although many times irreducible is equal to connate water saturation (Lake, 1989).

Endpoint relative permeabilities are two other important aspects. These are the constant relative permeability of a phase at the other phase's residual saturation, and they are a consequence of the wettability. The nonwetting phase occurs in isolated globules several pore diameters in length that occupy the central part of the pores. Trapped wetting phase, on the other hand, occupies the crevices between rock grains and coats the rock surfaces. Thus, we would expect the trapped nonwetting phase to be a bigger obstacle to the wetting phase than trapped wetting phase is to the nonwetting phase. Therefore, the wetting phase endpoint relative permeability is smaller than the nonwetting phase endpoint. The ratio of endpoint relative permeabilities is a good qualitative measure of wettability. Crossover saturation (saturation where equal relative permeabilities) of relative permeabilities is more appropriate indicator of wettability (Lake, 1989).

The main influence on the shapes of the relative permeability curves appears to be the wettability, that it is important to the creation of fluid flow paths and fluid distribution in the porous media, thus the hysteresis phenomena could be critical in some flow cases.

2.1.5 Mobility ratio

From the Darcy's law is observed a proportionality factor between fluid velocity and pressure gradient. This factor is known as mobility of a fluid and is defined as the effective permeability

divided by the viscosity of the phase (Craig, 1971; Sheng, 2011). For multiphase flow, it is important to relate the mobilities of each phase, then mobility ratio is defined as:

$$M = \frac{k_d}{\mu_d}\frac{\mu_o}{k_o} \tag{2.3}$$

Where the subscript *d* denotes the displacing phase, and the subscript *o* is for oil (in general we can use the concept of displaced phase).

For the application of the mobility ratio concept, it is important to consider if the saturation gradient plays a key role. Craig et al. (1955) presented results of waterfloods and gas drives in five-spot patterns, and they found that if the water mobility were defined at the average water saturation behind the front flood at water breakthrough, the data on area sweep versus mobility ratio matched the results obtained by other investigators using miscible fluids. From these results, water mobility was defined as that at the water saturation in the water contacted portion of the reservoir, and it was widely accepted.

The mobility ratio is a dimensionless number that affects the stability of fluid displacement front; the displacement front is unstable and unfavorable when $M > 1$ (Craig, 1971; Green et al., 1998), and a process with $M < 1$ yields a favorable displacement. Commonly, a range of values reported in the literature for waterflooding is between 0.02 and 2.

2.2 Concepts of polymer flooding

2.2.1 Polymer

A polymer is a chemical that is composed of several individual molecules usually associated in a pattern that repeats itself throughout the length of each polymer. The repeating units are called monomers and the polymer can be either a homopolymer (one polymer), a dimer (two monomers), etc. Another common term used to represent the joining of two different monomers is copolymer (Donaldson et al., 1989).

The polymer used is a high-molecular-weight chemicals that are soluble in water because a hydrogen bonding between water molecules and the polymer's polar side chains. A water-soluble polymer at low concentration is used in petroleum operations to alter the flow of water in the reservoir by increasing the water viscosity and reducing the water relative permeability, this is referred as thickened water, and the associated drive process is called polymer flooding (Chierici, 1995).

For 1D floods it is only necessary to consider the microscopic efficiency of the waterflood at higher mobility rations ($M > 1$), since for $M \leq 1$, the flood shows virtually piston-like displacement with almost full recovery of oil at water breakthrough (Sorbie, 1991). Thus, there is little point in considering polymer to improve the displacement in this condition. Therefore, the role of polymer is to improve the microscopic displacement efficiency by lowering M, mainly by increasing the water viscosity, but also by lowering the aqueous phase permeability (pore blocking). Linear polymer flooding behavior is more complex because of the presence of a bank of (low viscosity) connate water which is driven in front of the injected polymer. This led to a double shock front behavior, that can be described with an extension of Buckley-Leverett theory (Pope, 1980).

For homogeneous areal system, the behavior is similar to the 1D case discussed previously. At lower M, the microscopic displacement is good, and thus, the areal sweep is good. As M increases the displacement efficiency is reduced, and an instability may develop in the fluid displacement, which leads to fingering of the lower viscosity water into the oil (viscous fingering). This is the areal bypassed oil that is the main target for polymer flooding. Therefore, the role of polymer is to reduce M, stabilize the areal flood and improve the microscopic displacement (Sorbie, 1991).

Vertical heterogeneity, such as high-permeability strata may be adjacent to much lower permeability layers. This leads to early water breakthrough in waterfloods and hence poor vertical sweep efficiency, even if mobility ratio is favorable. Then, the objective of polymer flooding is to reduce M, typically to 0.1 – 0.3 (Sorbie, 1991), thereby improving the vertical sweep efficiency as well.

2.2.2 Rheology

Rheology is the study of the deformation of matter due to flow (Morrison, 2001), and it is focused to analyze the behavior of complex fluids such as polymers, biological systems, suspensions, emulsions, and other compounds.

An important property of a fluid to define, is the viscosity, that it is the resistance of a fluid to shear. The relationship between shearing stress (τ_r) and the rate of deformation of the fluid ($\dot{\gamma}$) or shear rate defines the behavior of fluids. For some liquids the proportionality between these two parameters is constant over a wide range of deformation rate; this constant is the viscosity, and the fluid is known as Newtonian fluid (Sorbie, 1991). On the other hand, there

are several classes of fluid for which the viscosity does not remain constant at different rates of deformation, that are known as non-Newtonian fluids, and are described as follow:

$$\tau_r = \eta\dot{\gamma} \tag{2.4}$$

where η is a viscosity function that depends on the shear rate.

There are different types of fluids with diverse relationships between the shear stress and the strain rate (shear rate). The cases with constant slope correspond to Newtonian fluid. When the flow shows a smaller slope, or viscosity appears to be less, as the rate of strain increases, the fluids are known as shear thinning or pseudoplastic (Sorbie, 1991), generally, dilute polymers with low molecular weights belong to this category (Sheng, 2011). Fluids which show an increasing apparent viscosity are known as shear thickening or dilatant fluids, in which the flow is elongational or extensional.

Solutions for polymer flooding are generally pseudoplastic and a common way to plot this rheological behavior is with apparent viscosity against shear rate, as Figure 2.3 shows, where at low shear rates there is a maximum limiting viscosity, and at high shear there is another limiting viscosity that is generally taken as water viscosity (Sheng, 2011). For intermediate shear rates, it represents a power law relation.

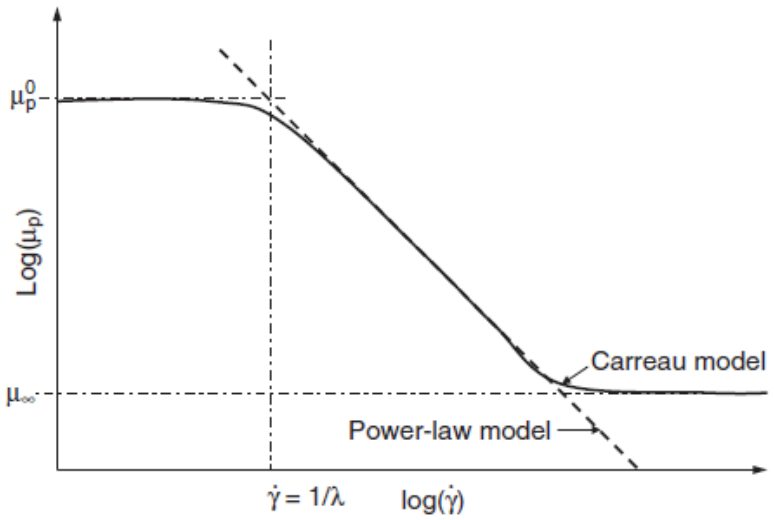

Figure 2.3: Viscosity versus shear rate for a typical pseudoplastic fluid flow behavior, (Sheng, 2011).

Another important property to discuss is the viscoelasticity that some polymer solutions show. This is the property that some materials exhibit to develop both viscous and elastic characteristics when undergoing deformation.

In the entire range of shear rates, a polymer solution viscosity could have three regimes, as Figure 2.4 shows. Below the first critical shear rate, the polymer solution behaves like a Newtonian fluid (the viscosity is independent of shear rate). At intermediate shear rate, between first and second critical shear rate, the polymer solution behaves like a pseudoplastic fluid. Above the second critical shear rate, the polymer solution behaves like a dilatant fluid (the viscosity increases with shear rate).

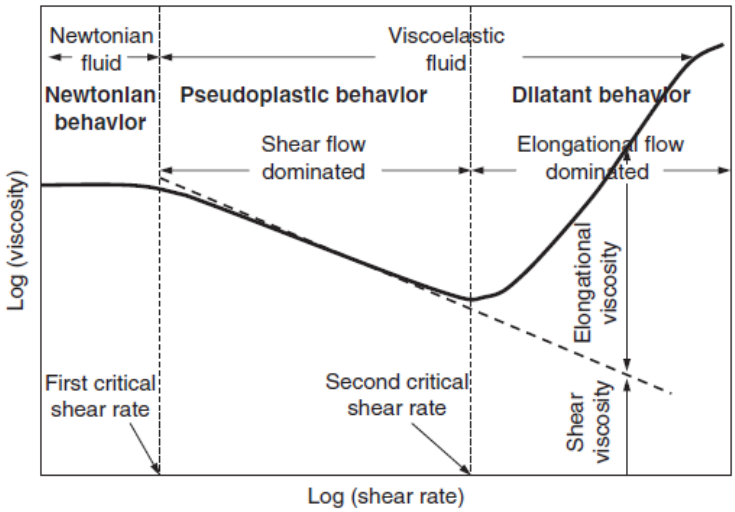

Figure 2.4: Schematic illustration of viscoelastic fluid flow behavior, (Sheng, 2011).

2.2.3 Polymer retention

In polymer flooding, there are interactions between the polymer molecules and the porous medium. Such interactions can cause a retention of the polymer in the porous rock, and this led to a detriment of the injected fluid slug with less polymer content and less viscosity compared to the initially injected polymer solution. Therefore, the retention level is an important factor to determine for field polymer applications (Sorbie, 1991).

There are three main retention mechanisms in polymer flooding (Sorbie, 1991; Sheng, 2011), illustrated schematically in Figure 2.5, and described as follows:

- Polymer adsorption. This is the main fundamental mechanism of polymer retention in porous media. It refers to the interaction between polymer molecules and solid surface; polymer molecules are bounded to the surface of the solid, mainly by physical adsorption, Van der Waals forces, and hydrogen bonding. Adsorption depends on the surface area exposed to the polymer solution.
- Mechanical entrapment. This mechanism only occurs in flow through porous media, where certain fraction of the network element would consist of narrow pore throats, and larger polymer molecules become lodged in narrow flow channels. The distribution of mechanical entrapped polymer along the formation rock should be largest close to the inlet and decrease exponentially along the core. Then, it is important to study the effective size of polymer molecules in solution.
- Hydrodynamic retention. This type comes from the experimental observations where the total level of retention changes when the fluid flow rate is adjusted to a new value; as the flow rate increases, more polymer is retained from the mobile aqueous phase. Here, some of the polymer molecules are thought to be trapped temporarily in stagnant flow regions by hydrodynamic drag forces. When the flow stops, these molecules may diffuse out into the main flow channels and, when the flow recommences, the polymer concentration in this region increases.

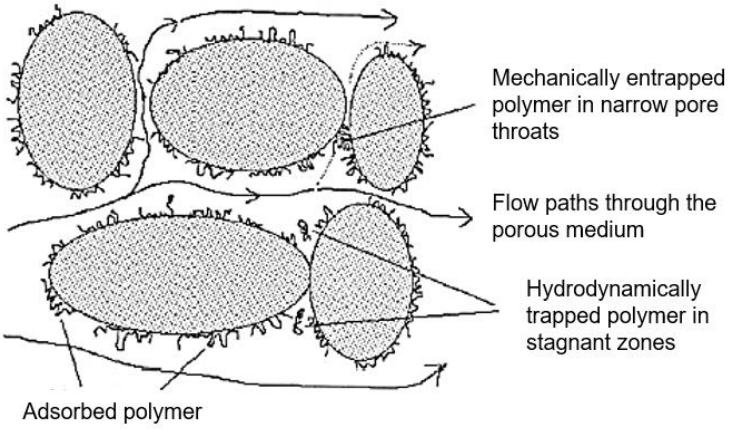

Figure 2.5: Schematic illustration of polymer retention mechanisms in porous media, (Sorbie, 1991).

From the three mechanisms of polymer retention, mechanical entrapment could be avoided by prefiltering the polymer or by applying the polymer in a high permeability formation.

Hydrodynamic retention is probably not a large contributor in the total retention and can be neglected in field applications (Sheng, 2011). Considering that adsorption is the most important mechanism, and because it is difficult to differentiate these three mechanisms in dynamic flood test, the term retention to describe polymer loss, sometimes may be referred to the term adsorption.

Polymer retention or the term adsorption may cause a permeability reduction (or pore blocking); rock permeability is reduced when polymer solution is flowing through it, compared with the permeability when only water is flowing. Therefore, permeability reduction must be evaluated and included in polymer flooding applications.

Chapter 3: Mathematical model for 1D polymer flooding

3.1 Mathematical modeling

3.1.1 Model assumptions

The key assumptions made for developing the one-dimensional model for multiphase multicomponent flow through porous media in a polymer flooding process are:

1. The problem is reduced to one-dimensional flow.
2. The medium is homogeneous and isotropic.
3. The system is isothermal.
4. All fluids and rock are incompressible, and effects of pressure on the equilibrium are negligible.
5. There are two immiscible phases and four components.
6. Fluid properties are function of composition only,
7. The phases are in local equilibrium,
8. There are no dispersive effects such as molecular diffusion, longitudinal and transverse dispersivities, convective dispersion, or capillary imbibition.
9. The adsorption isotherm has negative curvature, and it could be a reversible or irreversible process, depending on the case analyzed.
10. The permeability is reduced as a function of polymer concentration.
11. Gravity and capillary pressure are negligible.
12. Polymer and salt are transported only in the aqueous phase.
13. There are no changes in the inaccessible PV.
14. The rheological behavior can represent Newtonian, shear thinning and shear thickening behavior.

3.1.2 General flow model

To understand any EOR method, the mass conservation equations for component i, that includes the interaction with solid phase is described as:

$$\frac{\partial W_i}{\partial t} + \nabla \cdot \vec{J}_i = R_i \qquad (3.1)$$

where W_i is the overall concentration (accumulation), $\vec{J}_i$ is the flux and R_i the source-sink term. Incorporating the definitions of each variable:

$$\frac{\partial}{\partial t}\left[\phi \sum_{j=1}^{N_P} \rho_j S_j \omega_{ij} + (1-\phi)\rho_s \omega_{is}\right] + \vec{\nabla} \cdot \left[\sum_{j=1}^{N_P} \left(\rho_j \omega_{ij} \vec{u}_j - \phi \rho_j S_j \vec{\vec{K}}_{ij} \cdot \vec{\nabla} \omega_{ij}\right)\right] = \phi \sum_{j=1}^{N_P} S_j r_{ij} + (1-\phi)\, r_{is}, \qquad i = 1,2,\cdots,N_C \tag{3.2}$$

Considering incompressible fluids, constant porosity, ideal mixing, and other simplifications (Lake, 1989), the previous equation in one-dimensional form can be written as:

$$\frac{\partial}{\partial t}\left[\phi \sum_{j=1}^{N_P} S_j C_{ij} + (1-\phi) C_{is}\right] + u \frac{\partial}{\partial x}\left[\sum_{j=1}^{N_P} f_j C_{ij}\right] - \frac{\partial}{\partial x}\left[\sum_{j=1}^{N_P} \phi S_j K_{lij} \frac{\partial C_{ij}}{\partial x}\right] = 0 \quad , i = 1,2,\cdots,N_C \tag{3.3}$$

This equation includes the main effects that control the flow of fluids and components through porous media in a linear EOR processes (adsorption, gravity, capillarity, viscous, dispersion). The equation must be solved simultaneously with Darcy's law, the definitions of relative mobility, capillary pressure, volume fractions, phase saturations, equations of states, phase equilibria relations and dispersion.

Authors (Lake, 1989; Pope, 1978; Helfferich, 1981; Hirasaki, 1981; Rosado et al., 2022) have presented a special form of equation 3.3 to represent the physicochemical characteristics of oil and water displacement under a chemical EOR process, which in dimensionless form becomes,

$$\frac{\partial}{\partial t_D}\left[C_i + \hat{C}_i\right] + \frac{\partial F_i}{\partial x_D} = 0, \qquad i = 1,2,\cdots,N_C \tag{3.4}$$

were

$$x_D = \frac{x}{L} \tag{3.5a}$$

$$t_D = \frac{u}{\phi L} t \tag{3.5b}$$

C_i= Overall fluid phase concentration of component i $= \sum_{j=1}^{N_P} S_j C_{ij}$ (3.6a)

$\hat{C}_i$=Rock phase concentration of i on a pore volume basis.

F_i= overall flux of component j $= \sum_{j=1}^{N_P} f_j C_{ij}$ (3.6b)

$$f_j = \frac{\lambda_{rj}}{\sum_{j=1}^{Np} \lambda_{rj}} \tag{3.7}$$

3.1.3 Model for polymer flooding

The mathematical model based on fractional flow theory for linear polymer flood with salinity variation, consists in four equations expressing conservation of mass for each component. The common notation (Lake, 1989; Pope, 1978) for chemical flooding is adopted, so that, the four components are water (1), oil (2), polymer (4), and salinity or total monovalent anions (5).

Considering equations (3.4) to (3.6) coupled with the assumptions listed, the resulting system of equations can be reduced to the following system of nonlinear equations:

$$\frac{\partial}{\partial t_D}[S_1] + \frac{\partial}{\partial x_D}[f_1] = 0 \tag{3.8}$$

$$\frac{\partial}{\partial t_D}\left[C_{41}S_1 + \hat{C}_4\right] + \frac{\partial}{\partial x_D}[f_1 C_{41}] = 0 \tag{3.9}$$

$$\frac{\partial}{\partial t_D}[C_{51}S_1] + \frac{\partial}{\partial x_D}[f_1 C_{51}] = 0 \tag{3.10}$$

Fractional flow is a function of saturation and concentrations, and as specified in equation (3.7),

$$f_1 = \frac{\lambda_{r1}}{\lambda_{r1}+\lambda_{r2}} \tag{3.11}$$

Relative mobilities for both phases are:

$$\lambda_{r1} = \frac{k_{r1}}{\mu_1 R_k} \tag{3.12a}$$

$$\lambda_{r2} = \frac{k_{r2}}{\mu_2} \tag{3.12b}$$

Polymer flooding causes a degree of permeability reduction that decreases mobility, in addition to the increase of viscosity of the polymer solution (Lake, 1989). The polymer solution viscosity is modeled by the permeability reduction factor, R_k, to account for the reduction of permeability (Sheng, 2011).

Equation (3.12a) considers the permeability reduction effect, R_k. For relative permeabilities, Corey-type equations are used (Lake, 1989; Pope, 1978; Hirasaki, 1981; UTCHEM-9.0, 2000) as follow:

$$k_{rj} = k_{rj}^{*}[S_{nj}]^{e_j} \tag{3.13}$$

The normalized saturation is defined as

$$S_{nj} = \frac{S_j - S_{jr}}{1 - S_{1r} - S_{2r}} \tag{3.14}$$

Combining equations (3.11), (3.13) and (3.14), the fractional flow of water is

$$f_1 = \frac{M^{*} S_{n1}^{e_1}}{M^{*} S_{n1}^{e_1} + (1 - S_{n1})^{e_2}} \tag{3.15}$$

where $M^{*}$is the end point water-petroleum mobility ratio with permeability reduction, defined as:

$$M^{*} = \frac{k_{r1}^{*}/(\mu_1 R_k)}{k_{r2}^{*}/\mu_2} = \frac{k_{r1}^{*}\mu_2}{k_{r2}^{*}(\mu_1 R_k)} \tag{3.16}$$

The advantages of polymers as water mobility control agents in porous media are indicated by large permeability reduction factor values and the increment of aqueous phase viscosity. This can be used in profiles improvements to plug the more permeable streaks near injectors and to reduce permeability variation (Carcoana, 1992).

Permeability reduction is caused by polymer adsorption. The most used in numerical simulation is the Langmuir-type mathematical expression (Sheng, 2011; UTCHEM-9.0, 2000), that even though is not always the best choice, the flow model considers the option of irreversible adsorption and we took into account the recommendation of (Zhang and Seright, 2014) to reduce incorrect predictions; to reached the Langmuir plateau at very low polymer concentrations, polymer front to be sufficiently sharp, and relatively high polymer concentration. This model for adsorption could present inaccuracies in the dilute level for polymer solution, according to Zhang.

$$\hat{C}_4 = min\left[\tilde{C}_4, \frac{a_4(\tilde{C}_4 - \hat{C}_4)}{1 + b_4(\tilde{C}_4 - \hat{C}_4)}\right] \tag{3.17}$$

with the dependence of polymer and salinity concentrations by the following relation.

$$a_4 = (\alpha_1 + \alpha_2 C_{SEP})\sqrt{(k_{ref}/k)} \tag{3.18}$$

where the effective salinity is expressed as

$$C_{SEP} = C_{51}/C_{11} \tag{3.19}$$

The Langmuir-type model is reversible in terms of polymer concentration. When polymer adsorption needs to be irreversible, it requires tracking the adsorption history to detect decrements of polymer concentration (Sheng, 2011).

For the polymer rich phase, viscosity considers the influence of polymer concentration and effective salinity by the modified Flory-Huggins equation (Sheng, 2011; UTCHEM-9.0, 2000).

$$\mu_1^o = \mu_1\left[1 + \left(a_{p1}C_{41} + a_{p2}C_{41}^2 + a_{p3}C_{41}^3\right)C_{SEP}^{Sp}\right] \tag{3.20}$$

The rheology of polymeric solutions for polymer flooding are generally pseudoplastic and the viscosity related to this type of flow is shear thinning viscosity (μ_{1sh}); the apparent viscosity appears to be less at increasing shear rates (Sorbie, 1991). The shear thinning behavior of the polymer solution is caused by the uncoiling and unsnagging of the polymer chains when they are elongated in shear flow (Lake, 1989). To capture polymer solution viscosity and shear rate relationship, the Carreau equation (Sorbie, 1991; Sheng, 2011; Morrison, 2001) was used, equation (3.21a). Another type of flow is elongational, or extensional, when the fluid flows through a series of pore bodies and throats in a porous media. In this type of flow, the apparent viscosity is increased as the shear rate increases, and the viscosity related to this flow is shear thickening viscosity or elongational viscosity, μ_{1el}, (Sheng, 2011), that could be represented with the model developed by (Masuda et al., 1992), equation (3.21b).

$$\mu_{1sh} = \mu_\infty + (\mu_1^o - \mu_\infty)\left[1 + \left(\lambda\dot{\gamma}_{eq}\right)^\alpha\right]^{(n_C-1)/\alpha} \tag{3.21a}$$

$$\mu_{1el} = \mu_{1sh}C^*{\dot{\gamma}_{eq}}^{m_C} \tag{3.21b}$$

$$\mu_{1app} = \mu_{1sh} + \mu_{1el} \tag{3.21c}$$

$$\mu_{1app} = \begin{cases} \mu_\infty + (\mu_1^o - \mu_\infty)\left[1 + \left(\lambda\dot{\gamma}_{eq}\right)^\alpha\right]^{(n_C-1)/\alpha}, & pseudoplastic\ fluid \\ \left\{\mu_\infty + (\mu_1^o - \mu_\infty)\left[1 + \left(\lambda\dot{\gamma}_{eq}\right)^\alpha\right]^{(n_C-1)/\alpha}\right\}\left[1 + C^*{\dot{\gamma}_{eq}}^{m_C}\right], & viscoelastic\ fluid \end{cases} \tag{3.21d}$$

where μ_∞ is the viscosity at high shear limit that generally is taken as water viscosity, α affects the shape transition region between the zero shear rate plateau and the rapidly decreasing portion, and is generally taken (Sheng, 2011) to be *2*, λ is a parameter for material relaxation time correlated with molecular structure (Morrison, 2001) and it determines the shear rate at which the transition occurs from zero shear rate plateau to power law portion, and n_C is the exponent for power-law like. The parameter $C^* = C_M t_r^{m_C}$, depends on the empirical constant C_M and the relaxation time of the fluid t_r (that is considers constant), then C^* and m_C are empirical constants determined by flow experiment of the fluid through porous media (Masuda et al., 1992). To describe the viscosity in the entire shear rate range we consider two parts: shear-viscosity-dominant part (μ_{1sh}), and elongational-viscosity-dominant part μ_{1el}, equation (3.21c). Therefore, the model considers a rheology with pseudoplastic or pseudoplastic and elongational contributions, as equation (3.21d) specified.

Shear rate ($\dot{\gamma}$) is an equivalent shear rate for flow in permeable media applications ($\dot{\gamma}_{eq}$), and it could be modeled as (Sorbie, 1991; UTCHEM-9.0, 2000), but to consider the applicability of the model to low permeability porous formations (Sheng, 2011), an expression that includes permeability reduction was chosen (Wang and Liu, 2014; Sharafi et al., 2016):

$$\dot{\gamma}_{eq} = \dot{\gamma}_c \frac{u}{\sqrt{k k_{r1} S_1 \phi / R_k}} \tag{3.22}$$

The permeability reduction factor is defined (UTCHEM-9.0, 2000) as:

$$R_k = 1 + (R_{kmax} - 1)\frac{b_{kr} C_{41}}{1 + b_{kr} C_{41}} \tag{3.23}$$

where

$$R_{kmax} = \left[1 - \frac{c_{kr}\left(a_{p1} C_{SEP}^{Sp}\right)^{1/3}}{\sqrt{k/\phi}}\right]^{-4} \tag{3.24}$$

For the previous equation, it is common to consider an empirical value for maximum permeability reduction factor (Sheng, 2011) of 10.

The nonlinear system of differential equations must be solved simultaneously with Darcy´s law, definitions for relative mobility, mass fractions, saturations, and other auxiliary relations for polymer flooding.

For the initial and boundary conditions it was considered that porous media was initially saturated with oil and irreducible water at some initial salinity. At the injection boundary, water saturation is always at its maximum values. For continuous polymer injection, the polymer concentration is fixed to a specified value. For slug injection, polymer concentration is maintained to the desired value during the slug size, after which, chase water injection follows.

3.2 Numerical model for 1D polymer flooding

The system of advection-reaction equations, developed for describing the polymer flooding process, has no analytical solution for the general case, but it is suitable for numerical solution. Although, the flow model developed could work with any initial and boundary conditions, Dirichlet-type boundary conditions were considered as it was described before.

The nonlinear polymer flooding model, equations (3.8) - (3.10), could adopt the following general form:

$$\frac{\partial}{\partial t_D}\left[C_{i1}S_1 + \hat{C}_i\right] + \frac{\partial}{\partial x_D}\left[f_1 C_{i1}\right] = 0 \tag{3.25}$$

This equation was discretized by finite differences, resulting in an unconditionally stable numerical model for the flow problem, using an upwind fully implicit difference scheme and Newton-Raphson (NR) method (Ertekin et al., 2001; Chen et al., 2006). The mesh assumes that the block size is constant. The discretized nonlinear equations at node $\imath$ and time step $n+1$, takes the residual ($R\varepsilon$) form:

$$R\varepsilon_{i,\imath}^{n+1} \approx \frac{(C_{i1}S_1)_i^{n+1} - (C_{i1}S_1)_i^n}{\Delta t_D} + \frac{\hat{C}_{i,\imath}^{n+1} - \hat{C}_{i,\imath}^n}{\Delta t_D} + \frac{[(C_{i1}f_1)_\imath - (C_{i1}f_1)_{\imath-1}]^{n+1}}{\Delta x_D} \tag{3.26}$$

Either for continuous injection or slug injection schemes, the boundary conditions are Dirichlet-type, then, $\imath = 2, 3, \cdots, \mathrm{I}-1$; and for time discretization $n = 0,1,2,\cdots$.

For linearizing the system of non-linear equations is required the iteration level $v+1$ of the $n+1$ time step solution, and a generic form of the linearized equation for component i and node ι, is as follow:

$$-R\varepsilon_{i,\iota}^{v}(\xi_1,..,\xi_m,..,\xi_M) = \sum_{m=1}^{M}\left(\frac{\partial R\varepsilon_{i,\iota}}{\partial \xi_m}\right)^{v} \partial\xi_m^{v+1} \tag{3.27}$$

where m is the index for the unknown variables (ξ) around the node i, and $\partial\xi_m^{v+1}$ are the iteration changes of the unknowns:

$$\partial\xi_m^{v+1} = \xi_m^{v+1} - \xi_m^{v} \tag{3.28}$$

The generic form of the non-zero coefficients that linearized the system of equations, for component i, unknown variable ξ_m, at node i, have the following form:

$$\left(\frac{\partial R\varepsilon_{i,\iota}}{\partial \xi_m}\right)_{i-1}^{v} = \frac{1}{\Delta x_D}\left(\frac{\partial [C_{i1}f_1]}{\partial \xi_m}\right)_{i-1}^{v} \tag{3.29a}$$

$$\left(\frac{\partial R\varepsilon_{i,\iota}}{\partial \xi_m}\right)_{i}^{v} = \frac{1}{\Delta t_D}\left[\left(\frac{\partial [C_{i1}S_1]}{\partial \xi_m}\right)_{i}^{v} + \left(\frac{\partial \hat{C}_i}{\partial \xi_m}\right)_{i}^{v}\right] + \frac{1}{\Delta x_D}\left(\frac{\partial [C_{i1}f_1]}{\partial \xi_m}\right)_{i}^{v} \tag{3.29b}$$

The Jacobian matrix takes in to account all components and unknown variables for each node.

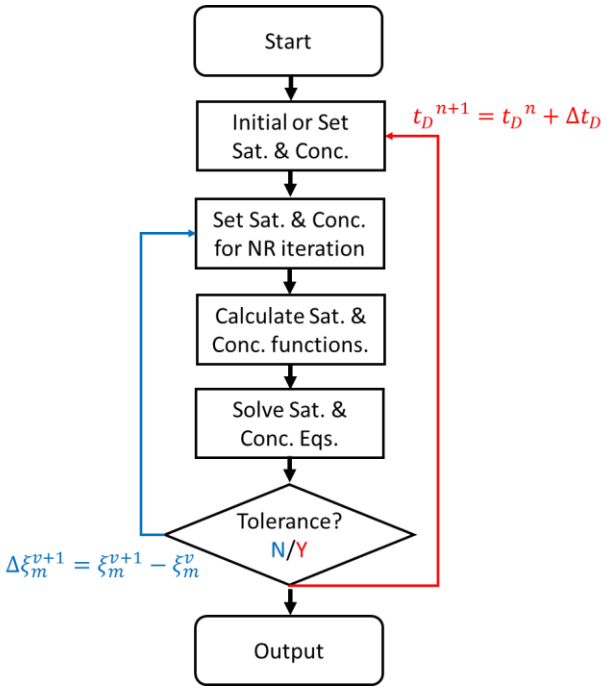

Figure 3.1: Flowchart of the numerical simulator developed.

To summarize, Figure 3.1 presents the flowchart that the numerical simulator applies for the numerical algorithm. In each time step, the simulator set values for saturation and concentrations, and begins the iterative process to solve implicitly the saturation and concentrations variables. All the newly updated variables and properties are provided for the initial values of the next time step. This continues until it reaches the final time.

The validation for the numerical algorithm by using the analytical solutions of BL (Lake, 1989; Buckley and Leverett, 1942) for waterflooding and the extension of the fractional flow theory for polymer flooding (Sorbie, 1991; Pope, 1980), as well as, by using experimental data carried out in 1D corefloods for water and polymer flooding. is presented later.

3.3 Effects of polymer and salinity concentrations on flow properties

Applying fractional flow theory concepts along with the most important phenomena and flow properties models related to polymer flooding, we present a qualitative analysis to get a quick idea of favorable scenario for oil recovery, before building a more elaborated predictive model, and so averting computing effort and time. Additionally, this analysis allows us to preliminary identify the phenomena that could be or could not be included without losing physical and chemical representation.

Based on equation (3.15), fractional flow depends on relative permeability, fluid viscosity and permeability reduction factor. Several experimental studies reported (Honarpour et al., 1986) that the effect of viscosity on relative permeabilities are very small and many times insignificant. Nevertheless, many tests conducted (Sheng, 2011) show that relative permeability curve for polymer solution is significantly lower than the corresponding relative permeability curve for water before polymer transport. This is caused by effective permeability reduction, which is a consequence of polymer adsorption. Therefore, to account for the mobility decrease due to permeability reduction, the viscosity of the aqueous phase is multiplied by the value of the permeability reduction factor as equation (3.16) illustrates.

To analyze the influence of the flow properties on each other, and on the fractional flow according to equations (3.11) – (3.24), the polymer and reservoir data described by Sorbie, (1991) are used as a starting point (see Table 3.1).

Phase viscosities	$\mu_1 = 0.5cP$	$\mu_2 = 3.0cP$
Water relative permeability	$k_{r1}^* = 0.3$	$e_1 = 2$
Oil relative permeability	$k_{r2}^* = 0.9$	$e_2 = 3$
Residual saturations	$S_{1r} = 0.25$	$S_{2r} = 0.22$
Polymer solution viscosity	$\mu_1^o = 7.8cP$	$C_{41} = 500ppm$
Polymer adsorption	$\hat{C}_4 = 3.12x10^{-3}lb/ft^3$	R_k=2
Reservoir geometry	$L = 2000ft$	$A = 2500ft^2$
Reservoir properties	$\phi = 0.25$	$k = 1000mD$
Fluid injection rate	$Q = 685ft^3/D$	

Table 3.1: Polymer and reservoir data for 1D flow problem.

3.3.1 Polymer adsorption

Langmuir-type isotherm is used to describe polymer adsorption ($\hat{C}_4$ or Cad_4), equation (3.17). Figure 3.2 illustrates a typical behavior of adsorption for the reference case (a_4 is constant and a_4/b_4 is fixed to 0.0163). As polymer concentration increases the polymer adsorption also increases until it reaches asymptotically an adsorption level of $\hat{C}_4 = 0.0163wt\%$. For the case where no salinity effect is included (reference case), and for a Langmuir isotherm, b_4 controls the curvature of the isotherm and the ration a_4/b_4 determines the plateau value for adsorption (Lake, 1989).

To capture the influence of salinity on polymer adsorption equation (3.18) is used, where a_4 is function of salinity and polymer concentration. For comparison with the reference case, it is selected a salinity of $C_{51} = 0.1wt\%$ and a set of values for α_1 and α_2 so that a_4/b_4 approaches to 0.0163. Figure 3.2 shows that at low polymer concentrations $C_{51} = 0.1wt\%$ and no salinity effect curves seem identical but, after a certain value of C_{41} the curves start to separate as it is illustrated. Additionally, this Figure also includes a case where salinity is lower ($0.01wt\%$) and it can be observed that as salinity decreases the adsorption level diminishes and tends to flatten.

Polymer adsorption is an important phenomenon that must be evaluated for a polymer flooding projects, due to loss of polymer from solution and a detrimental effect on the displacement. Hence, a proper polymer adsorption behavior should be included in modeling.

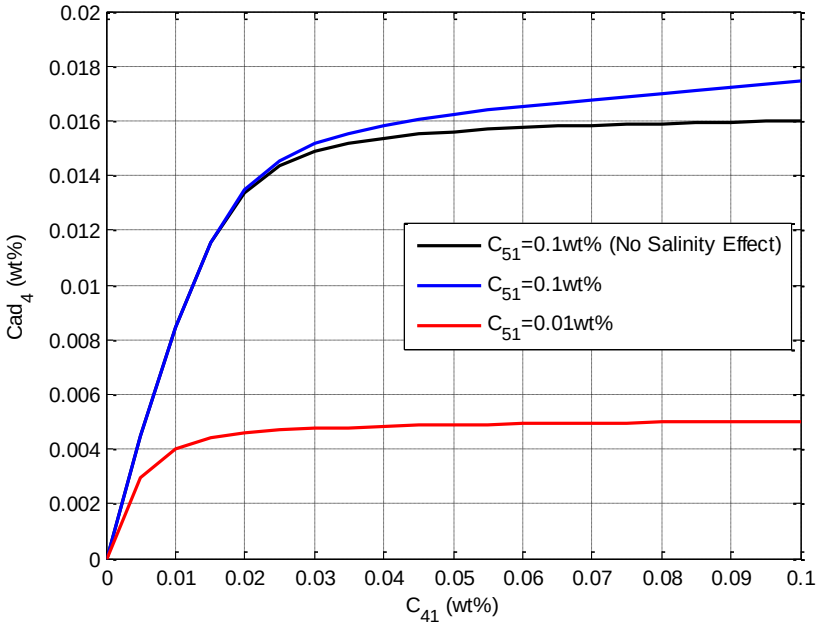

Figure 3.2: Polymer adsorption concentration for no-salinity effect and salinities $0.01wt\%$ *and* $0.1wt\%$.

3.3.2 Permeability reduction factor

When a polymer solution flows throughout a porous media some of the polymer molecules are adsorbed on the rocks surface, causing permeability reduction or pore throat blocking. Hence, the reduction of permeability is accounted for equations (3.23) and (3.24).

Equation (3.23) shows that permeability reduction factor depends on R_{kmax} and C_{41}. The behavior of maximum value for permeability reduction factor, equation (3.24), is illustrated in Figure 3.3, and it implies that as effective salinity (C_{SEP}) increases, R_{kmax} initially decays rapidly, and then it is asymptotic. S_p is a power parameter that also contributes to salinity effect, as Figure 3.3 also depicts; when S_p increases the maximum value of permeability reduction factor decreases.

From equation (3.23) and a fixed value of R_{kmax}, the relationship between permeability reduction factor and polymer solution concentration is similar to the relationship between polymer adsorption and polymer solution concentration with no salinity effect considered. For $1 \leq R_k \leq R_{kmax}$, and b_{kr} controls the curvature of the permeability reduction.

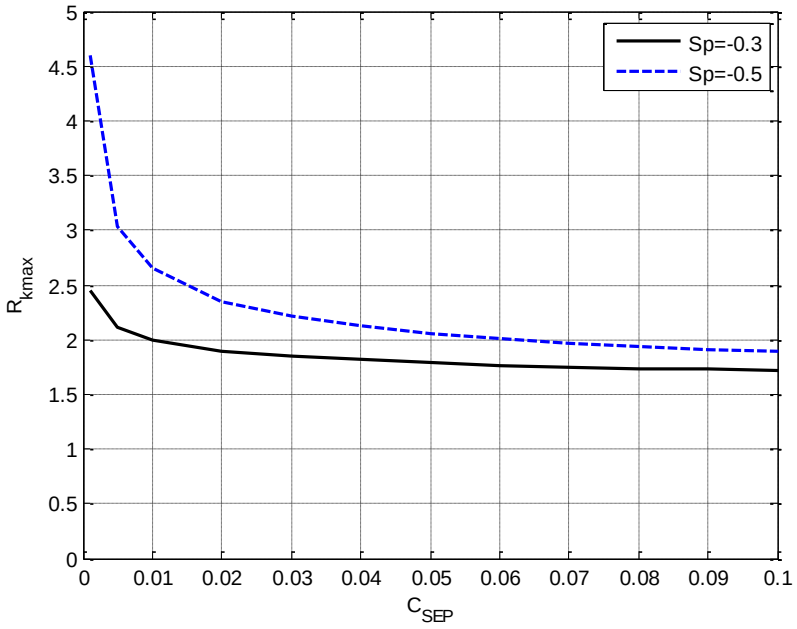

Figure 3.3: Maximum value for permeability reduction factor versus effective salinity.

It is important to notice that the effect of increasing salinity on permeability reduction factor is different from that observed on polymer adsorption. This means that permeability reduction from equations (3.23) and (3.24) does not correlates with the increase of polymer adsorption. Nevertheless, the prediction of R_{kmax} agrees with the reported in the literature by Sheng (2011) and Martin et al. (1983).

3.3.3 Viscosity at zero shear rate

Equation (3.20) describes the polymer solution viscosity at zero shear rate (μ_1^o) as a function of effective salinity and polymer concentration. Figure 3.4 depicts the behavior of μ_1^o for four specific salinity effects (C_{SEP}^{Sp}), where polymer concentration raises the viscosity at zero shear rate, and it increases with a cubic relationship. In this figure as the combination of C_{SEP} and S_p increases, the polymer viscosity at zero shear rate decreases. Higher salinities decrease the benefits of polymer solution viscosity.

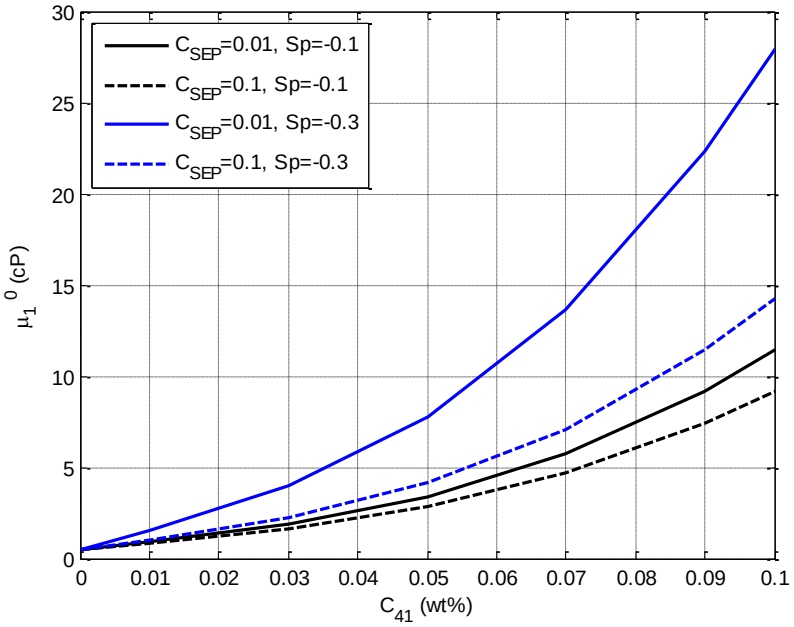

Figure 3.4: Viscosity at zero shear rate versus polymer concentration.

3.3.4 Equivalent shear rate

To estimate the effects of shear rate on fractional flow behavior, equation (3.22) is used by considering water flow rate, permeability reduction factor and other multiphase flow properties. Assuming viscosity at zero shear rate (equation 3.20) as an initial approximation to calculate the water fractional flow (equation 3.15) and then the equivalent shear rate.

Three cases for water fractional flow and equivalent shear rate were computed and illustrated in Figure 3.5, as function of water saturation. For cases where $R_k = 1$; as μ_1^o increases, the water saturation behind de front increases and $\dot{\gamma}_{eq}$ decreases. For cases where $\mu_1^o = 7.8cP$; as R_k increments the water saturation behind de front increases and $\dot{\gamma}_{eq}$ reaches higher values. The cases in this figure shows that fractional flow curve is more effected by variations in permeability reduction than by variations in viscosity at zero shear rate, so this is something to consider in cases where permeability reduction has an important role.

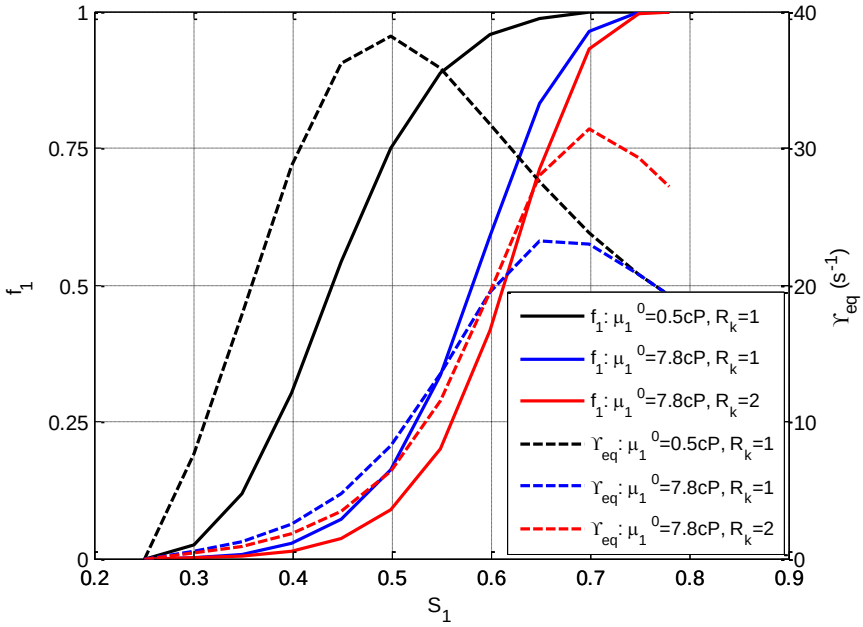

Figure 3.5: Water fractional flow and equivalent shear rate versus water saturation.

3.3.5 Aqueous phase viscosity

To estimate the apparent polymer solution viscosity (μ_{1app}) equation (3.21) is used. Figure 3.6 displays two cases with $\alpha = 2$ as a typical value (Sheng, 2011), $n_C = 0.45$, $1/\lambda = 40s^{-1}$, and varying total fluid velocity. When velocity is lower, $\dot{\gamma}_{eq} < 40s^{-1}$, μ_{1app} presents slight variations. On the other hand, as total fluid velocity increases and provides $\dot{\gamma}_{eq} > 40s^{-1}$ (power law region), apparent polymer viscosity decreases considerably (this decrease in apparent viscosity could be different for viscoelastic fluids, as the onset of dilatancy and dilatant behavior dictate the increment of viscosity). Depending on the combination of total fluid velocity and λ, it is the importance to consider the impacts of equivalent shear rate in modeling.

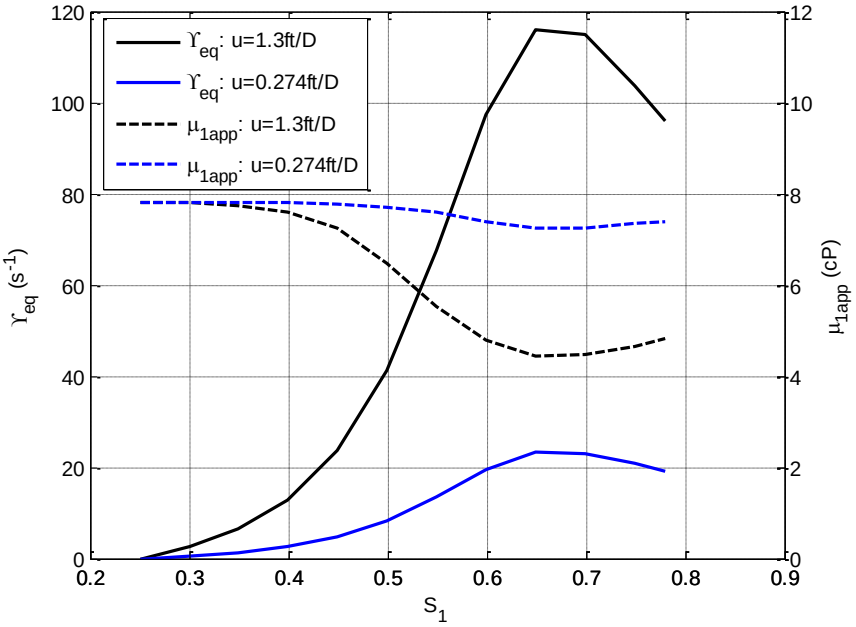

Figure 3.6: Shear rate and apparent polymer viscosity versus water saturation.

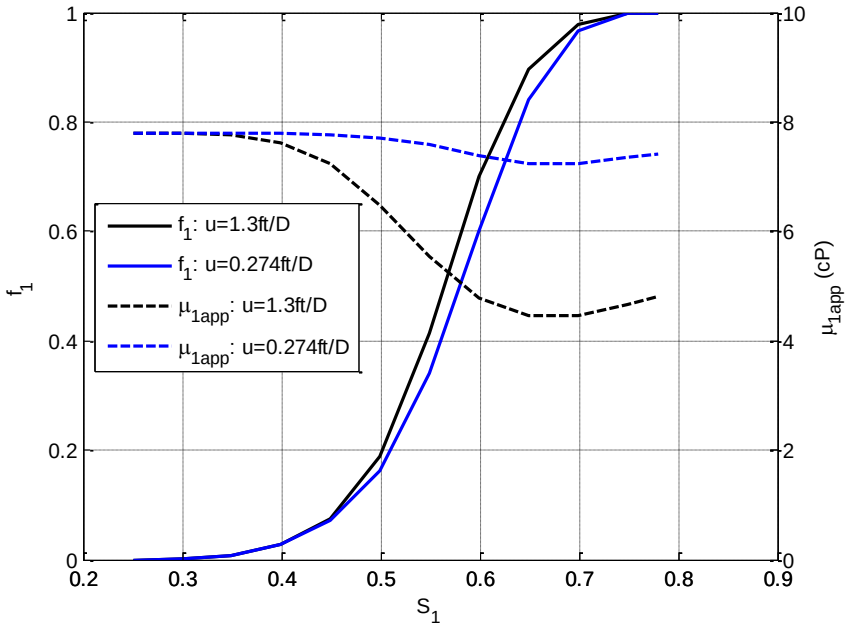

Figure 3.7: Water fractional flow and apparent polymer viscosity versus water saturation.

3.3.6 Aqueous phase fractional flow

Analyzing the cases in previous figures, focusing on the relation between fractional flow and apparent viscosity. Figure 3.7 depicts that as total fluid velocity increase, apparent polymer viscosity is reduced by shear rate effects, and it reduces the water saturation behind the front, and so it provides a lower oil recovery performance.

For the case of viscoelastic fluids, as shear rate increases the decrement of apparent viscosity and the start of the shear thickening behavior will depend on the onset of dilatancy and dilatant behavior. In this rheological regime, the increment of apparent viscosity leads to increase water saturation behind the displacement front and so to get a better oil recovery.

Chapter 4: Validation of the 1D model and flow dynamic

4.1 Numerical solution validation

4.1.1 Comparison of numerical model and analytical solution

The validation of the model versus the analytical solution to the fractional flow of Buckley-Leverett (Lake, 1989; Buckley and Leverett, 1942) and its extension for polymer flooding (Lake, 1989; Pope, 1980) was done using the case described by Sorbie (1991).

Figure 4.1 and Figure 4.2 compare the analytical and numerical solutions of the aqueous phase saturation profile for water flooding and polymer flooding, respectively. The saturation profiles obtained numerically give a good approximation to the analytical solutions. As the mesh is refined, the numerical approximation improves.

To analyze the performance of the numerical approach, ϵ_A is used to estimate the saturation profiles error of the numerical solution versus the analytical solutions. This represents the area bordered by analytical and numerical results (Rosado et al., 2007), and it is derived by using the trapezoidal rule.

$$\epsilon_A = \frac{\Delta x_D}{2}\left\{\left|S^n_{1,i=1} - S_1(x_{Di=1}, t^n_D)\right| + \left|S^n_{1,i=I} - S_1(x_{Di=I}, t^n_D)\right| + 2\sum_{i=2}^{I-1}\left|S^n_{1,i} - S_1(x_{Di}, t^n_D)\right|\right\} \tag{4.1}$$

Figure 4.3 and Figure 4.4 illustrate the error (ϵ_A) sensitivity to number of nodes for a saturation profile at a specific time, for water flooding and polymer flooding, respectively. These figures show a similar behavior for the numerical performance; ϵ_A tends to decrease when increasing the number of nodes or the number of time steps. Then, the computational effort is worthless form time steps above 400. Form these cases, 200 nodes and 200 time steps yield acceptable results.

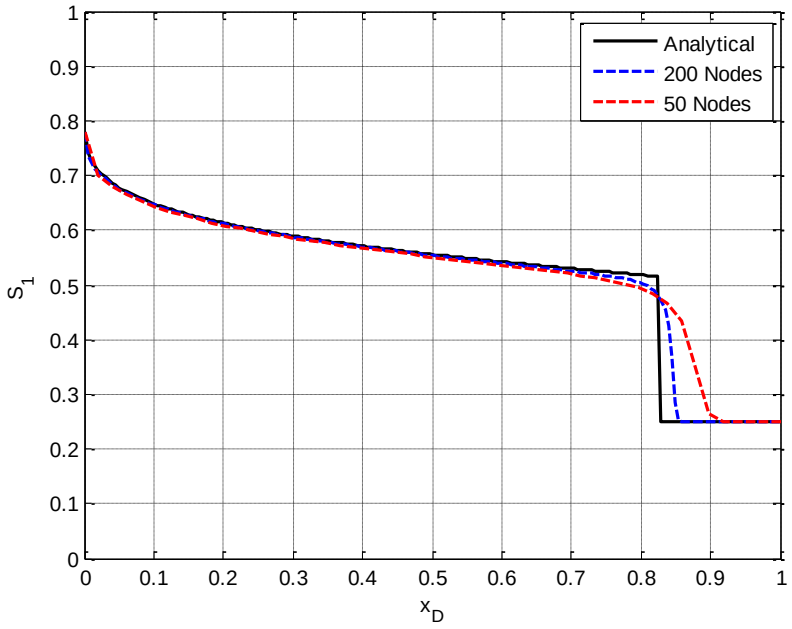

Figure 4.1: Comparative of numerical and analytical solutions for waterflooding.

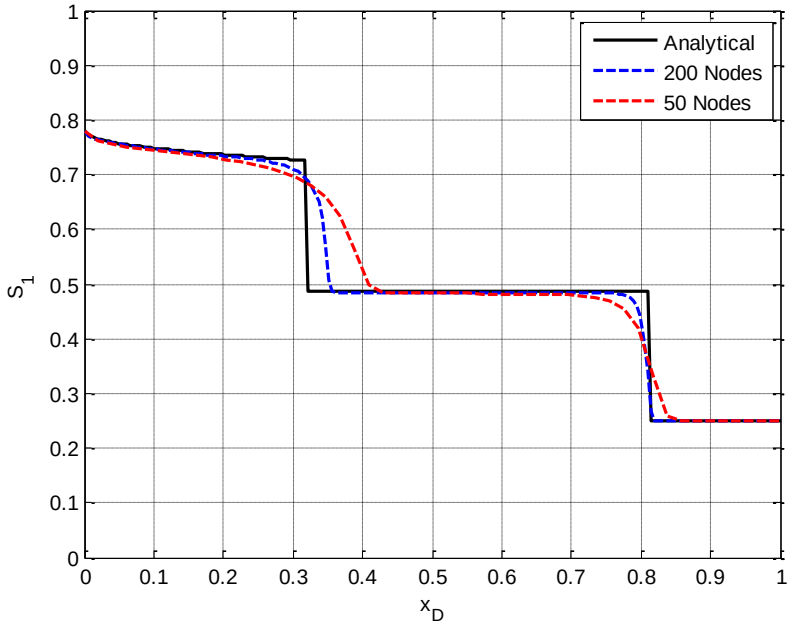

Figure 4.2: Comparative of numerical and analytical solutions for polymer flooding.

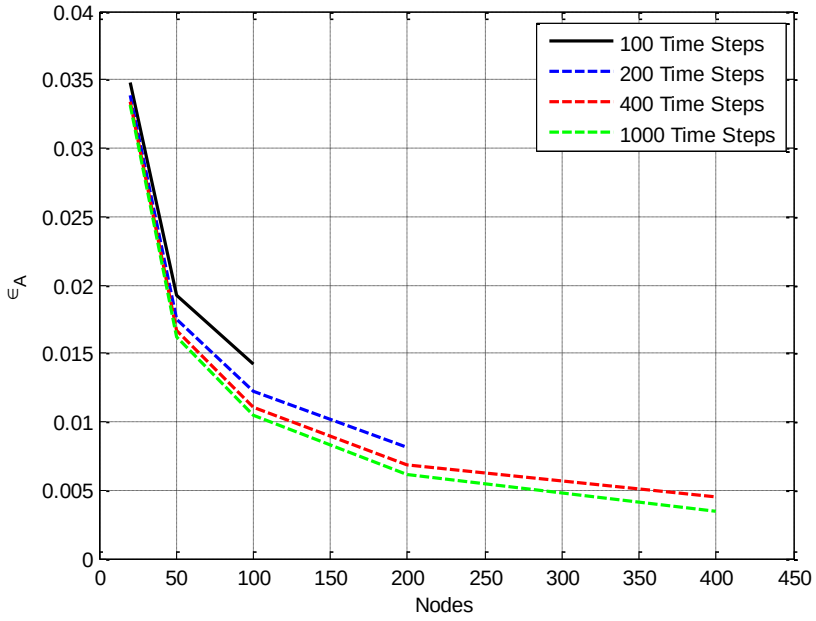

Figure 4.3: Behavior of ϵ_A as a function of number of nodes in the grid for waterflooding.

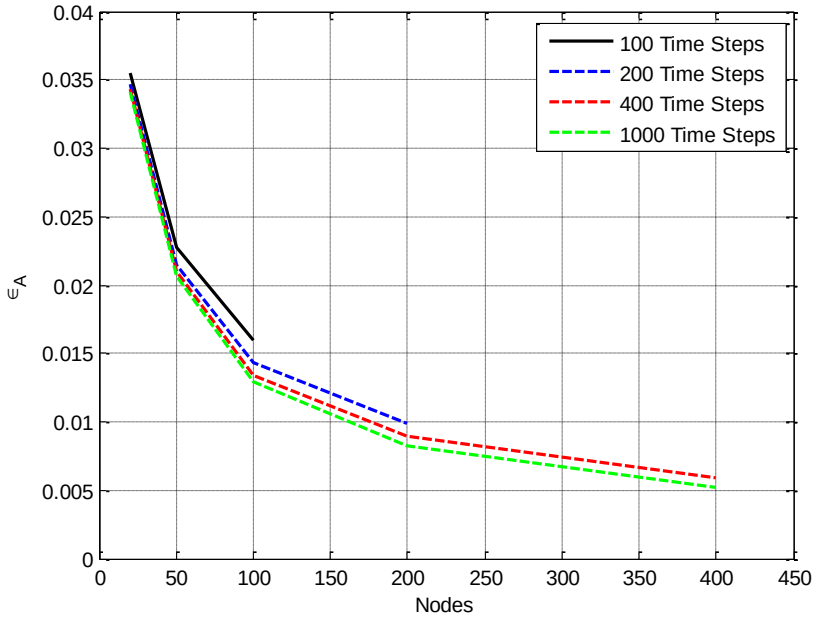

Figure 4.4: Behavior of ϵ_A as a function of number of nodes in the grid for polymer flooding.

Although, applying the analytical approach from the extension of fractional flow theory to polymer flooding is very useful to provides practical results, it has limitations in cases where salinity variations, shear rate effects on polymer rheology and permeability reduction are important for estimating fluid distribution and petroleum recovery. The modeling presented in this work, applies to a wide range of flow cases, and provides a more realistic physical representation of the polymeric solution flow performance by describing phases and composition distribution along porous media, as well as oil recovery behavior.

4.1.2 Comparison of numerical model and core flood experiments

The numerical model developed in this work, as well as CMG-STARS software, were used to reproduce experimental data reported by Koh et al. (2018) and Masuda et al. (1992), of water and polymer flooding in sandpacks and reservoir cores.

From Koh, the first five experiments (1 to 5) of waterflooding (WF) and polymer flooding (PF) were used to evaluate our proposed numerical model, since data of relative permeability curves, rheological and adsorption behavior dependence of salinity and polymer concentrations, were available. We fitted the equations (3.13) to (3.24) of our model to experimental data to find the parameter required by the new numerical model.

Experiment	#1	#2	#3	#4	#5
Oil viscosity, cP	80	120	250	1050	72
Oil-Water viscosity ratio	167	250	521	1591	144
Porosity	0.35	0.36	0.37	0.39	0.28
Water velocity, ft/D	13	14	14	5	3.3
Polymer concentration, ppm	1200	1300	2450	3500	2000
Equivalent shear rate, 1/s	10.1	10.7	9.8	8	54
Polymer viscosity, cP	16	28	108	46	12
Initial oil saturation	0.87	0.88	0.88	0.89	0.68
Initial water saturation	0.12	0.12	0.12	0.11	0.32

Table 4.1: Brief description of coreflood properties for laboratory polymer solution flooding.

As a brief reference, Table 4.1 indicates some properties used for experimental core floods, where the properties of polymer solution are indicated to get the desired apparent viscosity.

For the five experiments, the rheological model represents Newtonian and shear thinning behavior, then water velocities in Table 4.1 are in the power law region.

For experiments 1 through 3, the same brine was used, and the authors determined by a tracer test that the sands were homogeneous. The oil viscosities under reservoir conditions were $80cP$, $120cP$ and $250cP$, while polymer viscosities were $16cP$, $28cP$ and $108cP$, respectively. These polymer viscosities correspond to the shear rates specified in Table 4.1 for each experiment. In the publication, the polymer solution viscosity for each experiment was chosen to give an endpoint mobility ratio close to 1.

We start with experiment #3 since it was the most discussed in the publication. Figure 4.5 illustrates the recovery efficiency against PV injected of the experimental and simulated data of water and polymer flooding. Simulated data were obtained with the new model and the CMG-STARS software. From the Figure it is observed that numerical results yield a good approximation to experimental data.

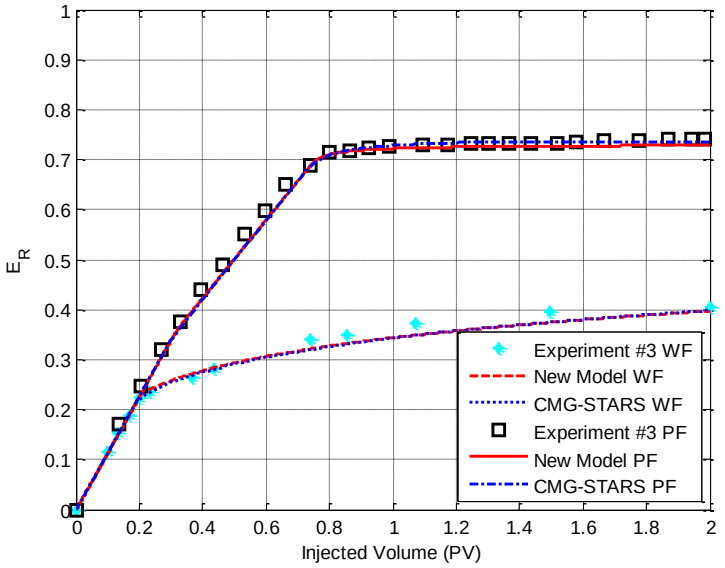

Figure 4.5: Comparison of experimental and simulated data of polymer flooding test 1. Simulated data were obtained with the proposed model and CMG-STARS software.

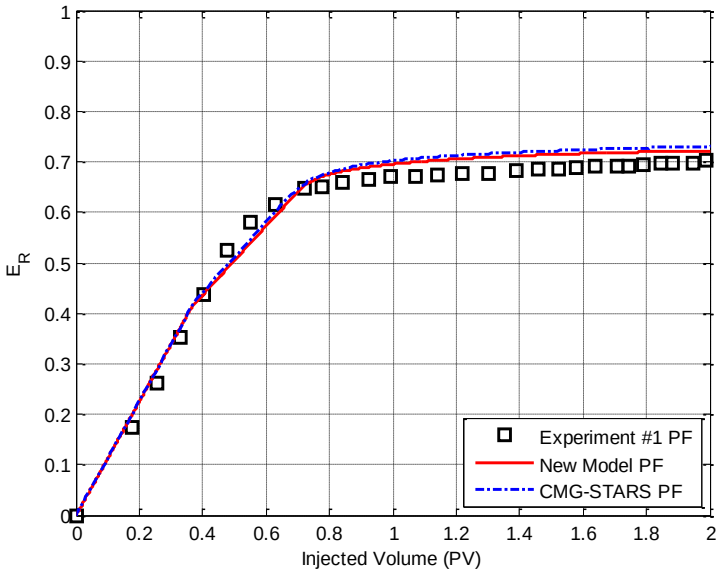

Figure 4.6: Comparison of experimental and simulated data of polymer flooding test 1. Simulated data were obtained with the proposed model and CMG-STARS software.

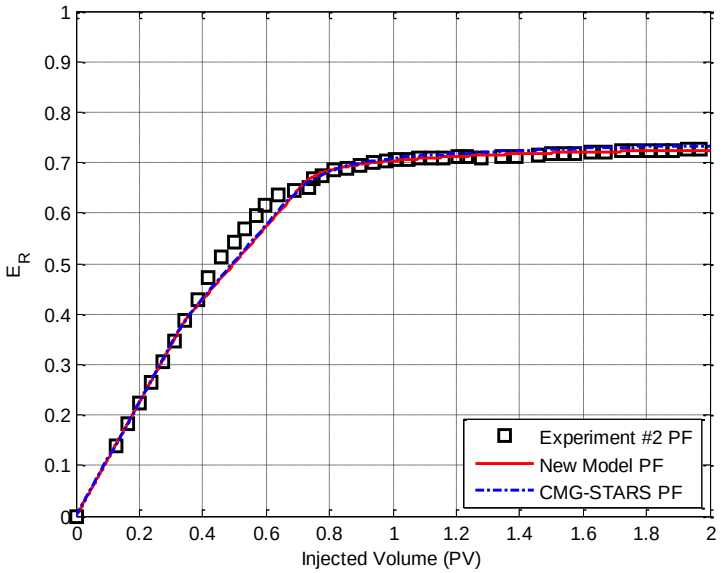

Figure 4.7: Comparison of experimental and simulated data of polymer flooding test 2. Simulated data were obtained with the proposed model and CMG-STARS software.

Experiments #1 and #2, describe flow cases with oil/water viscosities of 167 and 250, flooded with polymer concentration of $0.12wt\%$ and $0.13wt\%$, respectively. Figure 4.6 and

Figure 4.7, shows the recovery efficiency against injected PV for polymer flooding experimental data, and the simulated with the new model and the CMG-STARS software. From the Figures we can observe that, although the numerical representation in both flow cases provides good approximation to experimental data, the numerical results in the case of Figure 4.7 are more accurate to experimental data after $0.8PV$ of flooding than in Figure 4.6. Additionally, it is noticed that simulated data (New model and CMG-STARS) behave a bit differently from experimental data, in the transition from water breakthrough to polymer breakthrough (from $0.4PV$ to $0.8PV$), this behavior is not observed in the results for experiment #3 (Figure 4.5).

For experiments #4 and #5 the injection strategy is different; both started with a waterflooding followed by polymer flooding. In experiment # 4 the oil and polymer viscosities were $1{,}050cP$ and $46cP$, respectively, with an end point mobility ratio of 10. Figure 4.8 displays the WF + PF behavior, and it is observed that numerical results have good approximation to experimental data even though in polymer flooding stage numerical results behave a bit differently from experimental data near $2.5PV$ of injected time. This behavior is not observed in the results for experiment #5 (Figure 4.9).

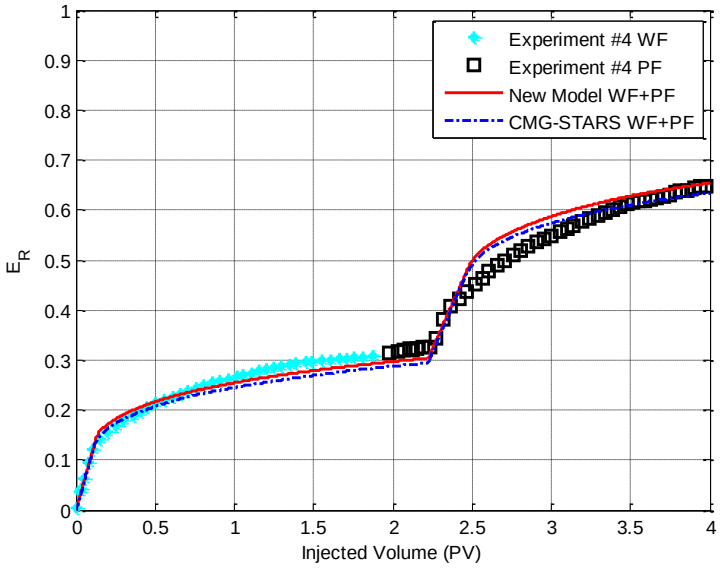

Figure 4.8: Comparison of experimental and simulated data of water and polymer flooding test 4. Simulated data were obtained with the proposed model and CMG-STARS software.

Experiment # 5 considers a polymer injection (polymer viscosity of $12cP$) after a stage of waterflooding to displace an oil with a viscosity of $72cP$. In this experiment the end point mobility ratio was set to 1. The results are shown in Figure 4.9, where it is illustrated the recovery efficiency against injected PV for the experimental data and simulated data during water and polymer flooding. It is observed a good match between experimental and numerical data.

By using the properties and parameters extracted from the publication of (Koh et al., 2018), from Figure 4.5 to Figure 4.9, we can identify that the numerical results provide a good approximation to experimental data for experiments #1 to 5#. In some experiments for polymer flooding, there was detected a slight difference between numerical and experimental results, in the transition period from water breakthrough time to polymer breakthrough time, this difference could be reduced by adjusting polymer retardation factor for these experiments. Additionally, for all experiments the performance of the new numerical model developed in this research and the results from CMG-STARS models are in close agreement. Therefore, despite the assumptions of the new model, the implemented numerical algorithm provides a good representation.

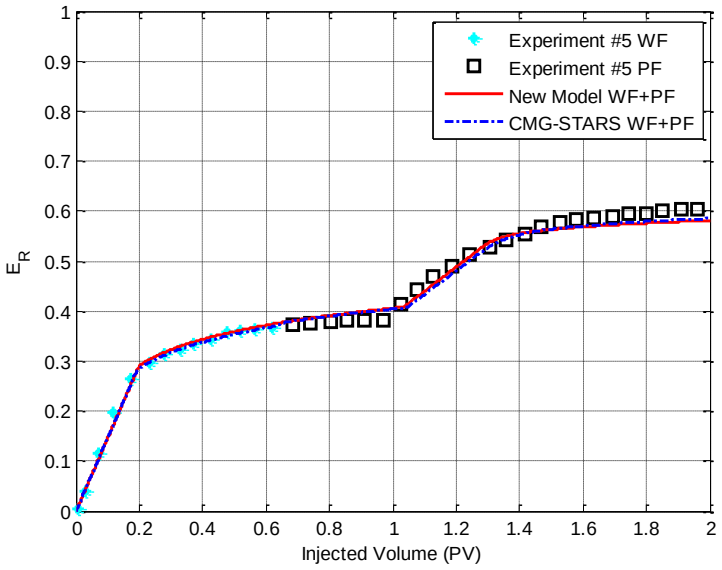

Figure 4.9: Comparison of experimental and simulated data of water and polymer flooding test 5. Simulated data were obtained with the proposed model and CMG-STARS software.

An additional set of experimental data used in the validation was the reported by Masuda, in which a polymer injection process was carried out to displace a mineral oil with a viscosity of $25cP$. To reproduce this experiment, we used the specified core properties (relative permeability curves, rheological behavior, and fractional flow curves) to fit equations (3.13) to (3.16), (3.20), and (3.21) to find the parameters and properties required by the new numerical model. For oil relative permeability, we noticed that Corey type behavior was not the best fit (this could yield some inaccuracies to reproduce the efficiency recovery obtained from the publication of Masuda), while water relative permeability was very good fitted with Corey behavior.

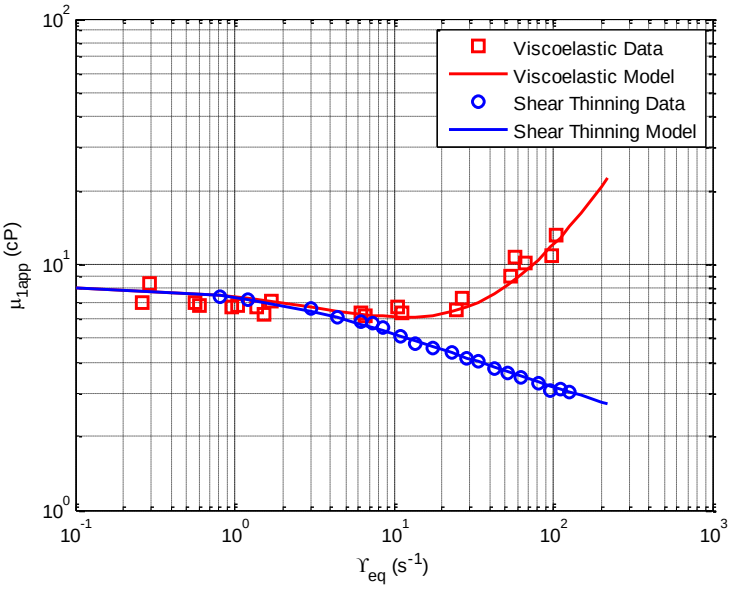

Figure 4.10: Shear thinning and viscoelastic models fit to experimental data taken from Masuda.

The rheological behavior of polymer solution for shear thinning and viscoelastic behavior was obtained from the experimental data of Masuda et al. (1992), which are depicted in Figure 4.10, together with the fitting of the models for shear thinning (equation 3.21a), shear thickening (equation 3.21b) and viscoelastic (equation 3.21c) behaviors.

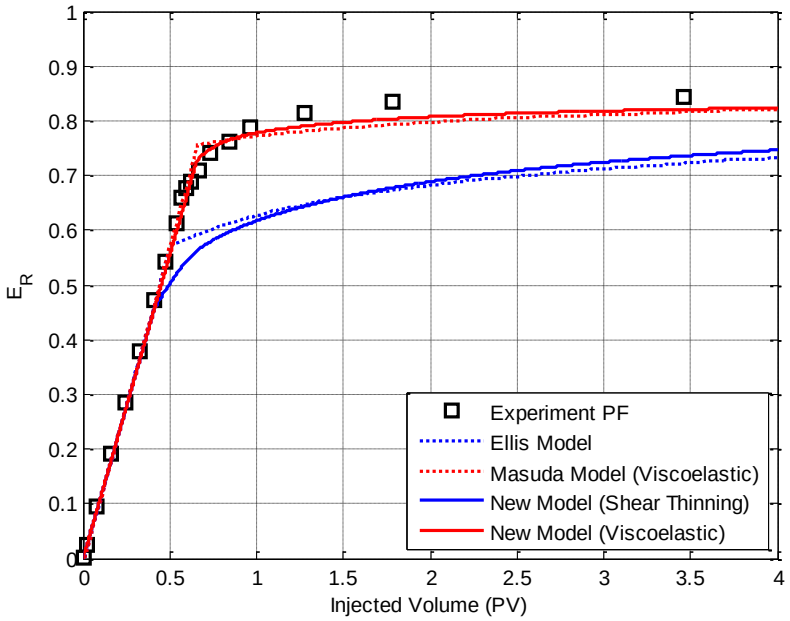

Figure 4.11: Comparison of experimental and simulated data of polymer flooding with data from Masuda et al. Simulated data were obtained with the proposed model for shear thinning and viscoelastic behavior.

Beginning with the shear thinning rheological behavior, we reproduce the Ellis model results taken from Masuda and presented in Figure 4.11; it is observed that results of the New Model for shear thinning displays good approximation to Ellis model solution even though near the polymer breakthrough time, numerical results are different, this could be explained from the Masuda publication, where it is identified that the flow model was built for an aqueous phase with a polymer that is mixed with a mobile water instantaneously at the displacement front, but its concentration is kept constant, therefore the aqueous phase behaves as only one component phase. On the other hand, the new model proposed in this research considers more than one component in the aqueous obey phase.

Whit the same data set of New Model (shear thinning) but changing the rheological model to viscoelastic (Figure 4.10), we obtained the New Model (Viscoelastic) results to reproduce the experimental data of Masuda. From Figure 4.11, it is identified a close agreement between experimental data and New Model (Viscoelastic) results, then the experiment from Masuda is represented in the shear thickening or dilatant behavior regime. Additionally, the new model presents better results than the results of Masuda Model (Viscoelastic).

We conclude from this section that, although a commercial numerical simulator can be accommodated to represent simple models, and considering the simplifications of the mathematical model built in this work, we identify that CMG-STARS model needed more information such as black oil properties for different pressures and temperatures, molecular weight for each component, mass density, thermal expansion coefficient, reference depth and pressure, well geometry parameters, and temperature of injected fluid, among other information. The model developed provides a practical tool that allows us to represent crucial phenomena involved to polymer flooding in CEOR implementations at laboratory scale, with less effort.

4.2 Flow dynamic analysis

Once the validation process has been applied, in this section we illustrate the performance and the detailed flow dynamic description that the numerical model is able to hand in. This, during a theoretical investigation of the effects that key phenomena considered have on the main flow properties and oil recovery.

By using the numerical tool developed, the behavior of flow properties is obtained and, Figure 4.12 displays the aqueous saturation (S_1) and polymer concentration (C_{41}) distributions, the viscosity at zero shear rate (μ_1^o) and the apparent viscosity (μ_{1app}) for $0.5PV$ injected. This figure shows that the displacement begins with the formation of a water front followed by a polymer rich front, this last one is due to chemical retention as normalize polymer concentration front illustrates. Additionally, it is observed the difference between viscosity at zero shear rate and apparent viscosity of the polymer solution, which is a consequence of shear rate effects and degradation of polymer solution.

Although, in this example salinity concentrations remains constant during the entire injection process, the simulation tool can describe the changes in salinity concentrations along the porous media and during the evolution of the petroleum displacement by polymer flooding, as it will be discussed later.

To understand better flow dynamics and main controlling aspects of polymer flooding, we applied the numerical tool developed and investigated the effects of flow properties and injection strategy on phase saturation, chemical composition distribution and oil recovery. This increases the chances to achieve an optimum design that balances material requirements and petroleum recovery benefits.

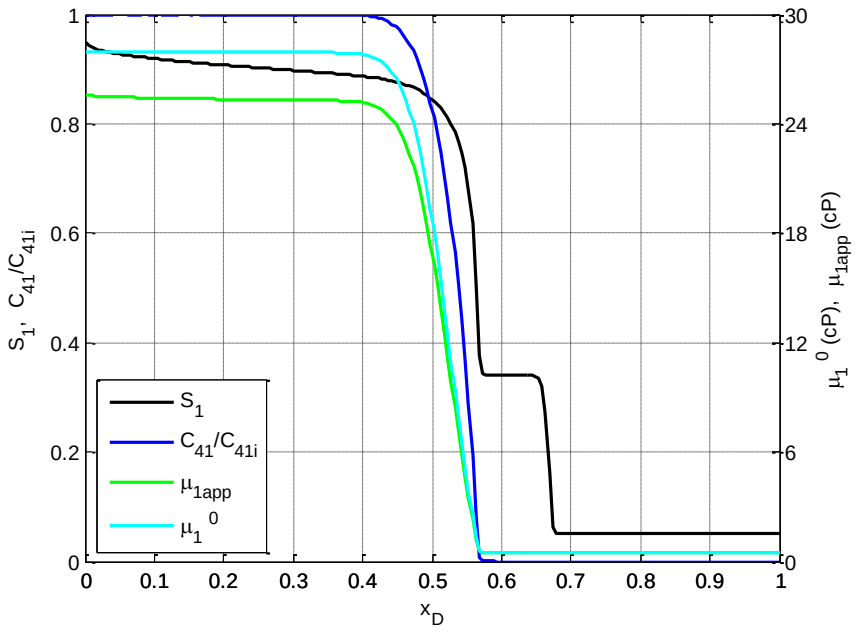

Figure 4.12 Saturation, chemical concentrations and viscosities versus distance, at $0.5PV$ injected.

4.2.1 Effect of shear rate and polymer concentration

As it was mentioned in Figure 4.12, equation (3.21) and equation (3.22), flow rate and shear rate impact apparent viscosity of the polymeric solution. Getting into more details in the effects of shear rate on polymer flooding, Figure 4.13 shows the relationship between injection flow rate and recovery efficiency (E_R) for several polymer injection concentrations. Then, at high polymer concentrations, as injection flow rate increases, the E_R decreases according to the curve for $C_{41} = 0.1wt\%$ and, as polymer concentration decreases, the influence of injection flow rate diminishes, up to the point of having no influence at all, as curve for $C_{41} = 0.001wt\%$ exhibits.

Figure 4.13 also shows that, for high C_{41} curves, as injection flow rate increases curves tend to converge to a value of recovery efficiency. At lower values of C_{41} and for high flow rates, the minimum asymptotic value of recovery efficiency decreases up to certain value where changes in flow rate no matter at all.

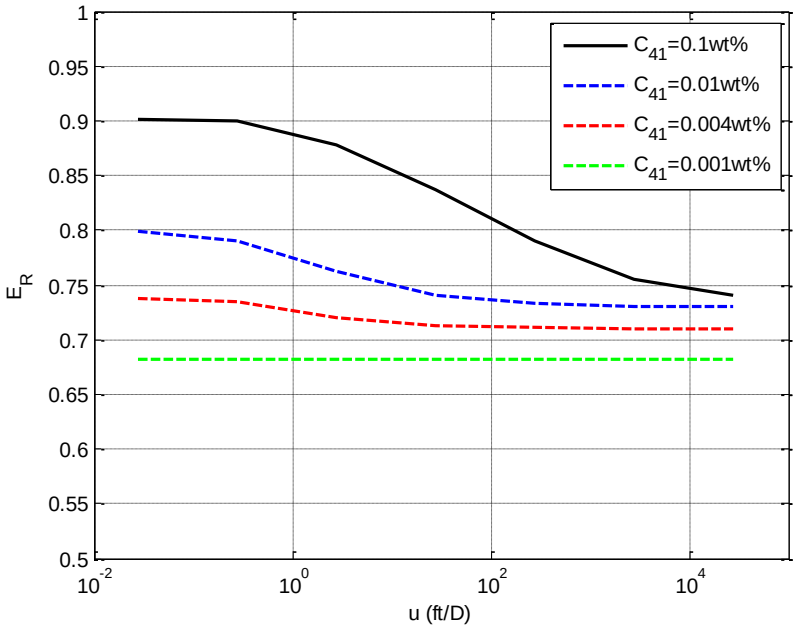

Figure 4.13: Efficiency recovery for different polymer concentrations versus injection flow rates.

To present the effect of shear rate on flow properties, it is taken the curve of $C_{41} = 0.1wt\%$ in Figure 4.13, and we compared two cases for flow rates $0.274ft/D$ and $27.4ft/D$, where E_R drops from 90% to 83%. Then, Figure 4.14 illustrates the difference in phase saturation and viscosity distributions along the porous media, and it is identified that, for a slower displacement, the water front saturation tends to decrease while the polymer front saturation increases. In this way, fluids are distributed more favorable with a longer breakthrough time. With respect to aqueous viscosity, for a slower displacement the differences between the viscosity at zero shear rate and apparent viscosity are less than for a faster displacement.

From Figure 4.13, where it is shown the influence of changing polymer concentration upon recovery efficiency. We took the cases with a fixed value of injection rate ($0.274ft/D$) and three values of polymer content ($C_{41} = 0.1, 0.01,$ and $0.0wt\%$), then Figure 4.15 exhibits the effects of polymer concentration variations on phase saturation and aqueous viscosity distributions, and it is observed that as the amount of polymer increases, the apparent viscosity of the aqueous phase increases, and as a consequence, the water front saturation decreases whereas polymer front saturation increases. This, results in a more efficient

displacement, nevertheless for practical applications it must be considered economical aspects to optimize the quantity of polymer to be used.

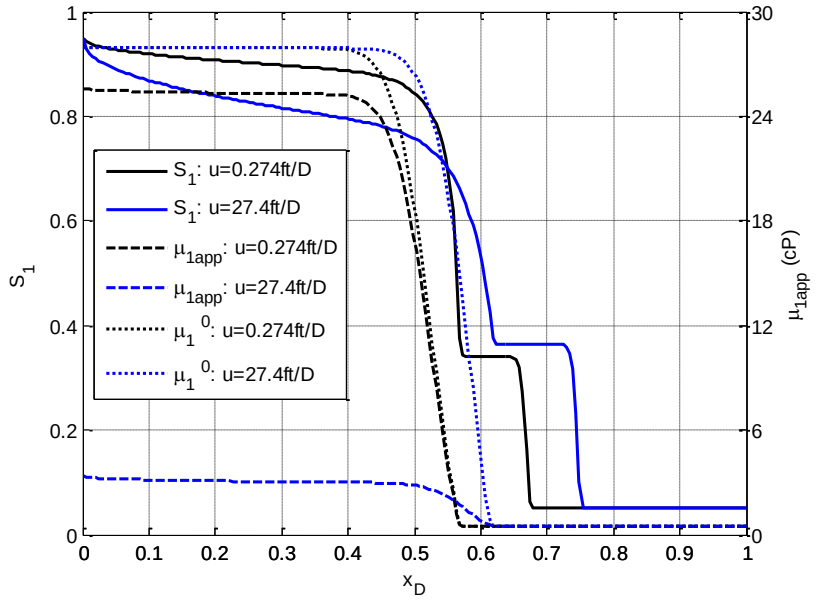

Figure 4.14: Profiles for saturation and viscosity distribution, for different injection flow rates.

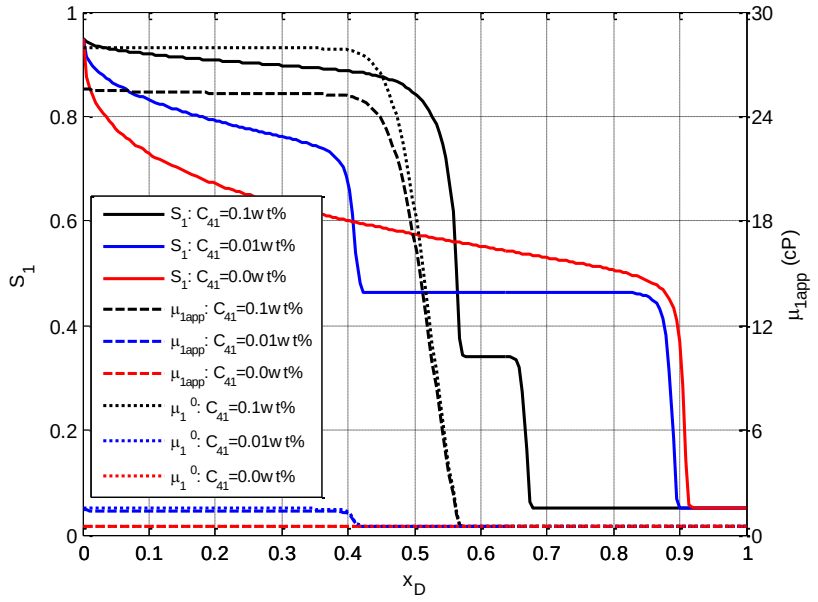

Figure 4.15: Profiles for saturation and viscosity distribution, for different polymer concentrations.

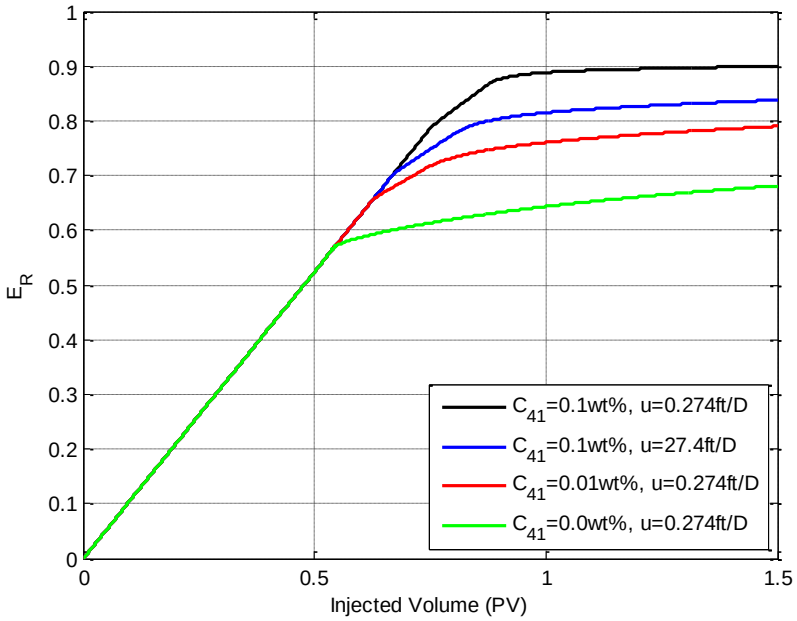

Figure 4.16: Recovery efficiency versus pore volume injected for different polymer concentrations and injection flow rates.

Pore volume injected and recovery efficiency relationship could work in a complementary way to visualize the cases in Figure 4.15. Therefore, Figure 4.16 illustrates that for a fixed injection rate ($0.274 ft/D$) and the highest polymer concentration ($C_{41} = 0.1 wt\%$), the recovery efficiency is nearby 0.8 when the aqueous front reaches the outlet, for the same pore volume injection time, the recovery efficiency for the intermediate polymer concentration ($C_{41} = 0.01 wt\%$) case is about 0.7 and, respectively close to 0.6 for water injection case. This clearly shows in a quantitative way the benefits of injecting the largest amount of polymer at the lowest possible injection rate to obtain the highest petroleum recovery.

4.2.2 Effect of salinity concentration

Salinity concentration has an important effect on apparent viscosity and so petroleum recovery during chemical flooding. Equations (3.20) and (3.21) relates salinity concentration to apparent viscosity.

Figure 4.17 displays the relationship between salinity concentration and petroleum recovery efficiency for four polymer injection concentration scenarios. In general, for a polymer

concentration case, when the salinity concentration increases the recovery efficiency decreases up to a minimum asymptotic value. It can also be observed that, when polymer concentration decreases to the minimum value ($C_{41} = 0.001wt\%$), the recovery efficiency does not depend on salinity concentration. Additionally, the figure displays that no matter polymer concentration level, as salinity increases, E_R converge to the value of the flow case with minimum polymer content.

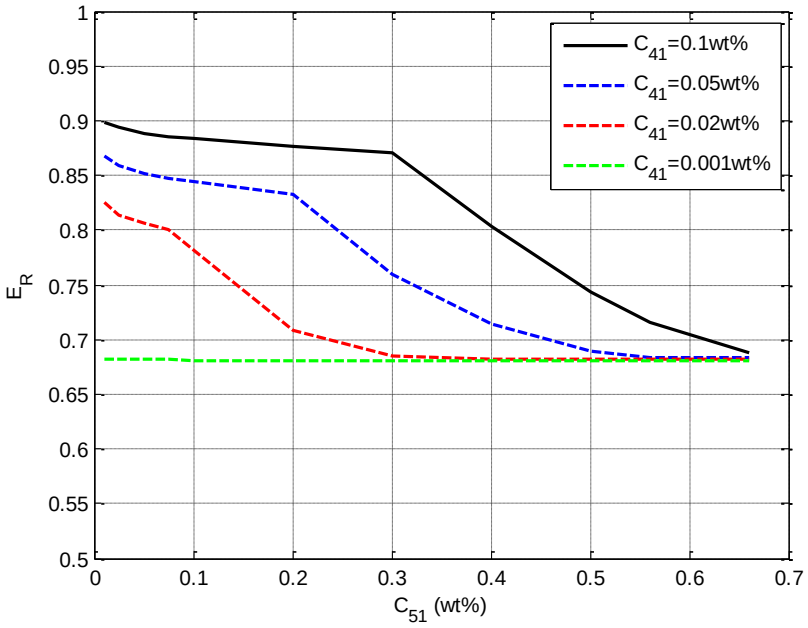

Figure 4.17: Recovery efficiency versus salinity concentration, for different polymer concentrations.

A chart with polymer volume injected and recovery efficiency contributes to describe the salinity and polymer concentration effect on petroleum recovery. Figure 4.18 takes four cases included in Figure 4.17, and it can be identified that for the case of the highest polymer concentration ($C_{41} = 0.05wt\%$) and the lowest salinity ($C_{51} = 0.01wt\%$), the water front arrives later while the polymer rich front arrives earlier to the production well than the other cases. Additionally, from the two cases with almost the same recovery efficiency at $1.5PV$ injected, it is observed that after breakthrough and before $1.5PV$, the case with $C_{41} = 0.02wt\%$ and $C_{51} = 0.01wt\%$ has better recovery efficiency than the case with $C_{41} = 0.05wt\%$ and $C_{51} = 0.2wt\%$; thus, at a specific time, there could be a value of recovery

efficiency that can be obtained with different combinations of salinity and polymer concentrations.

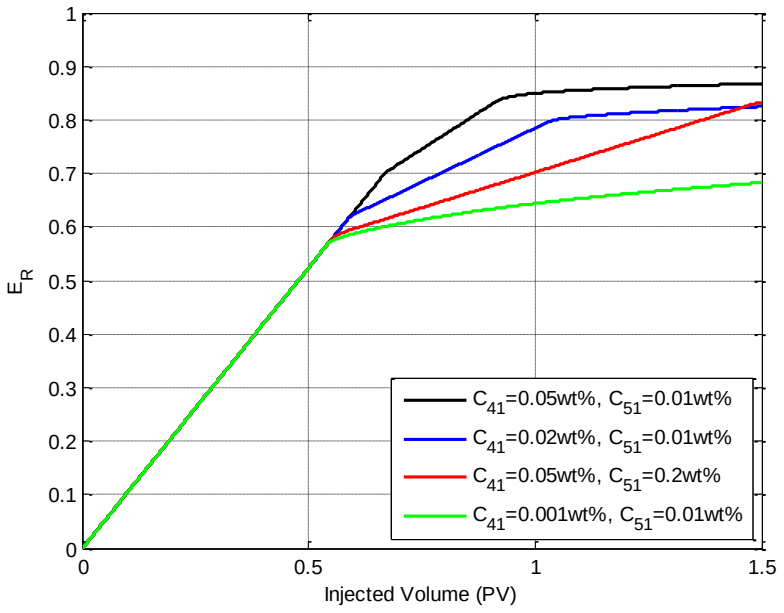

Figure 4.18: Recovery efficiency versus pore volume injected for different polymer and salinity concentrations.

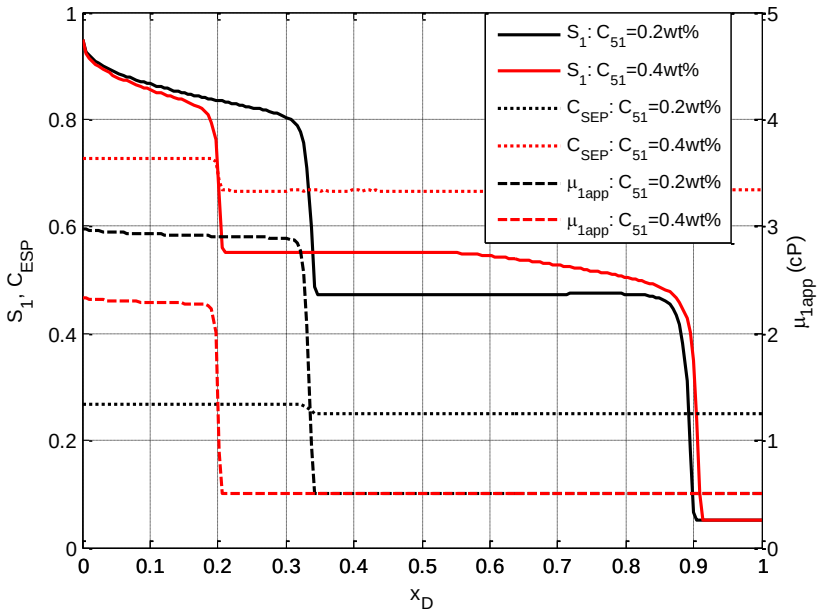

Figure 4.19: Profiles for saturation, effective salinity concentrations and apparent viscosity.

Analyzing the effects of salinity and polymer concentration on the distribution of saturation, effective salinity concentration and apparent viscosity, Figure 4.19 takes two cases ($C_{51} = 0.2wt\%$ and $C_{51} = 0.4wt\%$) included in the curve for $C_{41} = 0.05wt\%$ from Figure 4.17, and illustrates a snapshot for 0.5 pore volume injected time. From Figure 4.19, it is shown that as salinity increases the apparent viscosity of the polymeric solution deceases. Additionally, taking into account that adsorption increments with salinity (see Figure 3.2) and is a retardation term in the flow equation (Sheng, 2011; Herrera and Pinder, 2012), it is identified that the combined effect (polymer viscosity and adsorption) tend to anticipate the water shock front and delay the polymer rich shock front, so the benefits of the polymer injection arrive later. Depending on the salinity degree, this could affect the economics of the recovery process.

Figure 4.19 also allows to examine the relationship between salinity concentration and effective salinity. Considering any case from the figure and keeping in mind that the salinity concentration is constant along the porous media and during the flooding, effective salinity concentration responds to the polymer solution shock front location due to polymer concentration increments from zero to the injection concentration. The magnitude of the abrupt change in the effective salinity depends on the degree of salinity concentration.

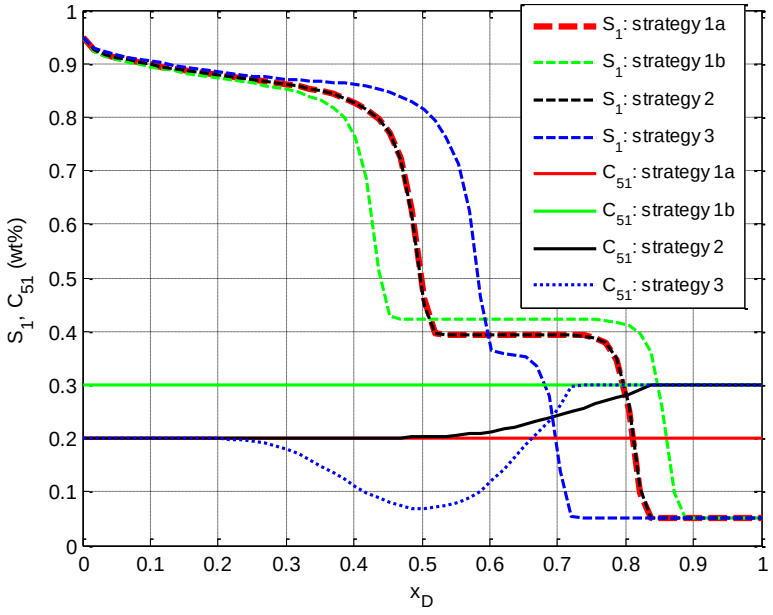

Figure 4.20: Profiles for saturation and salinity concentrations for different salinity injection strategies.

Additionally, to illustrate the effect of salinity variation on saturation-composition distributions and recovery efficiency during a polymer flooding, three main salinity injection strategies were considered: 1) continuous injection with the same injected and formation water salinities [two cases: a) lower ($C_{51} = 0.2wt\%$) and b) higher ($C_{51} = 0.3wt\%$) salinities], 2) continuous injection with injected salinity ($C_{51} = 0.2wt\%$) lower than formation salinity ($C_{51} = 0.3wt\%$), and 3) a slug size of $0.15PV$ injection with a very low salinity ($C_{51} = 0.02wt\%$) followed by a continuous injection with injected salinity ($C_{51} = 0.2wt\%$) lower than the formation salinity ($C_{51} = 0.3wt\%$). All strategies included a continuous polymer injection with concentration of $0.1wt\%$.

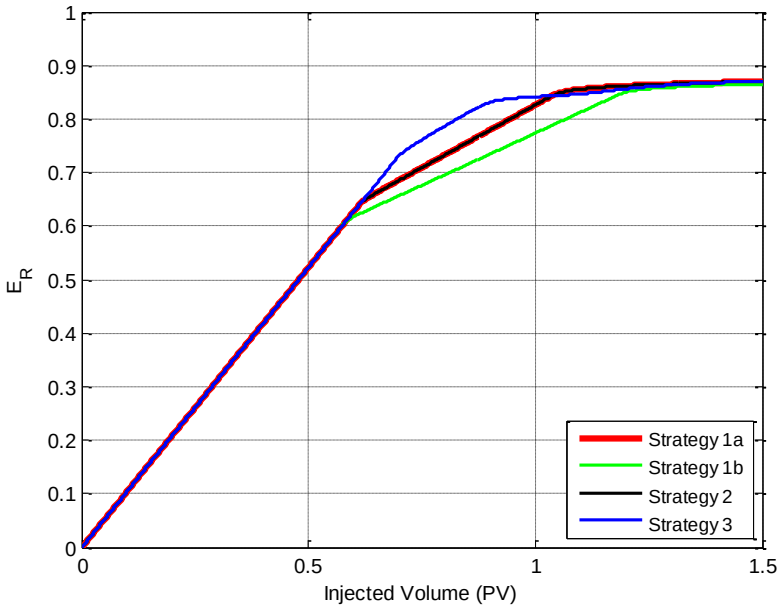

Figure 4.21: Recovery efficiency versus pore volume injected for different salinity injection strategies.

Figure 4.20 shows the results obtained for saturation profile and salinity concentration. Strategies 1a and 1b are references for high and low water injection salinity, respectively. Strategy 2 illustrates the salinity variation behind the displacement front, in which it decreases from formation salinity to injected salinity, and we observed that although salinity concentration profile is different to the one of strategy 1a, the behavior of saturation profiles and recovery efficiencies are the same in both strategies, as Figure 4.20 and Figure 4.21 illustrates. This, since the salinity injection in strategies 1a and 2 are the same even though the formation salinities are different, so the polymer rich front is affected by the same level

of salinity concentration. Therefore, the strategies 1a and 2 are governed by the same behavior of apparent viscosity and polymer adsorption.

Strategy 3 explores the benefits of starting the injection with a slug of lower salinity than the chase continuous injection salinity. Figure 4.20 shows the behavior of salinity concentration in this strategy, in which a decrement of the salinity behind the water displacement front from the salinity formation to a minimum value less than $0.07wt\%$ (near by $\mathrm{x}_D = 0.5$) is observed, and after this minimum, an increment of salinity concentration to injection salinity is identified. The salinity concentration values reached, between $\mathrm{x}_D \approx 0.25$ to $\mathrm{x}_D \approx 0.65$, allowed to achieve bigger apparent viscosities and less polymer adsorption, and so the polymer rich front presented a better performance than the one observed for polymer rich front of strategy 2. Therefore, strategy 3 yielded better recovery efficiencies, after breakthrough time of strategy 2 and before $1PV$ injected, as Figure 4.21 illustrates.

4.2.3 Effect of polymer adsorption

As we mentioned before, the flow equation that describes the displacement of petroleum by a polymer solution considers a term for the representation of chemical adsorption, and as we indicated previously, this could be modeled by a Langmuir-type isotherm.

To investigate the influence of adsorption phenomenon on fluid distribution and recovery efficiency, the second case in Figure 3.1 is chosen, where salinity of water formation is $C_{51} = 0.1wt\%$. This case is considered as 100% of the adsorption level (reference case) in Figure 4.22 and Figure 4.23, so by reducing the percentage of the adsorption level of the flow case at $t_D = 0.5$ and $C_{41} = 0.1wt\%$, the polymer adsorption effects on fluid distribution and petroleum recovery are studied.

Figure 4.22 shows the aqueous phase saturation and polymer concentration adsorbed profiles for the three cases, and it can be observed that as the adsorption level decreases, the water and polymer rich fronts get closer; water front is delayed, and polymer front goes faster. In addition, with less adsorption level the water saturation front reduces, and the polymeric solution front tends to be less sharp and spreads out toward water front. This results in differences for recovery efficiency behavior; the flow case with less adsorption level reaches faster the maximum recovery efficiency value, even though, the three cases get to the maximum recovery at different times, as Figure 4.23 illustrates. Figure 4.22 and Figure 4.23 expose the adsorption phenomena as a retardation term that defines the ratio

between front velocities and recovery times (Sorbie, 1991; Sheng, 2011; Herrera and Pinder, 2012).

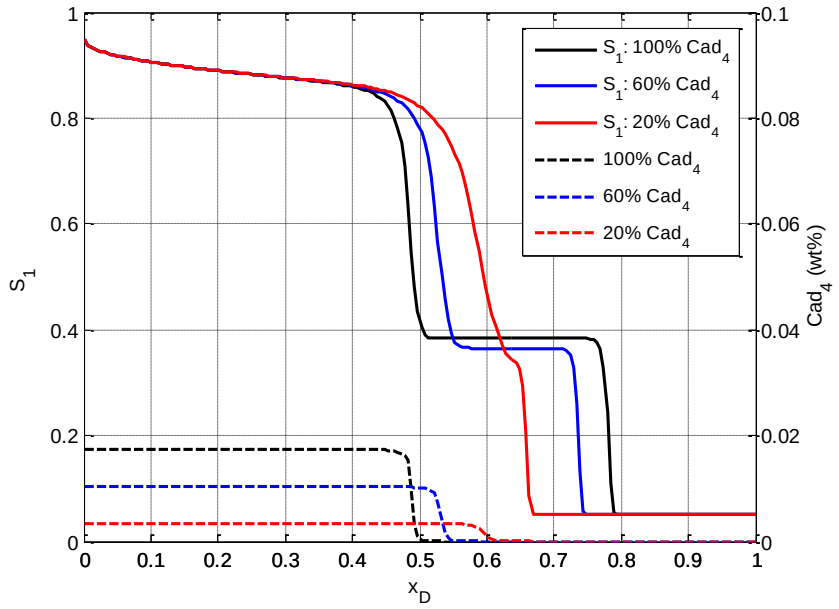

Figure 4.22: Profiles for saturation and adsorption concentrations, for 3 adsorption levels.

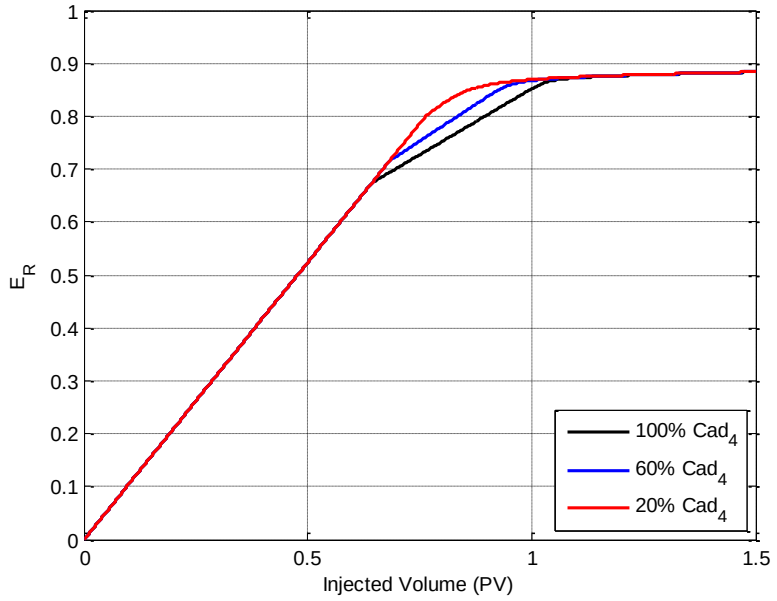

Figure 4.23: Recovery efficiency versus pore volume injected for 3 adsorption level.

4.2.4 Effect of permeability reduction

Polymer flooding causes permeability reduction due to adsorption phenomenon. This has an important role on mobility control for the increment of recovery efficiency. Therefore, in this section we research the effect of permeability reduction on fluid distribution and petroleum recovery.

As a measure of mobility control for the displacement, the mobility ration concept is used. For fractional flow theory with Corey type equations, one of the easiest expressions used is the end point water-oil mobility ratio, M^* (Lake, 1989; Dake, 1978; Rosado et al., 2006).

For waterflooding one displacement front is obtained, due to viscosities and relative permeabilities are not affected during the process, so M^* is constant in time and distance. Nevertheless, during polymer flooding a water front and a polymer rich front are presented, due to aqueous phase viscosity is function of time and distance. Additionally, end point water-oil mobility ratio should consider the effect of permeability reduction as equation (3.16) indicates.

M^* needs μ_{1app} and R_k, so it could be estimated a value for the water front and another for the polymer rich front. Thus, equation (3.16), as a profile, is used to analyze the behavior of mobility control. Therefore, Figure 4.24 presents four flow cases that compares the benefits of growing polymer concentration from $C_{41} = 0.0wt\%$ to $C_{41} = 0.1wt\%$, and the benefits of increasing permeability reduction factor from $R_k = 1$ to $R_k = 3.36$. Waterflooding case is for reference and, it can be observed that the four cases have the same M^* value in the water displacement zone, but different values after polymer rich displacement front.

First, the cases with unit permeability reduction factor are considered, and it is identified that as polymer concentration increase the displacement is more favorable, up to the point of $M^* = 0.07$ for the largest C_{41}. This value of M^* can also be achieved when we keep $C_{41} = 0.05wt\%$ and increment permeability retention to $R_k = 3.36$. Then, with a different combination of C_{41} and R_k the same degree of M^* is obtained, but at different polymer rich front locations, as Figure 4.24 depicts.

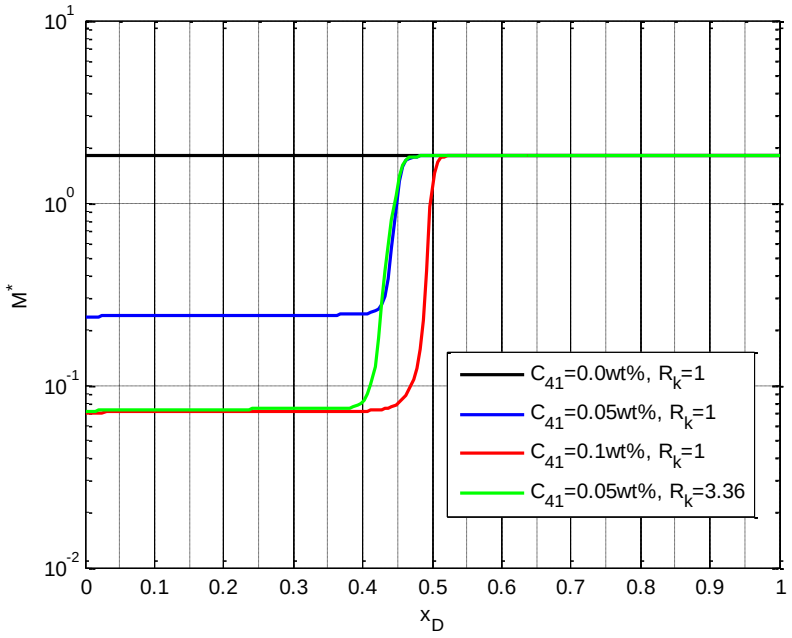

Figure 4.24: Profiles for end point water- oil mobility ration for different polymer concentration (C_{41}) and permeability reduction factor (R_k).

Figure 4.25 contributes to complement the flow cases in Figure 4.24, and it shows the fluid distribution and aqueous apparent viscosity behavior. It is identified that, for a $R_k = 1$, as polymer concentration grows water front velocity and water saturation front decreases while polymer front velocity and polymer rich saturation front increases, this makes the flow cases more favorable. Considering the two cases with the same $M^* = 0.07$; for the one with $R_k = 3.36$, its aqueous phase saturation behind the polymer rich front tends to the same trend as the case with $R_k = 1$; also, as permeability reduction factor increases, the water velocity and water saturation at the front increase, while the polymeric rich front velocity decreases.

The recovery efficiency behavior with the flow cases included in Figure 4.24 and Figure 4.25, is shown in Figure 4.26, and we observe that cases with $R_k = 1$; after water breakthrough and as polymer concentration increases the efficiency recovery increases. Comparing the two cases where $M^* = 0.07$ (as Figure 4.24 illustrates), both eventually reach the same maximum recovery efficiency ($E_R = 0.86$), with the difference that the case of unit permeability reduction factor gets the maximum recovery efficiency before the case for $R_k = 3.36$, so the former presents more favorable conditions for polymer flooding.

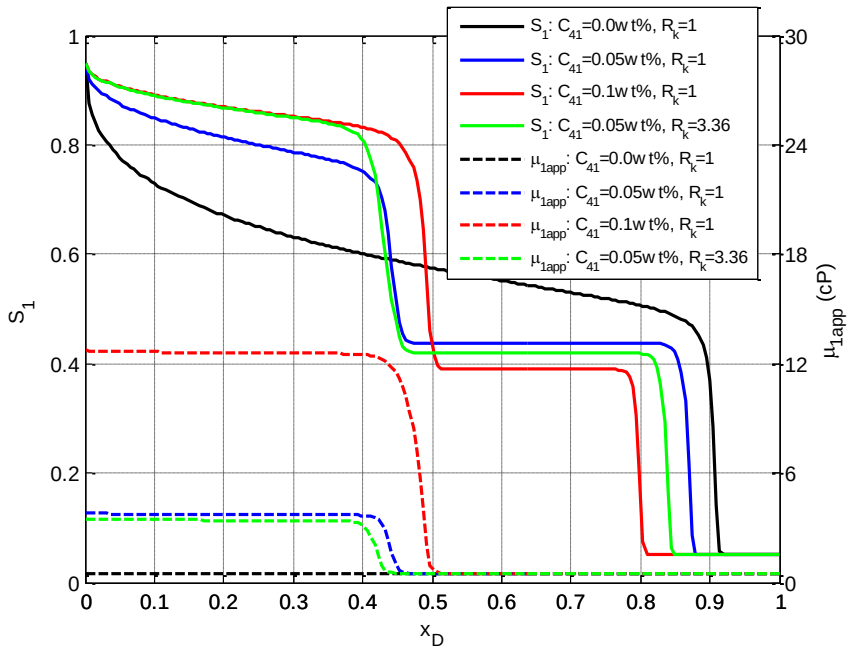

Figure 4.25: Saturation profiles and apparent viscosity distributions for different polymer concentration (C_{41}) and permeability reduction factor (R_k).

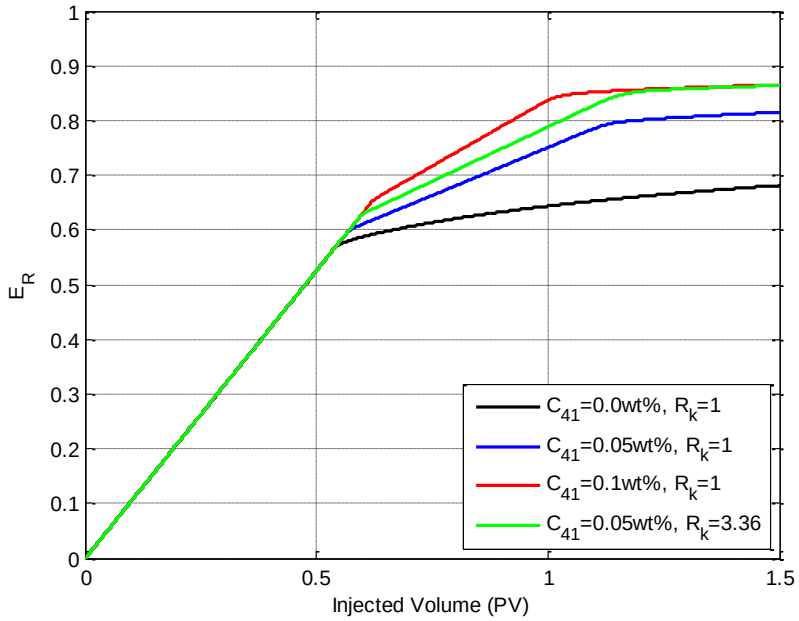

Figure 4.26: Recovery efficiency versus pore volume injected for different polymer concentration (C_{41}) and permeability reduction factor (R_k).

4.2.5 Effect of slug size

The flow cases discussed are related to a continuous injection scheme at fixed polymer concentration. Chemical injection strategy has an important role in the success of a CEOR project (Druetta and Picchioni, 2018). In this section, two types of scenarios are considered: 1) a fixed chemical slug size with varying polymer concentration and, 2) a fixed polymer concentration with changing slug size.

The numerical tool built allows to track flow properties, as the example in Figure 4.27 presents at a snapshot of $0.5PV$ injected with a polymer slug size of $0.25PV$ and chemical concentrations for polymer and salinity of $C_{41} = 0.1wt\%$ and $C_{51} = 0.1wt\%$. After slug injection, chase water follows with the same water salinity. This Figure illustrates aqueous saturation, polymer, effective salinities, and adsorption concentration profiles, as well as viscosity at zero shear rate and apparent viscosity of polymeric solution.

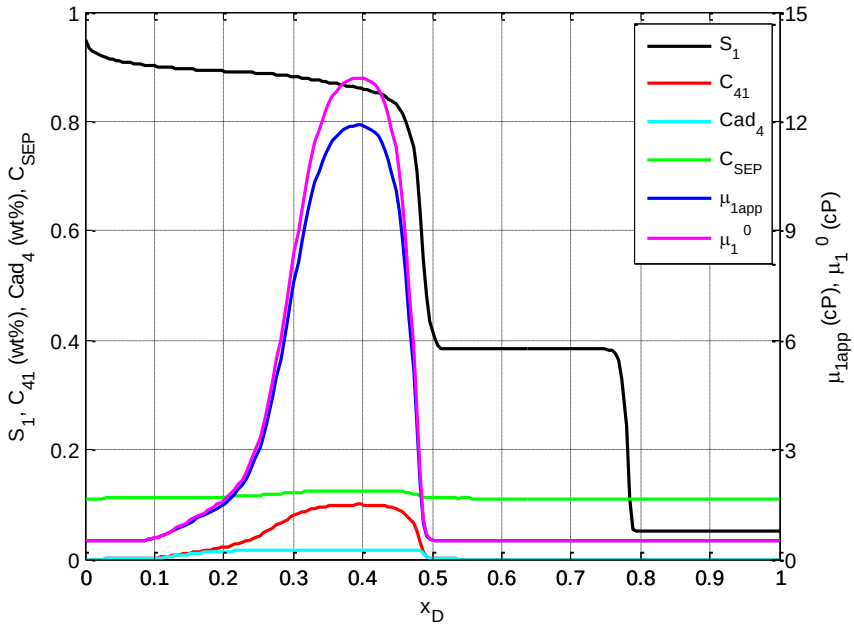

Figure 4.27: Profiles for saturation, chemical concentration and viscosities, at $0.5PV$ *injected with a slug size of* $0.25PV$.

Figure 4.27 illustrates that the aqueous saturation profile shows two shock fronts, and between them, all properties are practically constant. At the rich polymer front, chemical concentrations abruptly increase from zero to near injection concentration and, when chemical slug size finished polymer and effective salinity content gradually decreases to

initial concentrations. Polymer viscosities (at zero shear rate and apparent viscosities) and adsorption behave similarly to chemical concentration.

The evolution of saturation profiles and polymer concentration for a slug injected size of $0.25PV$ with chemical concentrations of $C_{41} = 0.1wt\%$ and $C_{51} = 0.1wt\%$, at three times is illustrated in Figure 4.28. $t_D = 0.25$ is the time when the polymer slug injection finishes, $t_D = 0.63$ is the water breakthrough time and $t_D = 0.44$ is the intermediate time between the two previous mentioned. From this Figure, it is observed that as time goes by the separation between the water front and the polymer rich front increases due to water front moves faster than the other front, as well as, the peak level and the width around peak of the polymer concentration curve (bell shaped curve) decreases. In addition, it can be deduced that due to the level of polymer concentration applied to this case, the effect of polymer dilution does not have a relevant role on changing polymer shock front and, on reducing the benefits of polymer injection. Therefore, this indicates that, the content of polymer to used could be optimized by considering an appropriate combination of polymer concentration and polymer slug size to be injected.

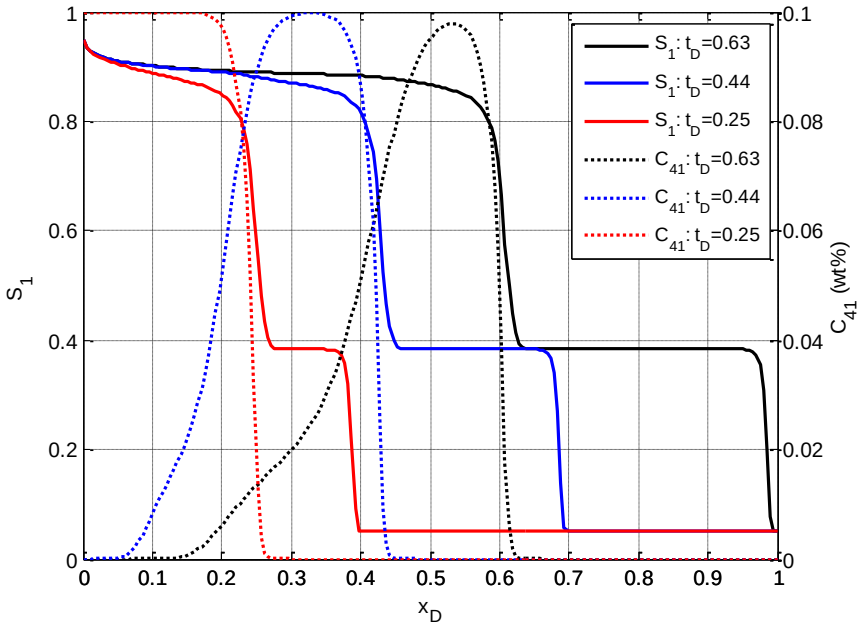

Figure 4.28: Profiles for saturation and polymer concentration with a slug size of $0.25PV$ *and* $C_{41} = 0.1wt\%$.

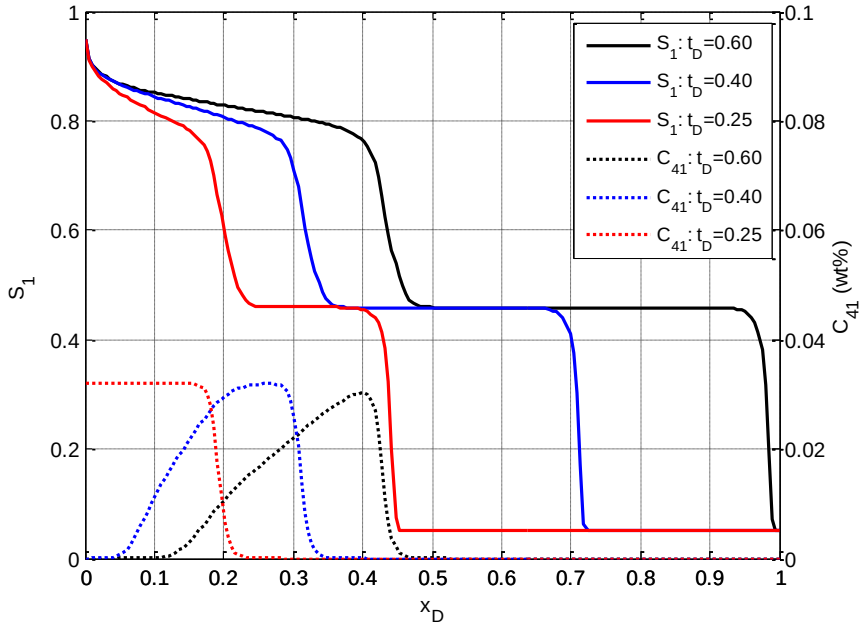

Figure 4.29: Profiles for saturation and polymer concentration with a slug size of $0.25PV$ *and* $C_{41} = 0.032wt\%$.

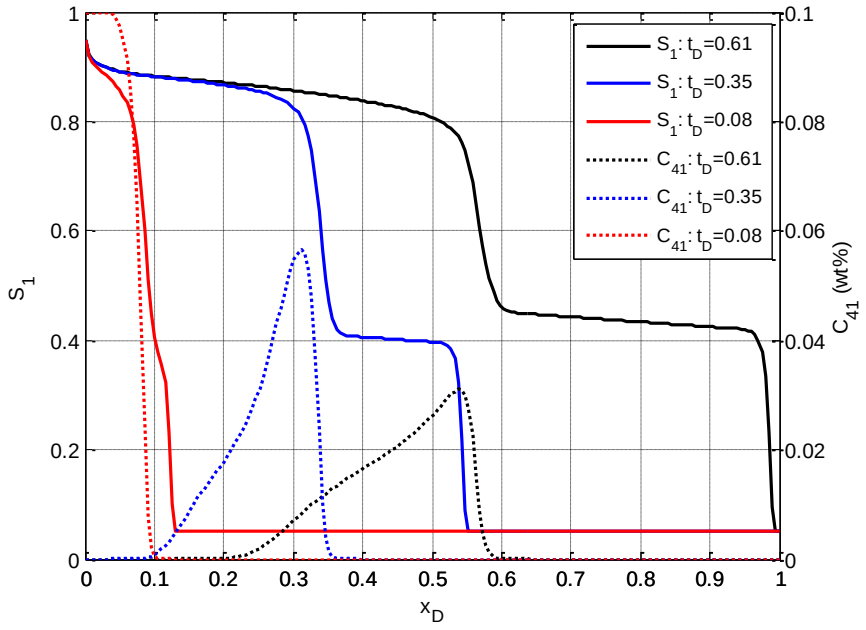

Figure 4.30: Profiles for saturation and polymer concentration with a slug size of $0.08PV$ *and* $C_{41} = 0.1wt\%$.

To analyze the consequences of reducing polymer content in the displacement process of Figure 4.28; polymer concentration is reduced about 70% (from $0.1\text{wt}\%$. to $0.032\text{wt}\%$), and the results are presented in Figure 4.29. Comparing both cases, it can be seen that in the case with less polymer concentration, water breakthrough appears earlier with a higher water saturation, and polymer rich front moves slower with a lower water saturation at the front. As a result, the case in Figure 4.29 takes less benefits from the polymer flooding than the case in Figure 4.28.

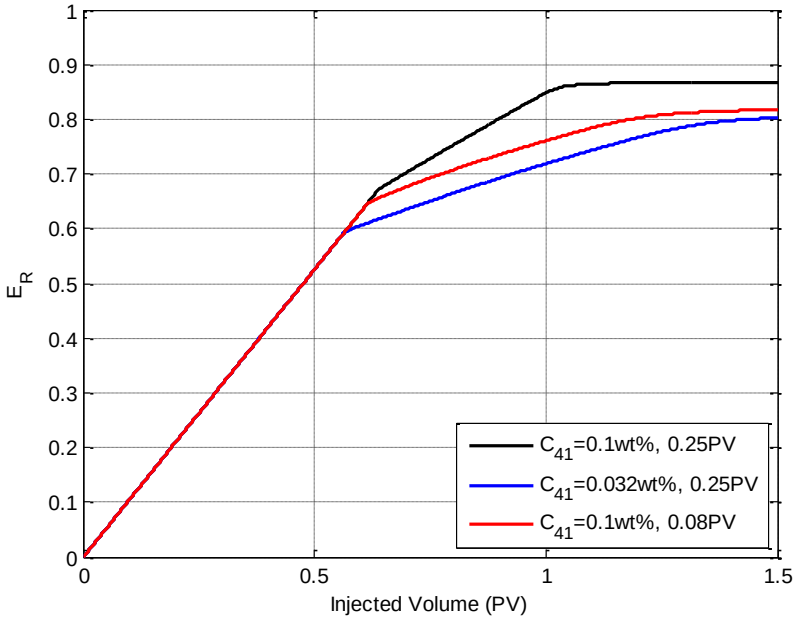

Figure 4.31: Recovery efficiency versus pore volume injected for three cases of slug injection.

Changing polymer slug size could be another way to adjust the amount of polymer needed for a flooding. From Figure 4.28 and Figure 4.30, slug size is reduced from $0.25PV$ to $0.08PV$, and it is observed that the latter case takes less advantage of the polymer flooding benefits than the case in Figure 4.28, although water breakthrough occurs almost at the same time. This displacement with polymer injection during $0.08PV$ let to appreciate a condition where polymer shock front and its benefits are considerable affected by polymer dilution to the extent that, even though the maximum of polymer concentration at the end of chemical injection is $0.1wt\%$, as in Figure 4.28, it is reduced about 70% at water breakthrough. Besides, it is noticed that in the less efficient process, water saturation does not remain

constant in the region between water front and polymer rich front saturations, and thus, reducing the performance of the polymer displacement.

Figure 4.31 complements the analysis of the flow cases from Figure 4.28 to Figure 4.30. Then, it can be seen that the case with higher polymer concentration and longest polymer injection time is the case with the better benefits of polymer flooding, due to it has the longest water breakthrough time and the highest recovery efficiency. For the other two cases, considering that both contain the same mass of polymer inside the reservoir, the case in Figure 4.30 yields a better scenario than the case in Figure 4.29, because of the former case reaches higher cumulative petroleum production and a longest water breakthrough time. It can also be identified that as time increments, the case in Figure 4.29 tends to achieve the recovery efficiency of the case in Figure 4.30.

4.2.6 Effect of reversible and irreversible adsorption

So far, the polymer flooding cases have assumed reversible adsorption, in terms of polymer concentration. However, depending on rock-fluid chemical composition, some cases need to consider adsorption as an irreversible process. Therefore, the effect of the adsorption irreversibility is explored, by comparing the reversible adsorption case, explained in Figure 4.30, and the flow case with the same conditions of such figure but including irreversible adsorption.

Applying the simulation tool developed, Figure 4.32 represents the adsorption behavior during the polymer flooding case of Figure 4.30, and we can observe that, as time goes by, the area under the curve of polymer adsorption tends to increase accordingly to Langmuir, equation (3.17) and, by considering the mass of polymer adsorbed onto formation rock, the polymer slug is degraded.

For an irreversible adsorption process, the Langmuir model cannot be used directly when the polymer concentration is declining (Sheng, 2011). An additional parameter must be used to track the adsorption history, so that, it is selected the maximum polymer adsorption concentration without exceeding the adsorption capacity. Taking into account this artifice for the numerical simulation tool, Figure 4.33 shows the theoretical approximation of polymer flooding performance in Figure 4.32 but including irreversible adsorption. And, it is observed the evolution of polymer adsorption, such that, polymer concentration and polymer adsorption concentration near the polymer front decreases to almost zero at water

breakthrough time. Besides, the polymer adsorbed onto the rock is larger than the case in Figure 4.32, in fact it is so large that polymer slug is almost completely consumed when water reaches the production well, and so, at this time almost all polymer mass injected is adsorbed onto the rock surface.

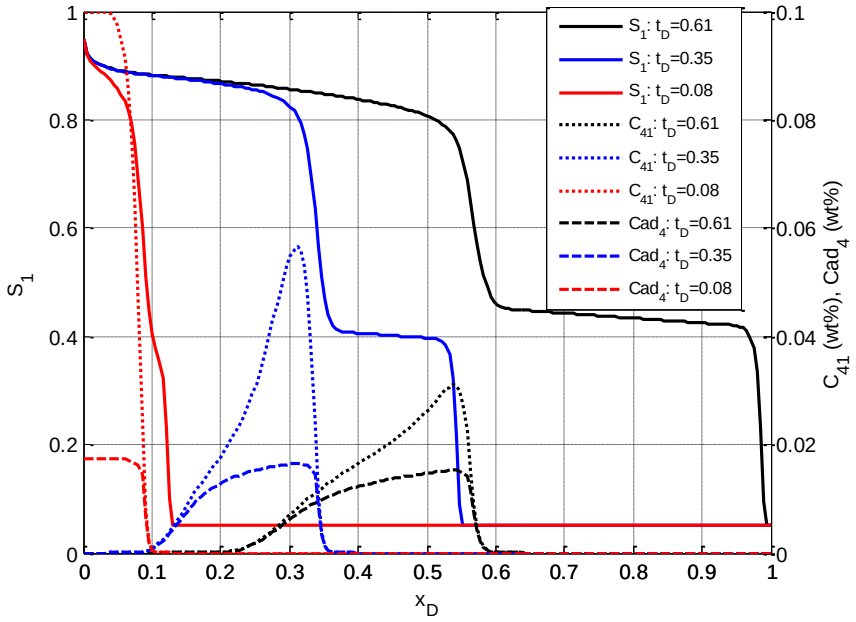

Figure 4.32: Profiles for saturation, polymer and adsorption concentrations with a slug size of $0.08PV$, $C_{41} = 0.1wt\%$ *and reversible adsorption.*

Figure 4.34 presents the recovery behavior comparison of the cases for reversible and irreversible adsorption, and we identify that, although both cases yield almost the same water breakthrough time, the case with a reversible process gets more benefits by polymer flooding than irreversible process. This is because of consumption of polymer is larger in the case of irreversible adsorption then reversible one, as Figure 4.32 and Figure 4.33 display.

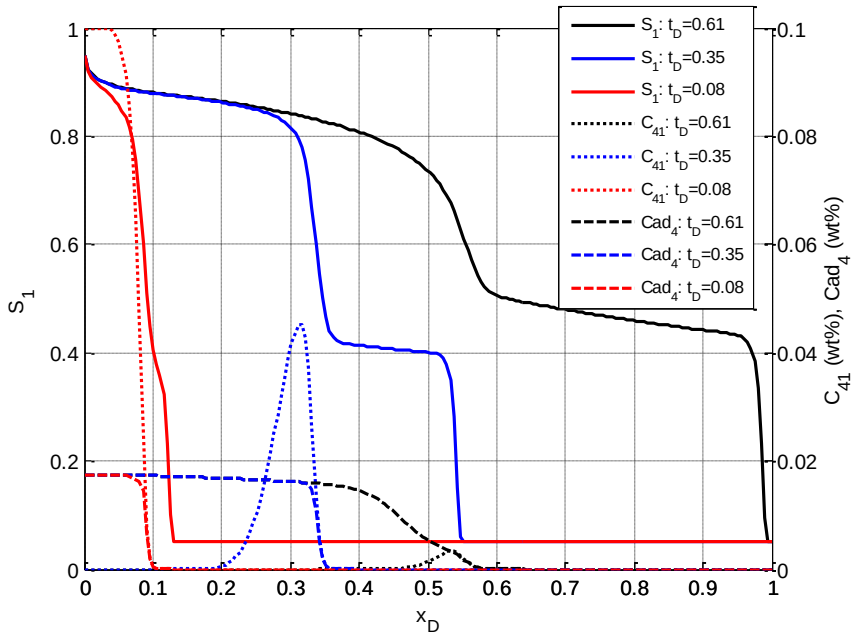

Figure 4.33: Profiles for saturation, polymer, and adsorption concentrations with a slug size of $0.08PV$, $C_{41} = 0.1wt\%$ *and irreversible adsorption.*

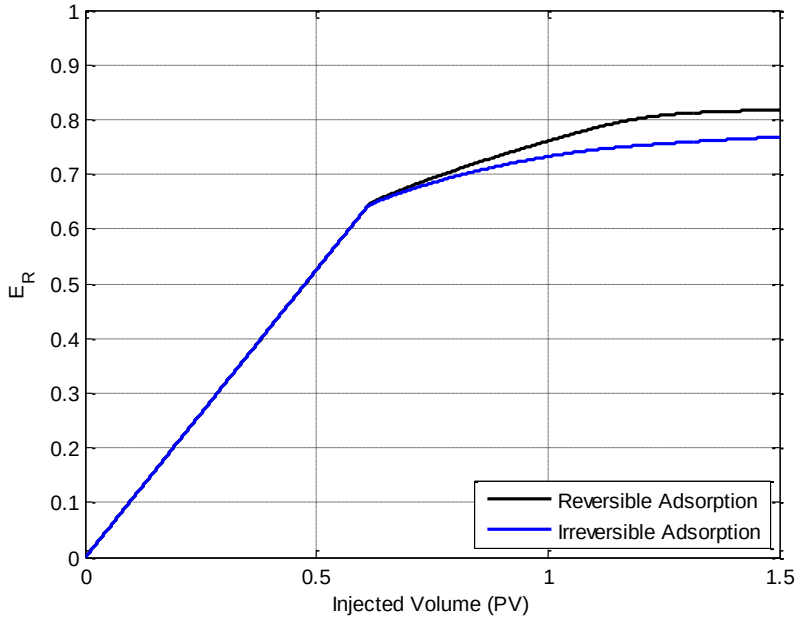

Figure 4.34: Recovery efficiency versus pore volume injected for reversible and irreversible adsorption.

Chapter 5: Streamline-based modelling of polymer flooding

5.1 Fundamentals of streamline simulation

This technique has been applied for more than 50 years in the petroleum industry. With the advances of computer performance, streamline models provides a tool for a fast flow simulation and a quick screening and ranking 3D reservoir models. The flood front development and the interaction with heterogeneities can be visualized easy using streamline models.

The streamline methods use concepts for particle tracking to define pathlines in 3D space and introduces the streamline "time of flight" (TOF) as a spatial variable (the travel time of a neutral tracer along streamlines). This and other concepts involved in streamline simulation are described as follow (Datta-Gupta and King, 2007):

- *Streamline*. - the streamlines are integrated curves, that are locally tangential to the direction of the velocity. Streamlines are based on instantaneous velocity, so they are traced from a snapshot of the velocity at a time of interest. A related definition is that of a *pathline*; that is the trajectory of a neutral tracer particle as it moves through space and time. By construction, streamlines can never cross.

- *Streamtube.* - In two dimensions, a streamtube is the region bounded by a pair of streamlines, and no convective flux will cross the boundaries of a streamtube. Therefore, within each tube, we could have a 1D description of flow by the average Darcy velocity at any location been equal to the volumetric flux in the streamtube divided by the cross-sectional area of the tube. Widely spaced streamtubes correspond to slow flow, and narrow streamtubes correspond to fast flow.

- *Time of flight.* – Introduce a neutral (non-reactive) particle at an injection well or at an influx boundary of the domain. Let the particle to move according to the instantaneous interstitial velocity and measure the time it takes to arrive at a point. This is the definition of the time of flight, $\tau(x,y,z)$ for that point. Then, for streamline simulation it is fundamental to use the time of flight primary as a spatial coordinate.

- *Streamfunction.* – For 2D incompressible fluid flow, it possible to determine the fluid velocity from the derivative of a function called the streamfunction (a scalar quantity, ψ, and like pressure it is determined relative to a reference point). The streamfunction at any point is defined as the volumetric flux, normalized per unit thickness. The difference between two points is independent of the path, so long as the path does not loop around a well. When a streamfunction is known, the contours of the streamfunction can be used to determine the streamlines.

In streamline simulation, we calculate de velocity by the solution of a finite difference problem and trace the streamline using that velocity, then it is associated a volumetric flux with each streamline.

Streamline simulators approximate a 3D fluid flow calculations by a sum of 1D solutions along streamlines. This approach is extremely effective for modeling convective-dominated flows in the reservoir, in which typically heterogeneity is the predominant factor governing the flow behavior. The geometry and density of streamlines reflect the impact of geology on flow paths, providing better solution in regions of faster flow.

5.2 Streamlines model for polymer flooding

5.2.1 Model for pressure, saturation, and composition 2D distribution

For the streamline technique it is necessary to calculate the pressure distribution to the construction of the streamlines. For the mathematical model, we adapted the strategy presented by Sorbie (1991), in which pressure and saturations are estimated with the equations for non-compositional multiphase flow because the components are only in the aqueous phase, and each of them are computed with an advection-reaction equation.

Then, the mass conservation equation is as follow (Bear, 1972; Chen et al, 2006).

$$\frac{\partial(\phi\rho_j S_j)}{\partial t} = -\nabla\cdot\left(\rho_j\vec{u}_j\right) + q_j \qquad (5.1)$$

For this section, the assumptions for the flow model are a black oil formulation, 2D x-y darcian flow, heterogeneous and anisotropic porous medium, fluids and rock are incompressible, negligible gravity and capillary effects, no dispersive effects nor convective dispersion.

With these considerations, the flow model, equation (5.1), (Ertekin et al., 2001), becomes,

$$\frac{\partial}{\partial x}\left(k_x A_x \frac{k_{rj}}{\mu_j B_j}\frac{\partial p_j}{\partial x}\right)\Delta x + \frac{\partial}{\partial y}\left(k_y A_y \frac{k_{rj}}{\mu_j B_j}\frac{\partial p_j}{\partial y}\right)\Delta y = V_b \frac{\partial}{\partial t}\left(\frac{\phi S_j}{B_j}\right) - q_{scj}, \quad j = 1,2 \qquad (5.2)$$

The compositional description considered an adaptation of the equation presented by Pope et al. (1981) and the aqueous transport equation for compositional-multiphase flow previously derived by Rosado et al. (2022) to establish the 2D flow as follows:

$$\phi \frac{\partial}{\partial t}\left[C_{i1}S_1 + \hat{C}_i\right] + \frac{\partial}{\partial x}\left[u_{x1}C_{i1}\right] + \frac{\partial}{\partial y}\left[u_{y1}C_{i1}\right] = 0 \qquad i = 1,2,\cdots,N_C \qquad (5.3)$$

These equations have no analytical solution and must be solved numerically to obtain an approximate solution. The finite differences method was used, and the nonlinear set of algebraic equations obtained from the finite difference approximation of the differential flow equations, (5.2), was solved applying the IMPES method. The difference equations for grid points (i, j) and non-linearities treated according to IMPES can be written as follows:

$$T^n_{jy,(i,j-1/2)}p^{n+1}_{2,(i,j-1)} + T^n_{jx,(i-1/2,j)}p^{n+1}_{2,(i-1,j)} - \left[T^n_{jy,\left(i,j-\frac{1}{2}\right)} + T^n_{jx,\left(i-\frac{1}{2},j\right)} + T^n_{jx,\left(i+\frac{1}{2},j\right)} + T^n_{jy,\left(i,j+\frac{1}{2}\right)}\right]p^{n+1}_{2,(i,j)} + T^n_{jx,\left(i+\frac{1}{2},j\right)}p^{n+1}_{2,(i+1,j)} + T^n_{jy,\left(i,j+\frac{1}{2}\right)}p^{n+1}_{2,(i,j+1)} = C^n_{jw,(i,j)}\left(S^{n+1}_{1,(i,j)} - S^n_{1,(i,j)}\right) - q^{n+1}_{scj,(i,j)} \qquad j = 1,2 \qquad (5.4)$$

$$T_{jx} = \frac{k_x A_x}{\Delta x}\frac{k_{rj}}{\mu_j B_j} \qquad j = 1,2 \qquad (5.5)$$

$$T_{jy} = \frac{k_y A_y}{\Delta y}\frac{k_{rj}}{\mu_j B_j} \qquad j = 1,2 \qquad (5.6)$$

$$C_{2w} = -\frac{V_b}{\Delta t}\left(\frac{\phi}{B_2}\right) \qquad (5.7)$$

$$C_{1w} = \frac{V_b}{\Delta t}\left(\frac{\phi}{B_1}\right) \qquad (5.8)$$

The IMPES method approach consists of obtaining a pressure equation for each gridblock by properly combining equations (5.4) for water and oil to eliminate the saturation unknows; in doing so, transmissibilities must be evaluated explicitly, at time level n, and flow properties needed are calculated according to saturations and polymer solution properties described in section 3.1.3. The combined pressure equation is written for each grdiblock and the linearized algebraic system of equations solved implicitly for the oil phase pressure

distribution at time level $n+1$. Then, the saturation unknows are solved explicitly in each gridblock by substituting the pressures calculated at that time level in equation (5.4).

In the strategy presented by Sorbie (1991), once pressure and saturation were determined, a numerical approach to the advection-reaction equation (5.3) can be derived with an upwind explicit finite difference scheme to discretize the flow equations at grid points (i,j), so the concentration of each component is updated explicitly at time level $n+1$, with the following numerical approximation:

$$\phi_{(i,j)}\frac{(C_{i1}S_1)^{n+1}_{(i,j)}-(C_{i1}S_1)^{n}_{(i,j)}}{\Delta t}+\phi_{(i,j)}\left[\frac{d\hat{C}_i}{dC_{i1}}\right]^n_{(i,j)}\frac{{C_{i1}}^{n+1}_{i,(i,j)}-{C_{i1}}^{n}_{i,(i,j)}}{\Delta t}+\frac{\left[(C_{i1}u_{x1})_{(i+1/2,j)}-(C_{i1}u_{x1})_{(i-1/2,j)}\right]^n}{\Delta x}+$$

$$\frac{\left[(C_{i1}u_{y1})_{(i,j+1/2)}-(C_{i1}u_{y1})_{(i,j-1/2)}\right]^n}{\Delta y}=0 \qquad (5.9)$$

The convective term is evaluated with an upstream criterion for concentrations and phase velocities at every cell face of the grid by applying Darcy´s law. The velocities are very important to the construction of the streamlines, as it will be described later. Models to represent key phenomena for polymer flooding and flow properties required are defined in section 3.1.3, and evaluated at each gridblock, for each time level n.

With the saturations and concentrations determined for each grid cell, we can estimate fluid saturation and composition values on any streamline. The method considers a flow from upstream to downstream on a streamline passing through two gridblocks with different saturations. According to the discretization along the streamline, the segment ($\Delta\tau$) that falls within these two cells can be divided in two, and a weighted average saturation is calculated (Datta-Gupta and King, 2007).

$$\bar{S}_1=\frac{[\Delta\tau S_1]_{upstream}+[\Delta\tau S_1]_{downstream}}{\Delta\tau} \qquad (5.10)$$

This procedure to compute the weighted average saturation is analogous to that applied in the calculation of weighted average compositions.

Figure 5.1 summarizes the procedure to estimate pressure, saturations, and compositions distributions in the 2D grid, required to build or update streamlines of the polymer flooding simulator. According to Jun and Minglu (2011), the update of the streamlines can derive from conditions such as closing producing wells with high water cut, infill well pattern by drilling new wells, re-perforating or modifying layers for old wells, and so on.

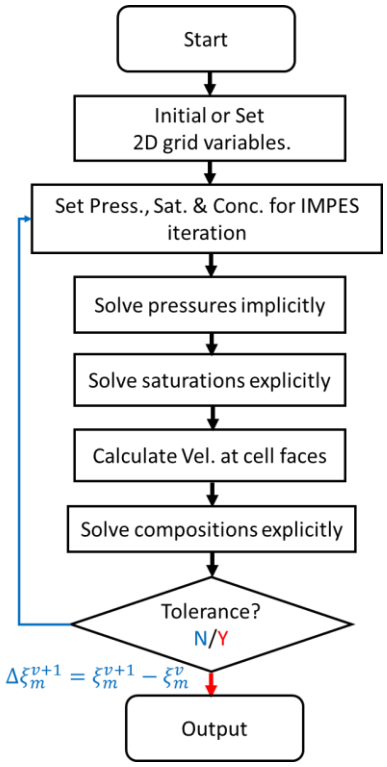

Figure 5.1: Flowchart of the numerical simulator for estimating pressure, saturations, and concentrations for a 2D distribution.

5.2.2 Polymer flooding model along streamlines

To develop the streamline-based mathematical model, a definition of the time of flight is needed, as well as the application of the gradient operator in the time of flight coordinates for a spatial transformation between coordinates (Datta-Gupta and King, 2007).

The time of flight refers to a specific coordinate that is used along streamlines, this is especially effective in representing the effect of spatial heterogeneity upon flow. To define $\tau(x, y, z)$, we can release a tracer particle that moves at interstitial speed, from an injector, and determine the time it takes for the tracer particle to reach that position. Hence, the time of flight can be represented from the following integral.

$$\tau = \int_0 \frac{\phi}{|\vec{u}|} d\zeta \tag{5.11}$$

where $(\vec{u}/\phi)$ is the interstitial velocity and ζ is the spatial distance along streamline. The previous equation can be written as a differential relationship,

$$\vec{u} \cdot \nabla\tau = \phi \tag{5.12}$$

For time varying velocities and considering that bistreamfunctions (ψ and χ) can determine particle velocity (Bear, 1972), the velocity is approximated as a sequence of steady state intervals, each with its own time of flight and bistreamfunctions. Therefore, a spatial transformation from (x, y, z) to (τ, ψ, χ) can be established by the Jacobian of the transformation that relates volume elements in these two spaces.

$$\left\|\frac{\partial(\tau,\psi,\chi)}{\partial(x,y,z)}\right\| = \|(\nabla\psi \times \nabla\chi) \cdot \nabla\tau\| = \|\vec{u} \cdot \nabla\tau\| = \phi \tag{5.13}$$

In terms of volume, we have:

$$\phi dx dy dz = d\tau d\psi d\chi \tag{5.14}$$

Then, a unit volume in the time-of-flight coordinates corresponds to a unit volume pore volume in physical space. This is an important link between spatial discretization in finite difference and in streamline simulation.

Now, the spatial gradient along streamlines, in the time of flight coordinates, can be expressed as:

$$\nabla = \nabla\tau \frac{\partial}{\partial\tau} + \nabla\psi \frac{\partial}{\partial\psi} + \nabla\chi \frac{\partial}{\partial\chi} \tag{5.15}$$

Because $\vec{u}$ is orthogonal to both $\nabla\psi$ and $\nabla\chi$,

$$\vec{u} \cdot \nabla = \phi \frac{\partial}{\partial\tau} \tag{5.16}$$

The identity operator is fundamental in streamline simulation, and it is used to transform equations from the physical space to the streamline time of flight coordinates. Then, considering the conservation equation for water phase in two phase incompressible flow, neglecting gravity and capillarity,

$$\phi \frac{\partial}{\partial t}[S_1] + \nabla \cdot (f_1 \vec{u}_t) = 0. \tag{5.17}$$

Using $\nabla \cdot \vec{u} = 0$, from the incompressibility condition (Datta-Gupta and King, 2007; Herrera and Pinder, 2012), and equation (5.16) to transform from the physical space to time of flight coordinates, it follows from equation (5.17) that,

$$\frac{\partial}{\partial t}[S_1] + \frac{\partial}{\partial\tau}[f_1] = 0 \tag{5.18}$$

This equation decomposes the 3D, or 2D, fluid flow into a series of 1D flow equation for water saturation along streamlines.

The physical meaning of the τ coordinate is evident when we compare the equation (5.18) to the well-known Buckley-Leverett equation (equation 3.8),

$$\frac{\partial}{\partial t_D}[S_1] + \frac{\partial}{\partial x_D}[f_1] = 0. \tag{3.8}$$

Here, we can notice that τ coordinate acts as a measure of a spatial distance.

Now, applying this coordinates transformation technique to the model for polymer flooding developed in chapter 3, we can establish the following system of nonlinear differential equations for water, polymer, and salt; components 1, 4 and 5, respectively:

$$\frac{\partial}{\partial t}[S_1] + \frac{\partial}{\partial \tau}[f_1] = 0 \tag{5.19}$$

$$\frac{\partial}{\partial t}\left[C_{41}S_1 + \hat{C}_4\right] + \frac{\partial}{\partial \tau}[f_1 C_{41}] = 0 \tag{5.20}$$

$$\frac{\partial}{\partial t}[C_{51}S_1] + \frac{\partial}{\partial \tau}[f_1 C_{51}] = 0 \tag{5.21}$$

with $S_1(\tau, t)$, $C_{41}(\tau, t)$ and $C_{51}(\tau, t)$ as unknowns. Initial and boundary conditions, that complete the definition of the problem, can be adequate to any condition state of previous production, polymer injection strategies and other operational conditions. The flow cases simulated in this research, consider that the reservoir is initially saturated with oil and irreducible water at some initial salinity. At the injection boundary, water saturation is always at its maximum value. The injection strategy can be for continuous polymer injection, a slug polymer from the beginning of the injection, a slug polymer after some water injection, and polymer injection as a secondary process.

This set of equations represent a compositional model that considers non-Newtonian rheology, permeability reduction, irreversible or reversible polymer adsorption, as a function of polymer and salinity concentrations. It includes four components and two phases, as it was described in chapter 3, when it was considered the physical space coordinate. This mathematical model has no analytical solution, but it can be solved by numerical techniques, such as finite difference.

The equations (5.19) - (5.21) can be represented by a general form:

$$\frac{\partial}{\partial t}\left[C_{i1}S_1 + \hat{C}_i\right] + \frac{\partial}{\partial \tau}\left[f_1 C_{i1}\right] = 0 \qquad (5.22)$$

where i refers to components. This equation is discretized by finite differences in time of flight coordinate. The discretized nonlinear equations, at node $\not{f}$ and time step $n+1$, is written in residual ($R\varepsilon$) form as,

$$R\varepsilon_{i,\not{f}}^{n+1} = \frac{(C_{i1}S_1)_{\not{f}}^{n+1} - (C_{i1}S_1)_{\not{f}}^{n}}{\Delta t} + \frac{\hat{C}_{i,\not{f}}^{n+1} - \hat{C}_{i,\not{f}}^{n}}{\Delta t} + \frac{\left[(C_{i1}f_1)_{\not{f}} - (C_{i1}f_1)_{\not{f}-1}\right]^{n+1}}{\Delta \tau} = 0$$
$$i = 1,4,5; \quad \not{f} = 2,3,\ldots F-1; \quad n = 1,2,3,\ldots \qquad (5.23)$$

It follows from this equation that at each time level, $n+1$, a system of 3x(F-2) non-linear algebraic equations, in the same number of unknowns, has to be solved. The solution was obtained by the Newton-Raphson (NR) iterative method. The details of this method are described chapter 4 for the analogous problem.

Either for continuous injection or slug injection schemes, the boundary conditions are Dirichlet-type, then, S_1, C_{41} and C_{51} must be specified at nodes $\not{f} = 1$ and F in all time levels. Initial conditions, $n = 0$, for concentrations and saturation must also be specified in all nodes. It is important to emphasize that the validation of the numerical algorithm associated to (5.23) was carried out in chapter 4 for the analogous flow problem.

After calculating concentrations and saturations along the streamlines by the polymer flooding model, we can apply a procedure for mapping saturations and concentrations from streamlines to the 2D gridblocks. The saturation that is assigned to a cell is the pore-volume-weighted average of the saturations segments that intersect the cell. The pore-volume-weighted is given in the following (Datta-Gupta and King, 2007):

$$\bar{S}_1 = \frac{\sum_s \Delta Q_s \sum_{\not{f}} (S_1)_{s\not{f}} \Delta\tau_{s\not{f}}}{\sum_s \Delta Q_s \sum_{\not{f}} \Delta\tau_{s\not{f}}}. \qquad (5.24)$$

where $\not{f}$ is the index for the time-of-flight discretization and s is the index for the streamline indicated. Then, ΔQ_s is the volumetric flux in the streamline s. For compositions we apply an analogous procedure.

For the mapping procedure, the approach of equation (5.24) works well for cases in which the gridblocks contain enough streamlines passing through (one at least). In gridblocks with insufficient streamlines, we implement the inverse distance weighting method, as a spatial predictive technique (Shepard, 1968; Pyrcz et. al, 2014), after equation (5.24) is applied in all gridblock where possible.

5.2.3 Streamline construction

For the construction of the streamlines and the estimation of the time of flight, the procedure follows the algorithm proposed by Pollock (Pollock, 1988). This approach starts with a numerical solution for pressure distribution using a finite difference technique, then the volumetric fluxes using Darcy's law are computed for each cell face.

In every gridlock, Pollock's algorithm applies a velocity model that assumes that the velocity of the components, in a given direction, varies linearly in each gridcell between the values at the appropriate pair of cell boundaries. This yields the following cell velocity models for each coordinate:

$$u_\varsigma = u_{\varsigma 1} + c_\varsigma(\varsigma - \varsigma_1), \qquad \varsigma = 1,2,3, \tag{5.25}$$

where ς is the spatial coordinate; 1 for x coordinate, 2 for y coordinate, and 3 for z coordinate, and the coefficients are velocity gradients equal to the difference of the Darcy velocities on the gridblock faces divided by the size of the cell in the corresponding direction.

Form equation (5.25), it can be settled that

$$\nabla \cdot \vec{u} = \sum_{\varsigma=1}^{3} c_\varsigma. \tag{5.26}$$

This relationship is important, and according to the incompressible flow condition it will be stated that $c_x + c_y + c_z = 0$.

To estimate the time of flight along a streamline in a cell, the following equation applies based on equation (5.16):

$$\frac{d\tau}{\phi} = \frac{d\varsigma}{u_\varsigma} \tag{5.27}$$

Combining this equation with (5.25), the time of flight to each of the faces of the gridblock is obtained as,

$$\frac{\Delta\tau_{\varsigma l}}{\phi} = \frac{1}{c_\varsigma} ln\left(\frac{u_{\varsigma l}}{u_{\varsigma 0}}\right) \tag{5.28}$$

The index $l = 1,2$ indicates the gridblock faces in each direction. From all the possible exit faces of the cell, the correct one it is related to the minimum positive transient time, thus

$$\Delta\tau = Min\ Positive\left\{\Delta\tau_{\varsigma l}\right\} = Min\ Positive\left\{\Delta\tau_{x1}, \Delta\tau_{x2}, \Delta\tau_{y1}, \Delta\tau_{y2}, \Delta\tau_{z1}, \Delta\tau_{z2}\right\} \tag{5.29}$$

With the correct time of flight, the exit coordinates can be estimated by rearranging the equations of this section:

$$\varsigma = \varsigma_0 + u_{\varsigma 0}\left(\frac{e^{c_\varsigma \Delta\tau/\phi}-1}{c_\varsigma}\right), \qquad \varsigma = 1,2,3. \tag{5.30}$$

When the velocity is constant across a gridblock in each direction, this can be reduced to

$$\varsigma = \varsigma_0 + u_{\varsigma 0}\,\Delta\tau/\phi, \qquad \varsigma = 1,2,3. \tag{5.31}$$

All the equations of this section contribute to construct the streamlines and estimate the time of flight in each cell and along the complete streamline. Streamlines can be launched uniformly from the face of a cell containing injectors or producers with the number of streamlines proportional to the flux across the cell face. Once estimated $\Delta\tau$ everywhere, the streamline discretization will not require the explicit determination of streamtube geometry (Datta-Gupta and King, 2007).

5.3 Steps for streamline simulation

As it is identified in the mathematical formulation for the streamlines technique, the model for polymer flooding by streamline simulation manage two numerical tools: a multiphase-compositional numerical simulator in a 2D spatial coordinates and a multiphase-compositional simulator for 1D linear time of flight coordinate along streamlines.

In general, the major steps in streamline simulation are outlined below:

- Set a grid geometry, reservoir, and fluid properties, and with the 2D simulator determine pressure and saturation distribution in the grid.
- Calculate compositions in each gridblock explicitly , according to equation (5.9).
- With pressure, saturations and compositions known in each node, estimate the velocity at the faces of every cell in the 2D grid.
- Based on fluid velocities, construct the streamlines in 2D dimension from injection point to production point.
- Compute the time of flight along each streamline and identify isochrones (time of flight contours).
- Transfer the saturation and composition distribution in the 2D grid to the discretization of every streamline.

- With the 1D polymer flooding simulator, estimate saturation and composition profiles along the streamlines.
- For every time step, mapping the saturation and composition from the streamlines to the 2D grid.
- Periodically update, according to the flow case, the streamlines for a better representation of flow dynamics. Estimate the time of flight along the new streamlines and follow the remaining steps.

Figure 5.2 presents a flow chart that summarizes the procedure applied by the numerical algorithm in the simulation for polymer flooding by the streamline technique.

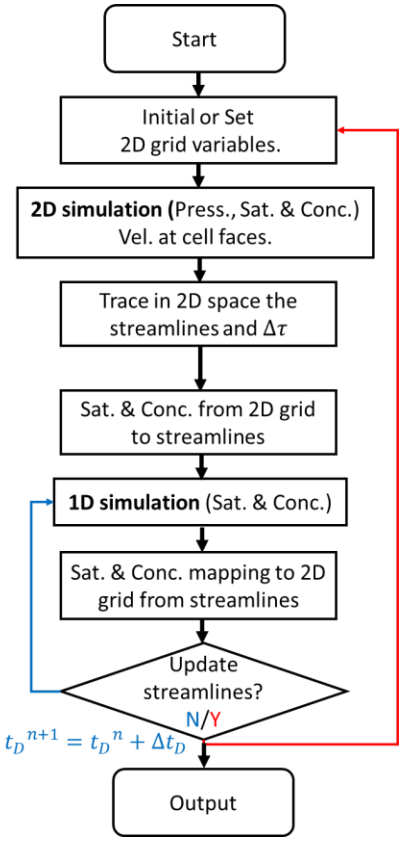

Figure 5.2: Flowchart of the numerical simulator for polymer flooding by streamlines

Chapter 6: Validation of the streamline-based model

6.1 Waterflooding in homogenous medium

The validation of the numerical model developed with the streamlines technique was done with experimental data for waterflooding, as well as CMG-STARS software. It considers a regular five-sport pattern in a homogeneous reservoir where injection and production rates are equal, the boundaries of the pattern are no-flow boundaries. The laboratory data correspond to waterfloods on a five-spot laboratory model with favorable and unfavorable mobility ratios (Douglas et al., 1959); where the sand was initially saturated with water, then oil was injected into one corner at a constant rate, and fluids production from the opposite corner was recorded. Several experiments were conducted at widely oil-water viscosity ratios ($0.083, 8.08, 141,$ and 754), oil produced was measured as a function of water injected. These experimental data have been used in previous publications (Higgins and Leighton, 1962, 1972) to compare the computed water flood performance for five-spot waterflood in laboratory models.

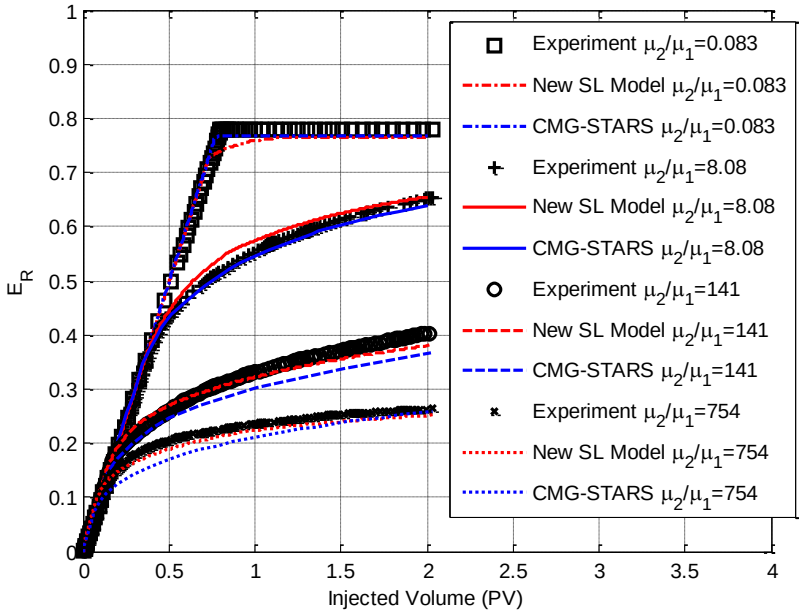

Figure 6.1: Comparison of experimental and simulated data for waterflooding. Simulated data were obtained with the proposed model and CMG-STARS software.

To reproduce the experiments, we used the specific sandpack properties, specified in the publication (properties such as rock, fluid, and geometry, as well as relative permeabilities). Relative permeabilities were fitted with Corey´s model and we noticed that this model was not the best fit for oil relative permeability (this could introduce some inaccuracies to reproduce the experimental behavior), while water relative permeability was a very good. Table 6.1 indicates some properties used for the 2D experimental five-spot physical model.

Experiment	#1	#2	#3	#4
Oil viscosity, cP	0.0137	0.0928	1.621	9.45
Oil-Water viscosity ratio	0.083	8.08	141.0	754.0
Porosity	0.375	0.375	0.375	0.375
Flow rate, cc/min	10	6	7	1.5
Permeability, D	11.1	11.1	11.1	11.1
Initial water saturation	0.125	0.087	0.087	0.087

Table 6.1: Brief description of five-spot model properties for laboratory waterflooding.

Figure 6.1 shows the experimental data reported by (Douglas et al., 1959) for different viscosity ratio experiments. It also shows results obtained with the CMG-STARS commercial simulator and the new model for Streamlines developed in this research (New SL Model), to reproduce the published data mentioned previously. Notice that the numerical simulations were conducted without any history matching procedure to improve the approximation, and as seen in this figure our model fits very well the experimental data for a wide range of viscosity ratio, favorable and unfavorable mobility ratios. Therefore, this presents a validation of the numerical algorithm used in the New SL Model to solve homogenous waterflooding problems.

Figure 6.2 shows the set of the streamlines computed with the New SL Model by using the algorithm of Pollock for a 2D numerical simulation of the $\mu_2/\mu_1 = 0.083$ case, where a homogeneous quarter five spot pattern was waterflooded. Simulation was conducted in a normalized 2D plane (x_D, y_D) with a mesh of 20 x 20 blocks, 20 streamlines, and 40 cells along the shortest streamline for time of flight discretization. It also exhibits the curves where particles represent the same time of flight or the isochrones (contours of equal time of flight) describing the propagation front. We only present the streamlines for this experiment because the others yield practically the same streamlines. For all experiments represented

in Figure 6.1, the set of streamlines was not update during the simulation, and nonetheless obtained a very good match between experimental and numerical results.

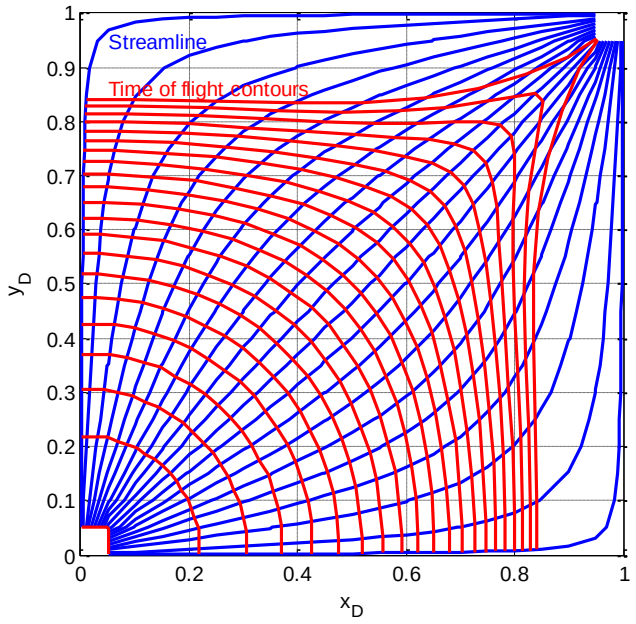

Figure 6.2: Streamlines and time of flight obtained from the New SL Model, with the data reported in the literature (Douglas et al., 1959).

As mentioned in the previous chapter, once the streamlines are computed, a 1D solution along each streamline is required, with the time of flight as a spatial coordinate. Figure 6.3 displays the saturation profiles at the breakthrough time of the extreme cases ($\mu_2/\mu_1 = 0.083$ and $\mu_2/\mu_1 = 754$) obtained with the New SL Model developed and related to the results in Figure 6.1. These are the 1D solutions to apply to each of the streamlines, and we can notice the big difference between these extreme scenarios, in which the displacement front for experiment 0.083 is very close to a piston like displacement and so more efficient than the other.

Figure 6.4 shows the contour plots of 2D saturation distribution at breakthrough time for the two experiments, obtained by adding up the 1D solutions for each set of streamlines. Notice that every contour line is a curve that connects points of the streamlines with the same saturation value. Figure 6.4 illustrates the development of the displacement front at breakthrough time in a 2D plane for the more efficient experiment, $\mu_2/\mu_1 = 0.083$, we observe a piston like displacement where all movable oil was swept. Notice, on the other

hand, that the less efficient experiment, $\mu_2/\mu_1 = 754$, a big amount of oil is left behind the displacement front at breakthrough time, resulting in a very inefficient process.

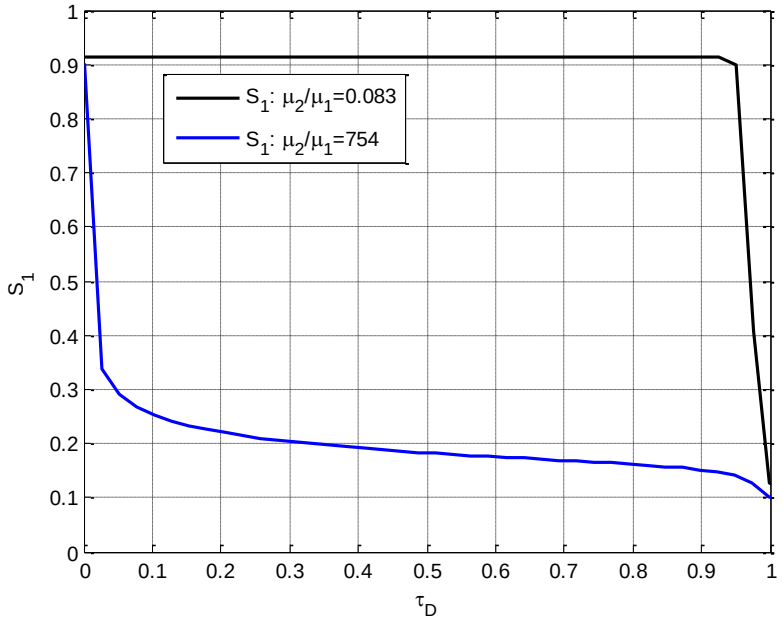

Figure 6.3: Profiles for saturation at breakthrough time, with normalized time of flight, obtained from experiments $\mu_2/\mu_1 = 0.083$ and $\mu_2/\mu_1 = 754$.

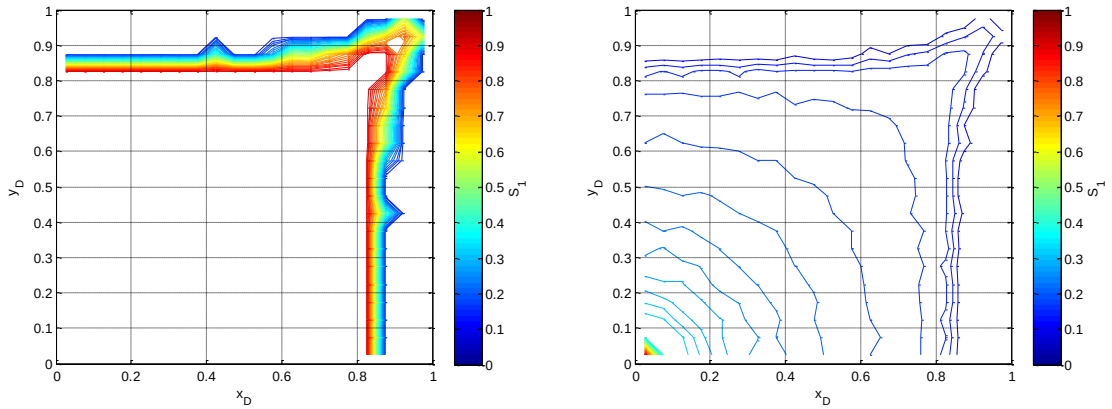

Figure 6.4: Profiles for saturation at breakthrough time, obtained from experiments a) $\mu_2/\mu_1 = 0.083$ (left) and b) $\mu_2/\mu_1 = 754$ (right).

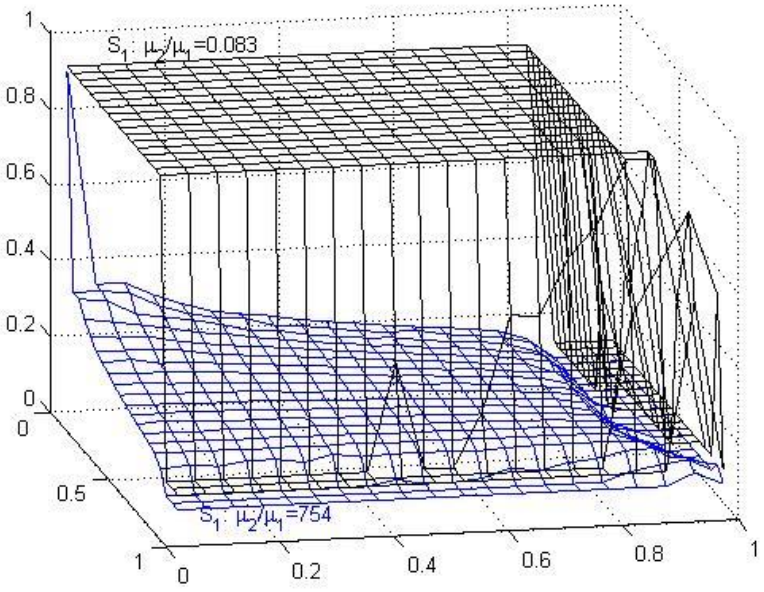

Figure 6.5: 3D view of saturation distribution at breakthrough time, obtained from the two experiments in Figure 6.4.

Figure 6.5 illustrates a 3D view representation of the saturation surfaces and a graphic comparison of the saturation distributions from Figure 6.4. This makes clear the amount of petroleum unswept if we carry out a process with $\mu_2/\mu_1 = 754$ instead of $\mu_2/\mu_1 = 0.083$.

6.2 Waterflooding in anisotropic medium

An important advantage of streamline simulation technique is the detailed capture of the effects of heterogeneity and anisotropy on flooding processes, such as fluid distributions, formation of pathways with remaining oil, and unswept zones. For the validation of the New SL Model regarding to the performance of the numerical algorithm in anisotropic formation for flooding processes, we used a published data (Landrum and Crawford, 1960) where authors considered an analytical procedure developed by Muskat (1949) to investigate the effects of directional permeability on sweep efficiency in a five-spot pattern under waterflooding. The Muskat's theoretical treatment considers the displacement of two fluids with same properties in an anisotropic reservoir under steady-state flow conditions, mobility ratio of one, and negligible gravity and capillary effects. Additionally, the validation procedure considers the solutions obtained with CMG-STARS and TRACE3D, an academic software

for streamlines simulation of a waterflooding process at field scale, developed by The Texas A&M University.

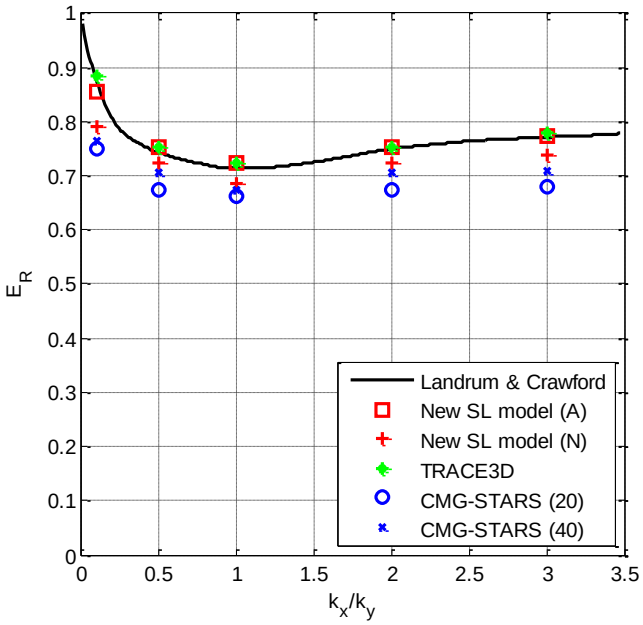

Figure 6.6: Comparison of analytical (Landrum and Crawford, 1960) and simulated data of waterflooding with directional permeability in a five-spot pattern.

Figure 6.6 presents results published by Landrum and Crawford (1960), in which the recovery efficiency versus horizontal permeability ratio (k_x/k_y) is plotted. To reproduce these results with the numerical simulators (New SL Model, CMG-STARS, and TRACE3D) we considered a flooding process with the injected fluid with having the same properties ($\mu_j = 1cP$, $k^*_{rj} = 1$, and $e_j = 1$) as the displaced one until breakthrough time, a mobility ratio of one, no initial water saturation, and no residual oil saturation. The streamlines simulators applied a mesh grid with 20 x 20 cells. The TRACE3D simulator considers the analytical solution from BL for the 1D solution along the streamlines, while the New SL simulator included two approximations to the 1D problem: an analytical and a numerical, New SL model (A) and (N), respectively. The CMG-STARS simulator was applied with two approximations for the mesh grid: with 20 x 20 and 40 x 40 cells.

The comparison of published and numerical results is shown in Figure 6.6, where it is noticed that results based on an analytical 1D solution [TRACE3D and New SL model (A)] for the streamlines match very good to the data published by Landrum and Crawford; solutions from

the New SL model (N) also show a good approximation. In the case of CMG-STARS results do not fit the published data, even though they improve as the mesh grid becomes more refined, when going from 20 x 20 to 40 x 40 cells.

Finally, to display how the streamlines change with a permeability direction contrast, we compare the streamlines for extreme cases illustrated in Figure 6.6, where $k_x/k_y = 1$ and $k_x/k_y = 0.1$. The streamlines construction for these two cases is the same as in Figure 6.7, in which it is clear the strong influence of permeability anisotropy on the configuration of streamlines and the time-of-flight estimations, this could indicate the formation of pathways, the unswept zones and the areal distribution of the remaining oil saturation.

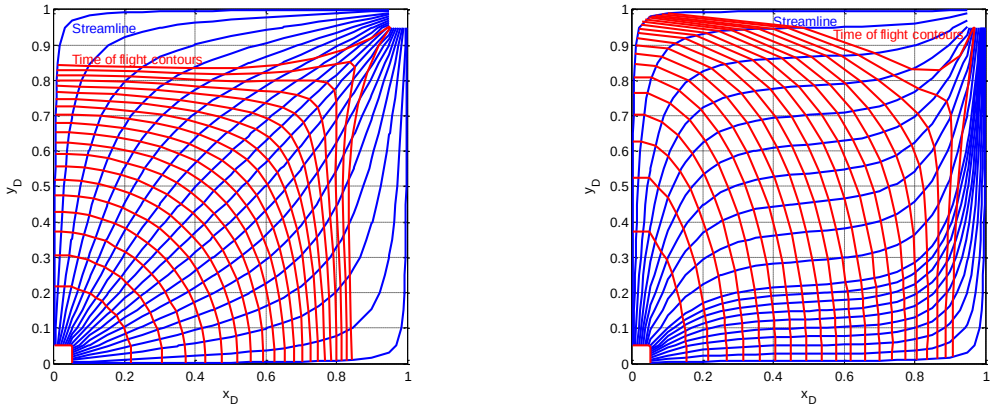

Figure 6.7: Streamlines and time of flight obtained from the New SL Model, with the data reported in the literature (Landrum and Crawford, 1960), for the cases a) $k_x/k_y = 1$ (left) and b) $k_x/k_y = 0.1$ (right).

From this section, we conclude that in spite of the simplifications considered in the New SL model, the streamline simulator satisfactorily reproduces results published in the literature, providing a practical tool to simulate a waterflooding process, in a heterogeneous media, with less information and time required.

6.3 Field case polymer flooding

So far, in this chapter, we have validated the algorithm of the New SL model with published data for waterflooding homogeneous cases (Douglas et al., 1959) and anisotropic permeability variation (Landrum and Crawford, 1960). For the validation of the New SL

model in a polymer flooding case, results are compared with those published by Qi et al. (2018) for the case of a quarter five-spot pattern polymer flooding simulation of a field case.

The field case simulation consists in a variable permeability formation with an average permeability of $5{,}000mD$, a porosity of 0.25%, and an initial oil saturation of 80%. The oil viscosity is $40cP$ and the brine viscosity at reservoir temperature is $0.5cP$. A polymer concentration of $0.4wt\%$ was considered to get an aqueous phase viscosity of $350cP$ (at a $10s^{-1}$ of shear rate). The rest of the geometrical, fluid, rock properties and polymer rheology data are described in the cited literature, and Table 6.2 indicates some properties used in the 2D quarter five-spot numerical model. For the injection strategy in the simulation case, $0.5PV$ of water was first injected at a constant rate of $1{,}000B/D$, then an additional $1.0PV$ of polymer solution was injected keeping the injection rate constant.

Phase viscosities	$\mu_1 = 0.5cP$	$\mu_2 = 40.0cP$
Water relative permeability	$k_{r1}^* = 0.2$	$e_1 = 2$
Oil relative permeability	$k_{r2}^* = 0.8$	$e_2 = 2$
Residual saturations	$S_{1r} = 0.3$	$S_{2r} = 0.2$
Polymer solution viscosity	$\mu_{1app} = 350cP$	$C_{41} = 0.4wt\%$
Reservoir properties	$\phi = 0.25$	$k = 5000mD$
Fluid injection rate	$Q = 1000B/D$	

Table 6.2: Polymer and reservoir data for 2D field scale polymer flooding simulation.

Because the results obtained from the publication are affected by a degree of permeability variation, the validation procedure includes the results obtained from the CMG-STARS using the same data of the New SL model, considering the average permeability previously indicted.

Figure 6.8 shows the behavior of recovery efficiency versus injected volumes for the five-spot water and polymer flooding simulation case presented by Qi et al. (2018) and, the behavior obtained with CMG-STARS and the New SL model. When comparing CMG with Qi's results, noticeable differences are observed in the waterflooding period, while in the polymer flooding period, the differences are considerable reduced, this is because polymer flooding tends to decrease the effects of permeability variations on recovery efficiency. The latter agrees with the findings of Qi et al. (2018); after conducting a sensitivity analysis for

different degrees of permeability variation, characterized by Dykstra-Parson coefficients of $0, 0.5$ and 0.8, they found no effect on oil recovery at 1.5PV injected; a recovery efficiency of 62.3% was obtained in all cases. The recovery from the CMG-STARS model at 1.5PV injected is 62.8%, so it presents a good match for the polymer flooding period.

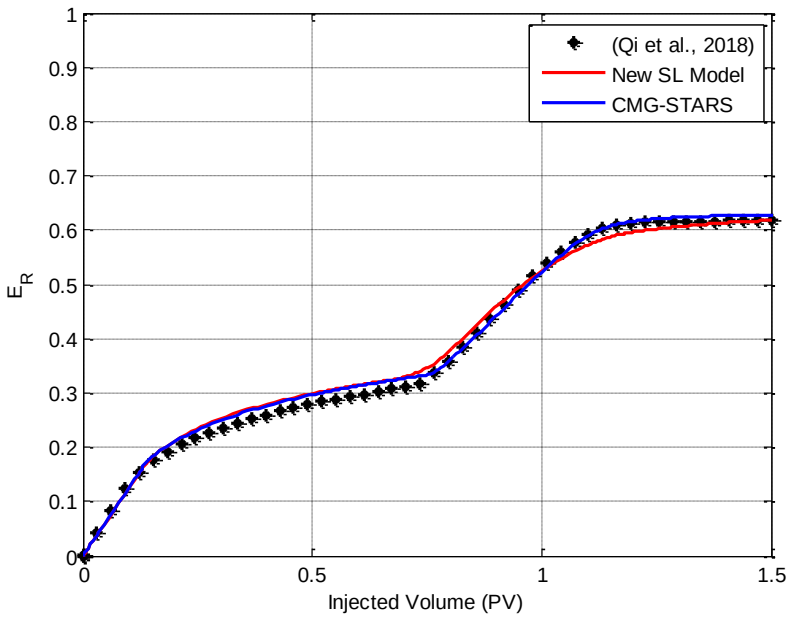

Figure 6.8: Comparison of published and simulated data for water and polymer flooding. Simulated data were obtained with the proposed model and CMG-STARS software.

From the Figure 6.8 it is also seen that the solution obtained with the streamline technique of the New SL model, fits very well the solution of the CMG-STARS in the waterflooding stage. In the polymer flooding stage, although the solution of the New SL model shows a good approximation to the solution of CMG-STARS, notice that the streamlines simulation yields an earlier and smoother response to polymer flooding than the commercial software, and that oil recovery is slightly lower after $1.0PV$ injected, but ends up in the same recovery efficiency reported by Qi et al., at 1.5 PV injected.

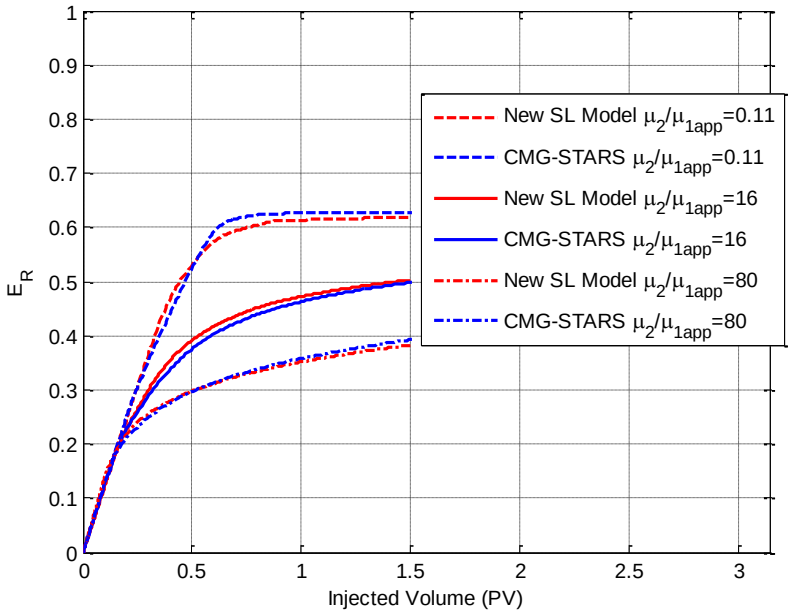

Figure 6.9: Comparison of simulated data for polymer flooding. Simulated data were obtained with the proposed model and CMG-STARS software.

In cases previously described, the polymer flooding started after $0.5PV$ of waterflooding, then to complement the validation procedure, this case was taken as the basis for another injection strategy in which the polymer is injected from the beginning of the flooding ($0.0PV$ injected), and we explore the performance of polymer flooding under three polymer concentration scenarios: 1) $C_{41} = 0.0wt\%$ with $\mu_2/\mu_{1app} \approx 80$, 2) $C_{41} = 0.1wt\%$ with $\mu_2/\mu_{1app} \approx 16$, and 3) $C_{41} = 0.4wt\%$ with $\mu_2/\mu_{1app} \approx 0.11$. Results obtained from the New SL model and CMG-STARS for these scenarios are presented in Figure 6.9, and results from the later are considered as reference for the validation. It can be observed in this figure that although results obtained with the streamlines model developed provide a good approximation to the CMG-STARS results, the numerical matching is better as the viscosity ratio increases.

Results shown in Figures 6.8 and Figure 6.9, for different injection strategies and a wide range of viscosity ratios, indicates that the streamlines model developed in this research works well under favorable and unfavorable mobility ratios, and provide a validation of the numerical algorithm for polymer flooding used in the New SL Model.

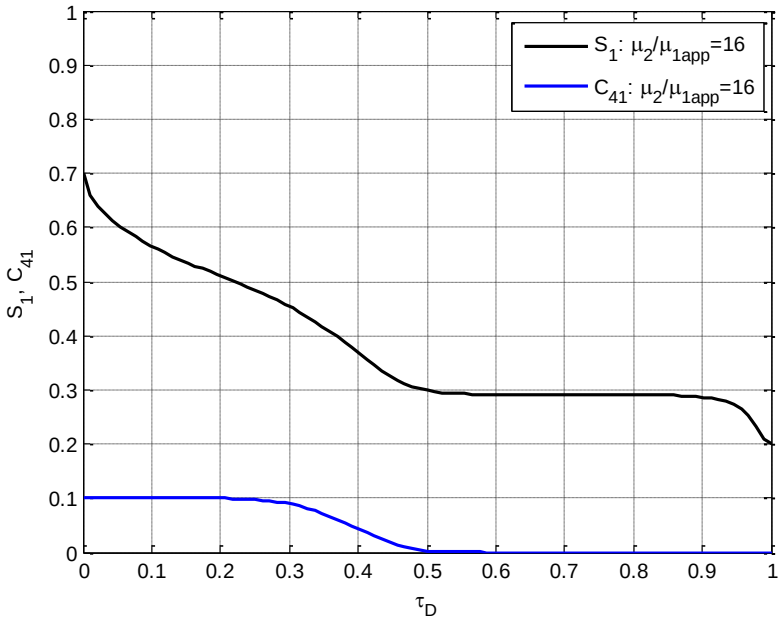

Figure 6.10: Profiles for saturation and polymer concentration at breakthrough time, with normalized time of flight, obtained from simulation case $\mu_2/\mu_{1app} = 16$.

Once the New SL Model has been validated, we show next, as an example, how the model represents the polymer transport in one of the previously simulated cases. Figure 6.10 illustrates the saturation and polymer concentration profiles at breakthrough time along the shortest streamline for the case of $\mu_2/\mu_{1app} = 16$; this figure shows that two displacement fronts (water front and polymer rich front) and a region with constant aqueous saturation between these two fronts develop during the flooding, making clear the beneficial effects of polymer concentration to achieve a better saturation profile.

An extension to a 2D representation of Figure 6.10 is presented in Figure 6.11 and Figure 6.12, where the contour plots of the aqueous phase saturation and polymer concentration are shown respectively; results were obtained with the New SL Model (left) and the CMG-STARS software (right). From the contours in Figure 6.11, it is evident that although both numerical tools are in agreement, the New SL Model represents better the saturation profile seen in Figure 6.10, near the two displacement fronts and in the section between the water front and the polymer rich front. A similar statement applies to the polymer composition front profiles of Figure 6.10 and Figure 6.12, so the New SL Model is a better alternative to represent the composition front. This is due to the truncation error associated with time and

space discretization in the conventional numerical formulation of CMG-STARS, that turns into numerical dispersion (Peaceman, 1977; Fanchi, 2006), so saturation or concentration fronts are expected to be more smeared in a conventional numerical formulation than in a streamline formulation that only applies a 1D space discretization. Additionally, although both numerical tools consider a grid with 20 x 20 cells, the streamline tool discretizes the time of flight coordinate into 80 cells in the shortest streamline, this contributes to reduce the numerical dispersion and so to get a better approximation to a sharp displacement front.

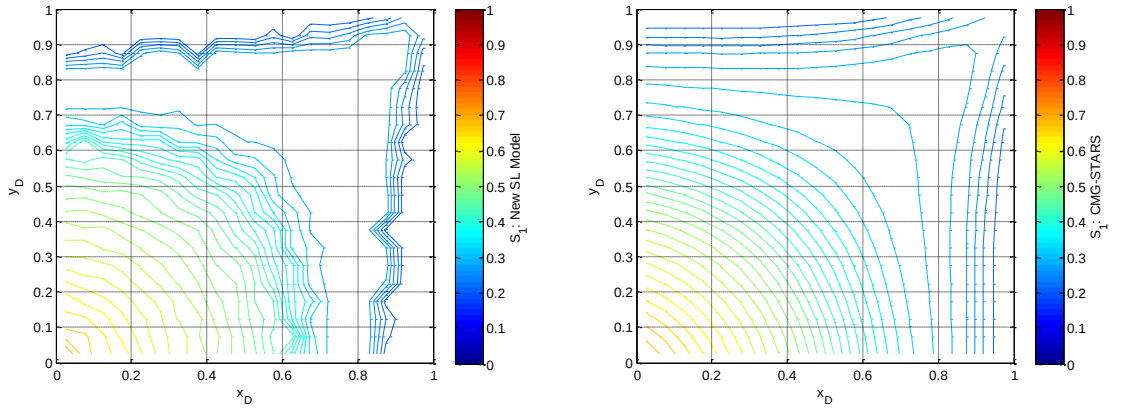

Figure 6.11: Saturation contours at breakthrough time, obtained from simulation case $\mu_2/\mu_{1app} = 16$ a) New SL Model (left) and b) CMG-STARS (right).

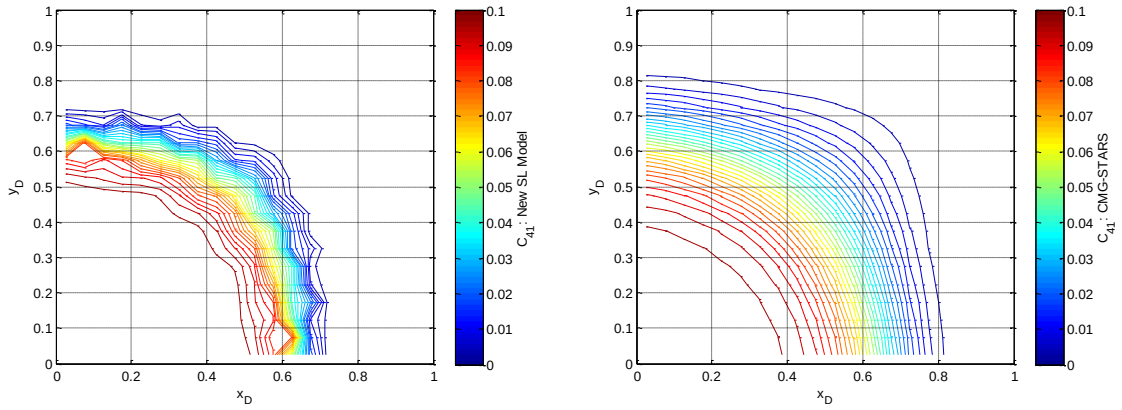

Figure 6.12: Polymer concentration contours at breakthrough time, obtained from simulation case $\mu_2/\mu_{1app} = 16$ a) New SL Model (left) and b) CMG-STARS (right).

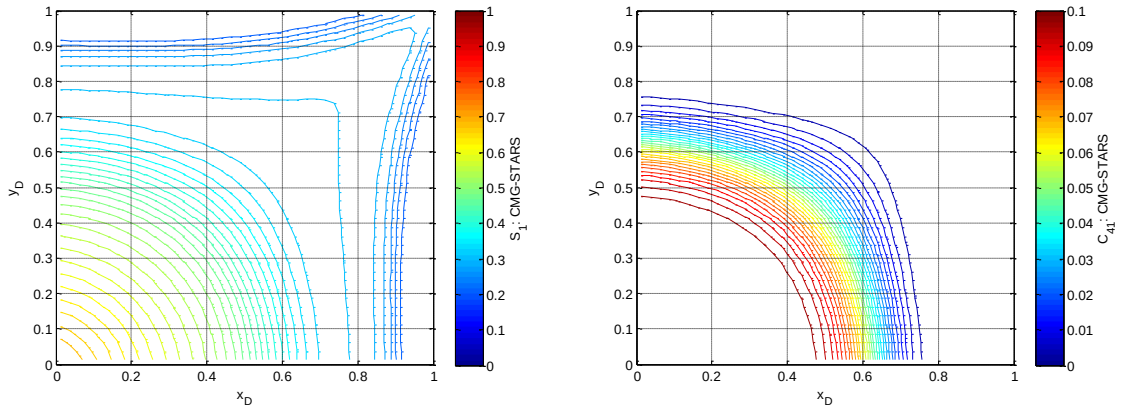

Figure 6.13: Contour plots at breakthrough time, obtained from simulation case $\mu_2/\mu_{1app} = 16$ with CMG-STARS and 40 x 40 cells: a) saturation (left) and b) polymer concentration (right).

According to the previously mentioned, a better representation of the displacement front in CMG-STARS, can be obtained with a more refined grid. This was verified by using grids of 40 x 40 and 80 x 80 cells to simulate the same problem. Figure 6.13 and Figure 6.14 present the contour lines of aqueous phase saturations (left) and polymer concentrations (right) for the 40 x 40 and 80 x 80 cells cases, respectively, where a reduction of the numerical dispersion is observed.

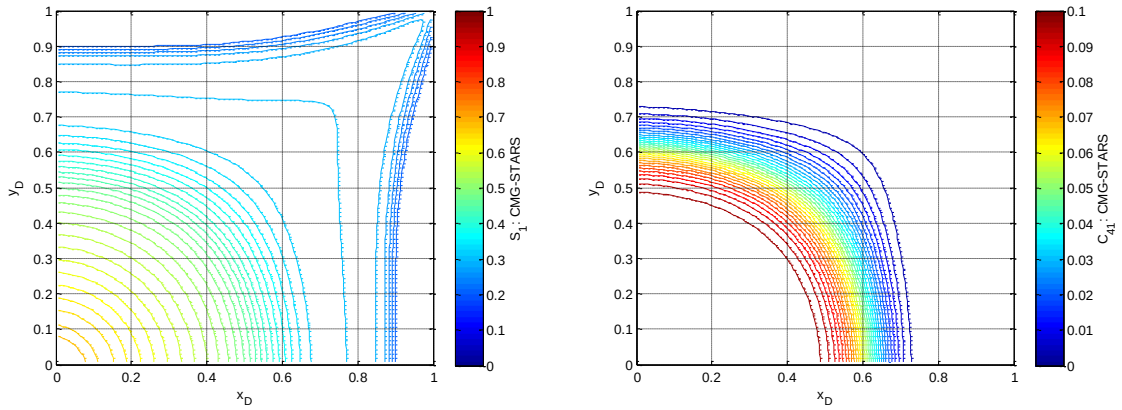

Figure 6.14: Contour plots at breakthrough time, obtained from simulation case $\mu_2/\mu_{1app} = 16$ with CMG-STARS and 80 x 80 cells: a) saturation (left) and b) polymer concentration (right).

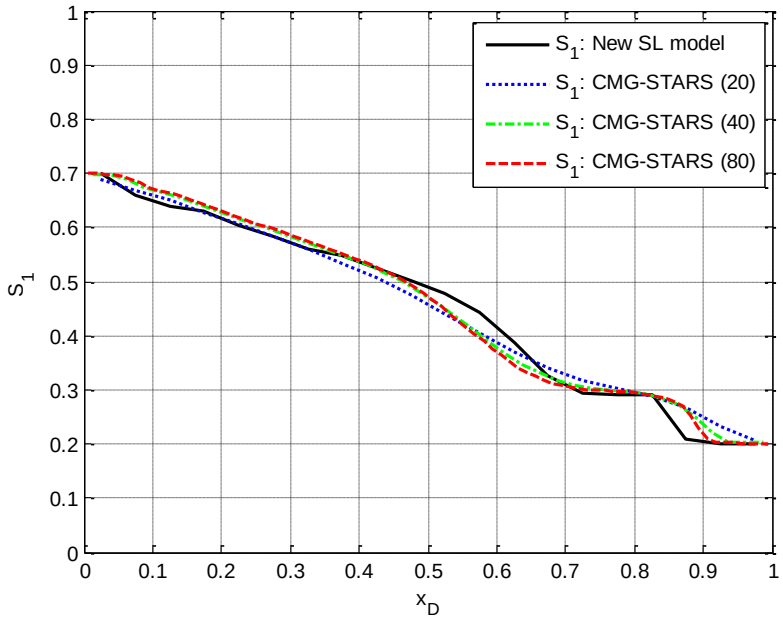

Figure 6.15: Profiles for saturation at breakthrough time, with normalized coordinate, obtained from simulation case $\mu_2/\mu_{1app} = 16$.

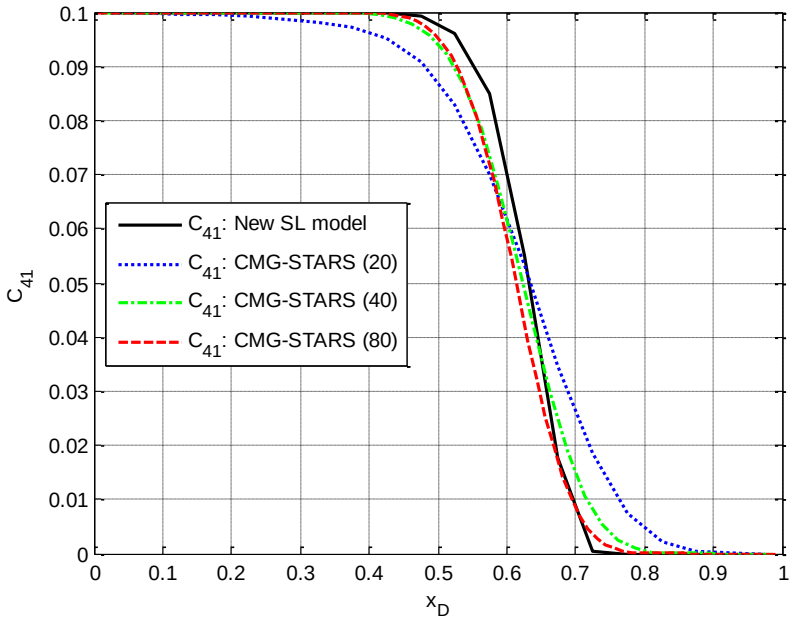

Figure 6.16: Profiles for polymer concertation at breakthrough time, with normalized coordinate, obtained from simulation case $\mu_2/\mu_{1app} = 16$.

For a better comparative of the numerical dispersion yielded by the New SL Model and the cases with CMG-STARS software, when solving the case of $\mu_2/\mu_{1app} = 16$, we consider the solution at $j = 1$ cells for any node i. Then, Figure 6.15 and Figure 6.16 present a comparison of the 1D solution along the x_D direction of the results in Figure 6.11 to Figure 6.14 for profiles saturation and polymer concentration respectively. These figures illustrate the comparison of the three scenarios obtained from CMG-STARS [a grid with 20 x 20 cells (20), 40 x 40 cells (40), and 80 x 80 cells (80)] with the scenario obtain from New SL Model (20 x 20 cells and 80 cells in the shortest SL). From the figures, we can identify that although the refinement reduces the numerical dispersion, the best solution [most refined grid (80)] with the conventional numerical formulation (CMG-STARS) exhibits deficiencies to represent mainly the water front and the polymer rich front (see Figure 6.15). A similar statement can be said for polymer composition profiles, nearby the concentration front (see Figure 6.16). Therefore, the New SL Model proposed is an alternative to mitigate the challenges documented by some authors (Lake et al., 1981; Thiele et al., 2010) that are related to numerical dispersion in simulators with Eulerian-based formulations (CMG-STARS), this tends to smear displacement fronts and misrepresent the true impact of chemicals on the flow dynamics.

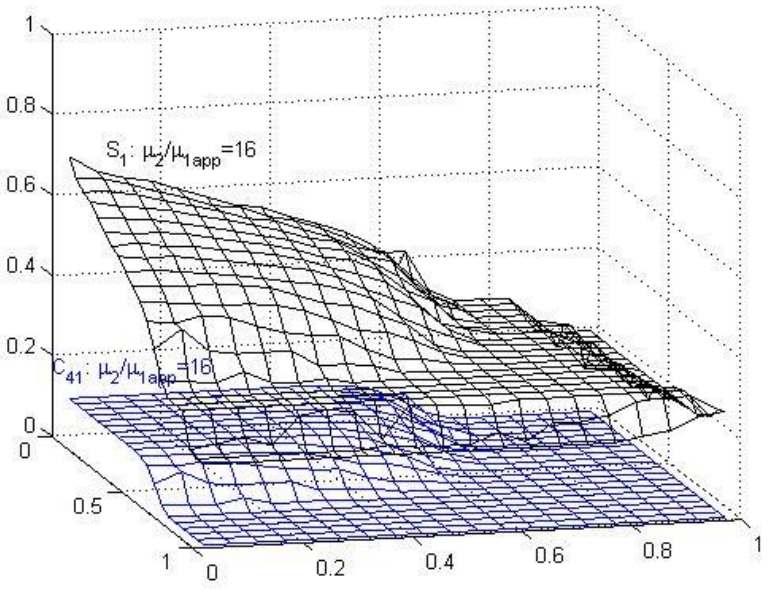

Figure 6.17: 3D saturation and concentration distributions at breakthrough time, obtained from simulation case in Figure 6.11.

Another important aspect to consider, is that the best solution [CMG-STARS (80)] with the finite difference conventional numerical formulation needed 180 timesteps compared with 65 with the New SL mode. Therefore, the streamline simulation required smaller number of solutions of the unknown variables than conventional finite difference simulator, as it has been indicated in other publications (Di Donato et al., 2003; Thiele et al., 2010; Vicente et al., 2012) related to polymer flooding modeling with streamlines.

Additionally, Figure 6.17 displays a 3D view of the aqueous phase saturation and polymer concentration surfaces of the simulated field scale case, as an alternative to get a better visualization of the amount and location of the petroleum left behind the two displacement fronts at breakthrough time. This representation and the contour plots previously described can give us a good idea of the areal saturation distribution, the unswept regions by waterflooding, as well as the swept sections by the polymer front, then an areal sweep efficiency and the remaining petroleum accumulations or sweet spots at breakthrough time can be estimated for the polymer flooding process.

Chapter 7: Conclusions

A practical streamline-based mathematical model for 2D, multiphase-compositional polymer flooding was presented. A numerical technique was applied to solve it and a validation procedure of the numerical algorithm was carried out. The following conclusions are drawn from the investigation:

1. Based on fractional flow theory, a practical 1D reservoir simulator for polymer flooding is developed. It considers non-Newtonian rheology (shear thinning and shear thickening), permeability reduction, reversible-irreversible adsorption and salinity variation effect. The validation of numerical algorithm was carried out; numerical solutions for waterflooding and polymer flooding, here developed, are in close agreement with analytical solutions, coreflood laboratory experiments and a CMG-STARS numerical model. Therefore, despite the assumptions or simplifications of the model, it provides a good representation to laboratory data, without losing reliability.
2. From the 1D numerical simulator and a flow dynamic analysis of the effects that key phenomena have on the main flow properties and oil recovery, the following elements are important to consider in polymer flooding project design:
    a. As polymer concentration decreases and injection flow rate increases (*effect of shear rate*), the E_R decreases to a minimum asymptotic value. When injection rate lessens the differences between the viscosity at zero shear rate and apparent viscosity profiles are reduced.
    b. A flow case with less *adsorption* level reaches faster to maximum recovery value than a flow case with more adsorption degree, even though, both eventually get to the maximum recovery efficiency at different times. Additionally, irreversible adsorption has larger detrimental effect than reversible one, so recovery efficiency is more affected.
    c. Increase in *salinity* tend to decrease benefits of polymer concentration on polymeric solution viscosity and increase retardation effects due to polymer adsorption. This combination anticipates water breakthrough and delays the polymer rich shock front.

d. Starting the polymer flooding with a slug of lower salinity than the chase continuous injection salinity improves the performance of the polymer rich front, so it increases the recovery efficiency.
e. From the flow cases presented with the same mobility ratio M^*, it was identified that increasing μ_{1app} has a better recovery efficiency benefit than increasing R_k.
f. The *amount of polymer* needed for the *slug injected* should be reduced as much as possible. Different combinations of polymer concentration and slug size can yield the same mass of polymer, but the better recovery was obtained with the highest polymer concentration and the smallest slug size.
g. In general, conditions where polymer concentration increases, injection rate decreases, polymer adsorption reduces and water salinity lessen, provide a more favorable scenario. It is also mandatory to consider economical aspects to optimize the quantity of polymer and salinity for a polymer flooding project.

3. Based on the streamlines technique, a 2D numerical reservoir simulator was constructed to represent the polymer flooding performance in homogeneous and heterogeneous porous media. The simulator couples two numerical tools: a multiphase numerical simulator in a 2D spatial coordinates and a multiphase-compositional simulator for 1D linear time of flight coordinate along each streamline.
4. This investigation successfully incorporated the practical 1D reservoir simulator for polymer flooding that was developed in chapter 4. It considers non-Newtonian rheology (shear thinning and shear thickening), permeability reduction, reversible-irreversible adsorption, and salinity effect. Therefore, these qualities are transferred to the streamline-based 2D model developed in this research.
5. The validation of the numerical algorithm of the 2D polymer flooding simulator was achieved in two steps: 1) numerical solutions here developed for waterflooding homogeneous and anisotropic media are in close agreement with experimental data, analytical solutions, and numerical solutions obtained from CMG-STARS model, 2) numerical solutions for polymer flooding under different injection strategies and a wide range of viscosity ratio (favorable and unfavorable mobility ratios) are in close agreement with a CMG-STARS model.
6. The 2D streamline-based model proposed is an alternative to mitigate numerical dispersion challenges obtained from simulators with Eulerian-based formulations that tends to smear displacement fronts and misrepresent the true impact of

chemicals on the flow dynamics. The streamline-based simulator allowed a numerical performance with less timesteps than finite difference-based simulator.

7. The 1D and 2D numerical simulators for polymer flooding developed in this research have been applied as practical tools which allowed to capture key aspects for representing physical-chemical phenomena and petroleum recovery behavior with less amount of detailed information, effort, and time, than commercial or academic field reservoir simulator for CEOR applications. Therefore, these predictive tools could work in screening studies to identify problems and avoiding unnecessary engineering work with low chances to get profitability, for an effective EOR project management.

References

Abdul-Hamid, S. A., and Muggeridge, A. H. (2018). Analytical Solution of Polymer Slug Injection with Viscous Fingering. *Computational Geosciences, Springer*, 22, pages711–723. https://doi.org/10.1007/s10596-018-9721-0.

AlSofi, A. M., and Blunt, M. J. (2010). Streamline-Based Simulation of Non-Newtonian Polymer Flooding. *SPE J.*, *15 (04)*, 895–905, SPE-123971-PA. https://doi.org/10.2118/123971-PA.

Alvarado, V., and Manrique, E. (2010). *Enhanced Oil Recovery - Field Planning and Development Strategies*. Gulf Professional Publishing, 1st ed.

Azad, M. S., and Trivedi, J. J. (2019). Quantification of the Viscoelastic Effects During Polymer Flooding: A Critical Review. *Society of Petroleum Engineers* SPE195687PA. https://doi.org/10.2118/195687-PA.

Batycky, R. P., Blunt, M. J., and Thiele, M. R. (1997). A 3D Field-Scale Streamline-Based Reservoir Simulator. *SPE Res. Eng., 12 (04), 246–254,* SPE-36726-PA. https://doi.org/10.2118/36726-PA.

Bear, J. (1972). *Dynamics of Fluids in Porous Media*. American Elsevier Publishing Company.

Bondor P. L., Hirasaki G. J., and Tham M. J. (1972). Mathematical Simulation of Polymer Flooding in Complex Reservoirs. *SPE J.,* 12 (05): 369–382, SPE-3524-PA. https://doi.org/10.2118/3524-PA.

Borazjani, S., Bedrikovetsky, P., and Farajzadeh, R. (2016). Analytical Solution of Oil Displacement by a Polymer Slug with Varying Salinity. *Journal of Petroleum Science and Engineering* 140, 28-40. https://doi.org/10.1016/j.petrol.2016.01.001.

Bratvedt, F., Gimse, T., and Tegnander, C. (1996). Streamline Computations for Porous Media Flow Including Gravity. *Transport in Porous Media, Springer* 25, 63–78. https://doi.org/10.1007/BF00141262.

Buckley, S. E., and Leverett M. C. (1942). Mechanism of Fluid Displacement in Sands. *Trans. 146 (01): 107–116*, SPE- 942107-G. https://doi.org/10.2118/942107-G.

Carcoana, A. (1992). *Applied Enhanced Oil Recovery*. Prentice Hall.

Chen, Z., Huan, G., and Ma, Y. (2006). *Computational Methods for Multiphase Flows in Porous Media*. Society for Industrial and Applied Mathematics.

Chen, H., Park, J., Datta-Gupta, A., Shekhar, S., Grover, K., Das, J., Shankar, V., Kumar, S., and Chitale, A. (2020). Improving Polymer Performance Via Streamline-Based Rate

Optimization: Mangala Field, India. *Society of Petroleum Engineers* SPE-200388-MS. https://doi.org/10.2118/200388-MS.

Chierici, G. L. (1994). *Principles of Petroleum Reservoir Engineering*. Vol. 2: Springer Verlag.

Choudhuri, B., Thakuria, C., Belize, A. A., Nurzaman, Z., and Al Hashmi, A. (2015). Optimization of a Large Polymer Flood with Full-Field Streamline Simulation. *SPE Res Eval & Eng 18 (03): 318–328*, SPE-169746-PA. https://doi.org/10.2118/169746-PA.

Clemens, T., Abdev, J., and Thiele, M. R. (2010). Improved Polymer-Flood Management Using Streamlines. *SPE Res Eval & Eng* 14 (02): 171–181, SPE-132774-PA. https://doi.org/10.2118/132774-PA.

CPGE. (2000). *Technical Documentation for UTCHEM-9.0 A Three Dimensional Chemical Flood Simulator*. Volume II. The University of Texas at Austin.

Craig, F. F. (1971). *The Reservoir Engineering Aspects of Waterflooding*. Vol. 3, SPE Monograph Series.

Craig, F. F., Jr.; Geffen, T. M.; Morse, R. A. Oil Recovery Performance of Pattern Gas or Water Injection Operations from Model Tests. *Trans*. 204 (01): 7–15. SPE-413-G. https://doi.org/10.2118/413-G.

Crane, M. J., and Blunt, M. J. (1999). Streamline-Based Simulation of Solute Transport. *Water Resources Research*, 35 (10), 3061-3078.

Dake, L. P. (1978). *Fundamentals of Reservoir Engineering*. Development in Petroleum Science 8, ELSEVIER.

Datta-Gupta, A., and King, M. J. (2007). *Streamline Simulation: Theory and Practice*. Vol. 11, SPE Textbook Series.

Datta-Gupta, A., and King, M. J. (1995). A Semianalytic Approach to Trace Flow Modeling in Heterogeneous Permeable Media. *Advances in Water Resources*, 18, 9-24. https://doi.org/10.1016/0309-1708(94)00021-V.

De Paula, A. S., and Pires, A. P. (2015). Analytical Solution for Oil Displacement by Polymer Slugs Containing Salt in Porous Media. *Journal of Petroleum Science and Engineering* 135, 323-335. https://doi.org/10.1016/j.petrol.2015.09.001.

Delamaide, E., Zaitoun, A., Renard, G., and Tabary, R. (2014). Pelican Lake Field - First Successful Application of Polymer Flooding in a Heavy Oil Reservoir. SPE Res Eval & Eng 17 (03): 340–354 SPE-165234-PA. https://doi.org/10.2118/165234-PA.

Delaplace, P., Delamaide, E., Euzen, T., Roggero, F., and Kopecny, P. (2013). Reservoir Simulation of a Polymer Flood Pilot in the Pelican Lake Heavy Oil Field (Canada) - a Step Forward. *Society of Petroleum Engineers* SPE-166028-MS. https://doi.org/10.2118/166028-MS.

Delshad, M., Kim, D. H., Magbagbeola, O. A., Huh, C., Pope GA, and Tarahhom, F. (2008). Mechanistic Interpretation and Utilization of Viscoelastic Behavior of Polymer Solution for Improved Polymer-Flooding Efficiency. *Society of Petroleum Engineers* SPE-113620-MS. https://doi.org/10.2118/113620-MS.

Delshad, M., Pope, G. A., and Sepehrnoori, K. (1996). A Compositional Simulator for Modeling Surfactant Enhanced Aquifer Remediation, 1 Formulation. *Journal of Contaminant Hydrology* 23 303-327. https://doi.org/10.1016/0169-7722(95)00106-9.

Di Donato, G., Huang, W., and Blunt, M. Streamline-Based Dual Porosity Simulation of Fractured Reservoirs. *Society of Petroleum Engineers* SPE-84036-MS. https://doi.org/10.2118/84036-MS.

Dickson, J. L., Leahy-Dios, A., and Wylie, P. L. (2010). Development of Improved Hydrocarbon Recovery Screening Methodologies. Society of Petroleum Engineers SPE-129768-MS. https://doi.org/10.2118/129768-MS.

Donaldson, E. C., Chilingarian, G. V., and Yen, T. F. (1985). *Enhanced Oil Recovery - I Fundamentals and Analyses*. ELSEVIER-Amsterdam-Oxford-New York-Tokyo.

Donaldson, E. C., Chilingarian, G. V., and Yen, T. F. (1989). *Enhanced Oil Recovery - II Processes and Operations*. ELSEVIER-Amsterdam-Oxford-New York-Tokyo.

Douglas, J., Peaceman, D. W., Rachford, H. H. (1959). A Method for Calculating Multi-Dimensional Immiscible Displacement. *Trans. AIME* 216, 297 – 308. SPE-1327-G. https://doi.org/10.2118/1327-G.

Druetta, P., and Picchioni, F. (2018). Surfactant-Polymer Flooding: Influence of the Injection Scheme. *Energy & Fuels* 32, 12, 12231–12246. https://doi.org/10.1021/acs.energyfuels.8b02900.

Ertekin, T., Abou-Kassem, J. H., and King, G. R. (2001). Basic Applied Reservoir Simulation. *Society of Petroleum Engineers* Textbook Series.

Fanchi, J. R. (2006). *Principles of Applied Reservoir Simulation*. ELSEVIER - Gulf Professional Publishing, 3rd.

Green, D. W., and Willhite, G. P. (1998). *Enhanced Oil Recovery*. Vol. 6, SPE Textbook Series.

Hashmet, M. R., AlSumaiti, A. M., Qaiser, Y., and AlAmeri, W. S. (2017). Laboratory Investigation and Simulation Modeling of Polymer Flooding in High-Temperature, High-Salinity Carbonate Reservoirs. *Energy & Fuels* 31, 12, 13454–13465. https://doi.org/10.1021/acs.energyfuels.7b02704.

He, J. S., Song, Z. Y., Qiu, L., Xie, F., Tan, Z. L., Nan, H., Yue, Q. S., and Li, X. N. (1998). High Temperature Polymer Flooding in Thick Reservoir in ShuangHe Oilfield. *Society of Petroleum Engineers*, SPE-50933-MS. https://doi.org/10.2118/50933-MS.

Helfferich, F. G. (1981). Theory of Multicomponent Multiphase Displacement in Porous Media. *SPE J.* 21 (01): 51–62 SPE-8372-PA. https://doi.org/10.2118/8372-PA.

Herrera, I., and Pinder, G. F. (2012). Mathematical Modeling in Science and Engineering: An Axiomatic Approach. *Wiley*, 1st ed.

Higgins, R. V., and Leighton, A. J. (1962). A Computer Method to Calculate Two-Phase in Any Irregularly Bounded Porous Medium. Journal of Petroleum Technology. *J Pet Technol* 14 (06) 679–683. SPE-243-PA. https://doi.org/10.2118/243-PA.

Higgins, R. V., and Leighton, A. J. (1972). *Numerical Methods for Determining Streamlines and Isopressures for Use in Fluid Flow Studies*. Bureau of Mines, San Francisco, CA (USA). San Francisco Energy Research Lab, BM-RI-7621.

Hirasaki, G. J. (1981). Application of the Theory of Multicomponent, Multiphase Displacement to Three-Component, Two-Phase Surfactant Flooding. SPE J. 21 (02): 191–204 SPE-8373-PA. https://doi.org/10.2118/8373-PA.

Hirasaki, J., and Pope, G. P. (1974). Analysis of Factors Influencing Mobility and Adsorption in the Flow of Polymer Solution Through Porous Media. *SPE J*. 14 (04), 337–346 SPE-4026-PA. https://doi.org/10.2118/4026-PA.

Hite, J. R., Avasthi, S. M., and Bondor, P. L. (2004). Planning Successful EOR Projects. *J Pet Technol* 57 (03): 28–29 SPE-0305-0028-JPT. https://doi.org/10.2118/0305-0028-JPT.

Honarpour, M., Koederitz, L., and Harvey, A. H. (1986). *Relative Permeability of Petroleum Reservoirs*. CRC Press, Inc. Boca Raton, Florida.

Jessen, K., and Orr, F. M. (2002). Compositional Streamline Simulation. Society of Petroleum Engineers, SPE-77379-MS. https://doi.org/10.2118/77379-MS.

Jones Jr, R. S., Pope, G. A. and Lake LW. (1984). A Predictive Model for Water and Polymer Flooding. *Society of Petroleum Engineers* SPE-12653-MS. https://doi.org/10.2118/12653-MS.

Jun, Y., and Minglu, W. (2011). Streamline Numerical Well Test Interpretation – Theory and Method. ELSEVIER - Gulf Professional Publishing.

Kakati, A., Kumar, G., and Sangwai, J. S. (2020). Low Salinity Polymer Flooding - Effect on Polymer Rheology, Injectivity, Retention and Oil Recovery Efficiency. *Energy & Fuels* 34, 5, 5715–5732. https://doi.org/10.1021/acs.energyfuels.0c00393.

Kamal, M. S., Adewunmi, A. A., Sultan, A. S., Al-Hamad, M. F., and Mehmood, U. (2017). Recent Advances in Nanoparticles Enhanced Oil Recovery - Rheology, Interfacial Tension, Oil Recovery, and Wettability Alteration. *Journal of Nanonaterials*, *Hindawi Vol. 2017*. https://doi.org/10.1155/2017/2473175.

Kazempour, M., and Alvarado, V. (2011). Geochemically Based Modeling of pH-Sensitive Polymer Injection in Berea Sandstone. *Energy & Fuels*, 25, 9, 4024–4035. https://doi.org/10.1021/ef200773h.

Kazempour, M., Manrique, E. J., Alvarado, V., Zhang, J., and Lantz, M. (2012). Role of Active Clays on Alkaline-Surfactant-Polymer Formulation Performance in Sandstone Formations. *Fuel* 104 593-606. https://doi.org/10.1016/j.fuel.2012.04.034.

Koh, H., Lee, V. B., and Pope, G. A. (2018). Experimental Investigation of the Effect of Polymers on Residual Oil Saturation. *Society of Petroleum Engineers* SPE-179683-MS. https://doi.org/10.2118/179683-MS.

Lake, L. W. (1989). *Enhanced Oil Recovery*. Prentice-Hall, 1st ed.

Landrum, B. L., and Crawford, P. B. (1960). Effect of Directional Permeability on Sweep Efficiency and Production Capacity. J Pet Technol 12 (11): 67–71, SPE-1596-G. https://doi.org/10.2118/1597-G.

LeBlanc, J. L., and Caudle, B. H. (1971). A Streamline Model for Secondary Recovery. *SPE J.* 11 (01): 7–12, SPE-2865-PA. https://doi.org/10.2118/2865-PA.

Li, A., Chen, H., Datta-Gupta, A., Chitale, A., Shekher, S., Shankar, V., Kumar, M. S., Ahmed, A., Das, J., and Kumar, R. (2022). Streamline Based Polymerflood Injection Optimization: Experiences in the Malaga Field, India. *Society of Petroleum Engineers* SPE-209998-MS. https://doi.org/10.2118/209998-MS.

Manzoor, A. A. (2020). Modeling and Simulation of Polymer Flooding with Time-Varying Injection Pressure. *ACS Omega* 5, 10, 5258–5269. https://doi.org/10.1021/acsomega.9b04319.

Martin, F. D., Hatch, M. J., Shepitka, J. S., and Ward, J. S. (1983). Improved Water-Soluble Polymers for Enhanced Recovery of Oil. *Society of Petroleum Engineers* SPE-11786-MS. https://doi.org/10.2118/11786-MS.

Masuda, Y., Tang, K., Mlyazawa, M., and Tanaka, S. (1992). 1D Simulation of Polymer Flooding Including the Viscoelastic Effect of Polymer Solution. *SPE Res Eng* 7 (02): 247–252, SPE-19499-PA. https://doi.org/10.2118/19499-PA.

Morel-Seytoux, H. (1965). Analytical-Numerical Method in Waterflooding Predictions. *SPE J.* 5 (03): 247–258, SPE-985-PA. https://doi.org/10.2118/985-PA.

Morel-Seytoux, H. (1966). Unit Mobility Ratio Displacement Calculations for Pattern Floods in Homogeneous Medium. *SPE J.* 6 (03): 217–227, SPE-1359-PA. https://doi.org/10.2118/1359-PA.

Morrison, F. A. (2001). *Understanding Rheology*. Oxford University Press.

Muskat, M. (1937). *Flow of Homogeneous Fluids*. International Human Resources Development Corporation, Boston, Massachusetts.

Muskat, M. (1949). *Physical Principles of Oil Production*. McGraw-Hill, 1st ed.

Muskat, M., and Wyckoff, R. D. (1934). A Theoretical Analysis of Water-Flooding Networks. *Trans*. 107 (01): 62–76, SPE-934062-G. https://doi.org/10.2118/934062-G.

Olajire, A. A. (2014). Review of ASP EOR (alkaline surfactant polymer enhanced oil recovery) Technology in the Petroleum Industry - Prospects and Challenges. *Energy*, Vol. 77, pp. 963–982; 2014. https://doi.org/10.1016/j.energy.2014.09.005.

Patton, J. T., Coats, K. H., and Colegrove, G. T. (1971). Prediction of Polymer Flood Performance. *SPE J.* 11 (01): 72–84, SPE-2546-PA. https://doi.org/10.2118/2546-PA.

Peaceman, D. W. (1977). *Fundamentals of Numerical Reservoir Simulation*. Development in Petroleum Science 6, ELSEVIER.

Peddibhotla, S., Cubillos, H., Datta-Gupta, A., and Wu, C., H. (1996). Rapid Simulation of Multiphase Flow Through Fine-Scale Geostatistical Realizations Using a New 3-D, Streamline Model: A Field Example. Society of Petroleum Engineers, SPE-36008-MS. https://doi.org/10.2118/36008-MS.

Pollock, D. W. (1988). Semianalytical Computation of Path Lines for Finite-Difference Models. *Groundwater*, 26, No. 6. https://doi.org/10.1111/j.1745-6584.1988.tb00425.x.

Pope, G. A., Hong, C.H., Sepehrnoori, K., and Lake, L. W. (1981). Two Dimensional Simulation Of Chemical Flooding. *Society of Petroleum Engineers* SPE-9939-MS. https://doi.org/10.2118/9939-MS.

Pope, G. A., and Nelson, R. C. (1978). A Chemical Flooding Compositional Simulator. *SPE J.* 18 (05): 339–354, SPE-6725-PA. https://doi.org/10.2118/6725-PA.

Pope, G. A. (1980). The Application of Fractional Flow Theory to Enhanced Oil Recovery. SPE J. 18 (05): 339–354, SPE-7660-PA. https://doi.org/10.2118/6725-PA.

Pyrcz, M. J., and Deutsch, C. (2014). *Geostatistical Reservoir Modeling*. Oxford University Press.

Qi, P., Lashgari, H., Luo, H., Delshad, M., Pope, G., and Balhoff, M. (2018). Simulation of Viscoelastic Polymer Flooding – From the Lab to the Field. *Society of Petroleum Engineers* SPE-191489-MS. https://doi.org/10.2118/191498-MS.

Rai, K. R., Johns, R. T., Delshad, M., Lake, L. W., and Goudarzi, A. (2013). Oil-Recovery Predictions for Surfactant Polymer Flooding. Journal of Petroleum Science and Engineering 112 341-350. https://doi.org/10.1016/j.petrol.2013.11.028.

Rosado-Vázquez, F. J., Rangel-German, E. R., and Rodríguez-De la Garza, F. (2007). Analysis of Capillary, Gravity and Viscous Forces Effects in Oil/Water Displacement. *Society of Petroleum Engineers* SPE-108722-MS. https://doi.org/10.2118/108722-MS.

Rosado-Vázquez, F. J., Rangel-German, E. R., and Rodríguez-De la Garza, F. (2006). Analytical Model for Vertical Oil-Water Displacement Under Combined Viscous, Capillary

and Gravity Effects. *Society of Petroleum Engineers* SPE-100659-MS. https://doi.org/10.2118/100659-MS.

Rosado-Vázquez, F. J., Bashbush-Bauza, J. L., and López-Ramìrez, S. (2022). Practical Mathematical Model for the Evaluation of Main Parameters in Polymer Flooding: Rheology, Adsorption, Permeability Reduction, and Effective Salinity. *ACS Omega* 7, 29, 24982–25002. https://doi.org/10.1021/acsomega.2c00277.

Scheidegger, A. E. (1974). *The Physics of Flow Through Porous Media*. University of Toronto Press, 3rd ed.

Seright, R. S. (2016). How Much Polymer Should Be Injected During a Polymer Flood? Review of Previous and Current Practices: *SPE J.* 22 (01): 1–18, SPE-179543-PA. https://doi.org/10.2118/179543-PA.

Seto, C. J., Jessen, K., and Orr, F. M. (2007). Using Analytical Solutions in Compositional Streamline Simulation of a Field-Scale CO_2-Injection Project in a Condensate Reservoir, *SPE Res Eval & Eng* 10 (04): 393–405 SPE-79690-PA. https://doi.org/10.2118/79690-PA.

Shiran, B. S., and Skauge, A. (2013). Enhanced Oil Recovery (EOR) by Combined Low Salinity Water/Polymer Flooding. *Energy & Fuels*, 27, 3, 1223–1235. https://doi.org/10.1021/ef301538e.

Shapiro, A. A., Bedrikovetsky, P. G., and Pires, A. P. (2004). A New Method for Analytical Modelling of Chemical Flooding. *Society of Petroleum Engineers* SPE-88461-MS. https://doi.org/10.2118/88461-MS.

Sharafi, M. S., and Jamialahmadi, M. (2016). Mathematical Model for Prediction of Oil Recovery of Core-Flood Test in Process of Viscoelastic Polymer Flooding. *Petroleum Science and Technology* Vol. 34, 11-12, 1098-1105. https://doi.org/10.1080/10916466.2016.1172090.

Sheng, J. J. (2014). A Comprehensive review of Alkaline-Surfactant-Polymer (ASP) flooding. *Asia-Pacific Journal of Chemical Engineering* Vol. 9 471-489. https://doi.org/10.1002/apj.1824.

Sheng, J. J. (2011). *Modern Chemical Enhanced Oil Recovery - Theory and Practice*. Elsevier, Burlington.

Shepard, D. (1968). A two-dimensional interpolation function for irregularly spaced data. ACM National Conference. https://doi.org/10.1145/800186.810616.

Sorbie, K. S. (1991). *Polymer-Improved Oil Recovery*. CRC Press, Inc.

Standnes, D. C., and Skjevrak, I. (2014). Literature Review of Implemented Polymer Field Projects. *Journal of Petroleum Science and Engineering* Vol. 122, 761-775. https://doi.org/10.1016/j.petrol.2014.08.024.

Taber, J. J., Martin, F. D., and Seright, R. S. (1997). EOR Screening Criteria Revisited—Part 1: Introduction to Screening Criteria and Enhanced Recovery Field Projects. *SPE Res Eng* 12 (03): 189–198*,* SPE-35385-PA. https://doi.org/10.2118/35385-PA.

Thiele, M. R., Batycky, R. P., Pöllitzer, S., and Clemens, T. (2010). Polymer-Flood Modeling Using Streamlines. *SPE Res Eval & Eng* 13 (02): 313–322, SPE-115545-PA. https://doi.org/10.2118/115545-PA.

Thomas, S. (2008). Enhanced Oil Recovery – An Overview. *Oil & Gas Science and Technology – Rev. IFP*, Vol. 63, 9-19. https://doi.org/10.2516/ogst:2007060.

Vermolen, E. C. M., Pingo-Almada, M., Wassing, B. M., Ligthelm, D. J., and Masalmeh, S. K. (2014). Low-Salinity Polymer Flooding - Improving Polymer Flooding Technical Feasibility and Economics by Using Low Salinity Make-Up Brine. *International Petroleum Technology Conference*, IPTC-17342-MS. https://doi.org/10.2523/IPTC-17342-MS.

Vicente, B. J., Priimenko, V. I., and Pires, A. P. (2014). Semi-analytical solution for hyperbolic system modeling 1D polymer slug flow in porous media. *Journal of Petroleum Science and Engineering* 115 102-109. https://doi.org/10.1016/j.petrol.2014.02.005.

Vicente, B. J., Priimenko, V. I., and Pires, A. P. (2012). Streamlines Simulation of Polymer Slugs Injection in Petroleum Reservoirs, Society of Petroleum Engineers, SPE-153616-MS. https://doi.org/10.2118/153616-MS.

Wang, J., and Liu, H. (2014). A Novel Model and Sensitivity Analysis for Viscoelastic Polymer Flooding in Offshore Oilfield. *Journal of Industrial and Engineering Chemistry* 20, 656-667. https://doi.org/10.1016/j.jiec.2013.05.030.

Wang, B., Lake, L. W., and Pope, G. P. (1981). Development and Application of a Streamline Micelar/Polymer Simulator. *Society of Petroleum Engineers* SPE-10290-MS. https://doi.org/10.2118/10290-MS.

Wassmuth, F. R., Arnold, W., Green, K., and Cameron, N. (2009). Polymer Flood Application to Improve Heavy Oil Recovery at East Bodo. *J Can Pet Technol* 48 (02), 55–61, PETSOC-09-02-55. https://doi.org/10.2118/09-02-55.

Welge, H. J. (1952). A Simplified Method for Computing Oil Recovery by Gas or Water Drive. *J Pet Technol* 4 (04), 91–98. SPE-124-G. https://doi.org/10.2118/124-G.

Willhite, G. P. (1986). *Waterfloodong*. Vol. 3, SPE Textbook Series.

Zhang, G., and Seright, R. S. (2014). Effect of Concentration on HPAM Retention in Porous Media. *SPE J.* 19 (03): 373–380, SPE166265PA. https://doi.org/10.2118/166265-PA.

Zheng, C. G., Gall, B. L., Gao, H. W., Miller, A. E., and Bryant, R. S. (1998). Effects of Polymer Adsorption and Flow Behavior on Two-Phase Flow in Porous Media. *Society of Petroleum Engineers* SPE-39632-MS. https://doi.org/10.2118/39632-MS.

Zhu, Z., Garritsen, M. G., and Thiele, M. R. (2009). Thermal Streamline Simulation for Hot Water Flooding. *Society of Petroleum Engineers* SPE-119200-MS. https://doi.org/10.2118/119200-MS.